ABSTRACT

DANCES AND ESCAPE OF THE VORTEX QUARTET

by
Brandon M. Behring

This dissertation considers the linear stability of a one-parameter family of periodic solutions of the four-vortex problem known as 'leapfrogging' orbits. These solutions, which consist of two pairs of identical yet oppositely-signed vortices, were known to W. Gröbli (1877) and A. E. H. Love (1883) and can be parameterized by a dimensionless parameter α related to the geometry of the initial configuration. Simulations by Acheson and numerical Floquet analysis by Tophøj and Aref both indicate, to many digits, that the bifurcation occurs when $1/\alpha = \phi^2$, where ϕ is the golden ratio.

Acheson observed that, after an initial period of aperiodic leapfrogging, the perturbed solutions could transition into one of two behaviors: a bounded orbit he called '*walkabout*' and an unbounded orbit he called '*disintegration.*' In the walkabout orbit, two like-signed vortices couple together, and the motion resembles a three-vortex system. In disintegration, four vortices separate into two pairs—each pair consisting one negative and one positive vortex—that escape to infinity along two transverse rays.

Two goals are addressed in this dissertation:

1. **Goal I** To rigorously demonstrate, without numerics, the exact algebraic value for which the Hamiltonian pitchfork bifurcation occurs.

2. **Goal II** Understand how, as the parameter, α is decreased, the dynamics transitions between the various regimes and escape become first possible and then almost inevitable, as well as identifying the structures in phase-space that are responsible for the transition between these regimes.

DANCES AND ESCAPE OF THE VORTEX QUARTET

by
Brandon M. Behring

A Dissertation
Submitted to the Faculty of
New Jersey Institute of Technology and
Rutgers, The State University of New Jersey – Newark
in Partial Fulfillment of the Requirements for the Degree of
Doctor of Philosophy in Mathematical Sciences

Department of Mathematical Sciences
Department of Mathematics and Computer Science, Rutgers-Newark

December 2020

APPROVAL PAGE

DANCES AND ESCAPE OF THE VORTEX QUARTET

Brandon M. Behring

Dr. Roy H. Goodman , Dissertation Advisor Date
Associate Professor, Department of Mathematical Sciences, New Jersey Institute of Technology

---

Dr. Dennis Blackmore, Committee Member Date
Professor, Department of Mathematical Sciences, New Jersey Institute of Technology

---

Dr. Michael Siegel, Committee Member Date
Professor, Department of Mathematical Sciences, New Jersey Institute of Technology

---

Dr. Panayotis G. Kevrekidis, Committee Member Date
Professor, Department of Mathematics and Statistics, University of Massachusetts Amherst.

Dr. Richard O. Moore, Committee Member Date
Director of Programs and Services, SIAM (Society for Industrial and Applied Mathematics

BIOGRAPHICAL SKETCH

Author: Brandon M. Behring

Degree: Doctor of Philosophy

Date: December 2020

Undergraduate and Graduate Education:

- Doctor of Philosophy in Mathematical Sciences,
  New Jersey Institute of Technology, Newark, New Jersey, 2020
- Master of Science in Mathematics,
  New York University, New York, New York, 2011

Major: Mathematical Sciences

Presentations and Publications:

B. M. Behring and R. H. Goodman, "Stability of leapfrogging vortex pairs: A semi-analytic approach," *Phys. Rev.Fluids*, 4:124703, Dec 2019.

T. Budylin, S. R. Guariglia, L. I. Duran, B. M. Behring, Z. Shaikh, L. S. Neuwirth, and P. Banerjee, "Ultrasonic vocalization sex differences in 5-ht1a-r deficient mouse pups: Predictive phenotypes associated with later-life anxiety-like behaviors," *Behav. Brain Res.*, vol. 196, 373:112062, 2019

B. M. Behring, "Dynamics Near the Leapfrogging Vortex Quartet," *Poster*, SIAM Conference on Dynamical Systems Snowbird, Utah, U.S., 2019.

To my wife, mother and sister.

ACKNOWLEDGMENT

I want to thank my advisor Roy Goodman for his guidance and mentorship. I would also like to thank my committee- Dennis Blackmore, Michael Siegel, Panayotis Kevrekidis, and Richard Moore for their support and aide. Thanks to Kevin Mitchell, who inspired me to look at the escape using dimer coordinates, which become a significant part of this dissertation. I am also grateful for the funding given to me by the Department of Mathematical Sciences. Additionally, I have appreciated Professors Bose, Matveev, Lushi, Luke, and Shirokoff, along with my colleague Ryan Allaire for his friendship. I want to thank my wife, Tatyana, for her love and support as I made my way through graduate school. I would also like to thank my mother, Valerie, and my sister, Renee, for raising me and encouraging me to press forward.

TABLE OF CONTENTS

Chapter **Page**

TABLE OF CONTENTS
(Continued)

Chapter **Page**

TABLE OF CONTENTS
(Continued)

Chapter **Page**

TABLE OF CONTENTS
(Continued)

Chapter **Page**

LIST OF TABLES

Table **Page**

LIST OF FIGURES

Figure **Page**

LIST OF FIGURES
(Continued)

Figure **Page**

LIST OF FIGURES
(Continued)

Figure **Page**

LIST OF FIGURES
(Continued)

Figure **Page**

LIST OF FIGURES
(Continued)

Figure **Page**

CHAPTER 1

INTRODUCTION

1.1 Introduction to Point-vortex Motion

Point-vortex motion arises in the study of concentrated vorticity in an ideal, incompressible fluid described by Euler's equations. The two-dimensional Euler equations of fluid mechanics, a partial differential equation (PDE) system, support a solution in which the vorticity is concentrated at a single point. Helmholtz derived a system of ordinary differential equations (ODEs) that describe the motion of a set of interacting vortices that behave as discrete particles, which approximates the fluid motion in the case that the vorticity is concentrated in very small regions [59]. This system of equations has continued to provide exciting questions for over 150 years.

Kirchhoff formulated these equations as a Hamiltonian system [7, 32]. This Hamiltonian formulation has allowed researchers to apply to this system an extensive repertoire of methods developed in the study of the gravitational N-body problem. In this paper, we consider a configuration of vortices with vanishing total circulation, which has no analog in the N-body problem. As such, many techniques developed for the gravitational problem do not apply to the net-zero circulation case of the N-vortex problem. This case of the N-vortex problem is relatively less studied, despite its physical importance and mathematical richness, Ref. [6, 8, 21].

Bose-Einstein condensates (BEC), a quantum state of matter that exists at ultra-low temperatures, have provided an experimental testbed in which point vortices can be studied in the laboratory. These were first observed experimentally in Ref. [5] in 1995, in work that led to the 2001 Nobel Prize in Physics for Cornell and Wieman, along with Ketterle. The same group experimentally demonstrated concentrated vortices in BECs [39]. This new experimental model has led in the last 20 years

to a new flowering of interest in point vortices. In this experimental system, the BEC is confined using a strong magnetic field that introduces additional terms into the equations of motion. Ref. [43], for example, shows nicely how experiment and mathematical theory have been used together to explore these nonlinear phenomena.

1.2 Introduction to the Leapfrogging Trajectory

The leapfrogging orbits are a remarkable one-parameter family of relative periodic orbits known as 'leapfrogging orbits,' described first by Gröbli in 1877 [27] and independently by Love (1883) [34]. It can be considered as a simple two-dimensional model of the phenomenon of two smoke rings passing through each other periodically, first discussed by Helmholtz in 1858 [14, 59]. The four vortices are analogous to the four intersections that the two vortex rings made with a plane containing the axis of propagation. Recall that a relative periodic orbit is defined as an orbit that is periodic modulo a group orbit of a symmetry of the system, in this case, translation.

Another physical model that is simple to reproduce is the half-ring vortex phenomenon popularized in a series of internet videos produced by "The Physics Girl" Dianna Cowern [19] for PBS Digital Studies, see Figure 1.1. By dragging a dinner plate along the surface of a swimming pool twice, she creates a pair of vortex half-rings in the water, which she visualizes by pouring dye into the vortices where the rings meet the pool's surface. These videos provide a beautiful and tangible visualization of the motions of vortex pairs, where the leapfrogging motion can be observed.

The leapfrogging solution to the point-vortex system of equations is built from simple components. As shown in Section 3.3, two vortices of equal and opposite-signed vorticity move in parallel at a uniform speed with their common velocity inversely proportional to the distance between them. Two vortices of equal and like-signed

Figure 1.1 Clockwise from top left: (i) Dianna Cowern [19] drags a plate forward into the pool and gently lifts it out at an angle. (ii) The vortex half-ring moves slowly across the pool and is visible as two dimples on the surface of the water rotating in opposite directions. (iii) Schematic showing the structure of the vortex half-ring. (iv) Dianna Cowern puts food dye into the vortex half-ring to make the vortex tube connecting the two surface dimples visible.

vorticity, by contrast, trace a circular path with a constant rotation rate proportional to the inverse square of the distance between them, see Figure 1.2.

Remark 1.2.1. *To reduce clutter, we have attempted to create a consistent graphical language, with the trajectories of positive vortices colored red and those of negative vortices colored blue. This language carries over in a consistent way to the reduced systems introduced later. We thus eliminate legends in most subsequent figures.*

In this dissertation, we consider the two pairs of identical point vortices, which we call the *vortex quartet*. In particular, we consider an initial configuration of the vortex quartet where the vortices arranged collinearly and symmetrically at $t = 0$, with vortices of strength positive one at $\mathbf{r}_1^+$ and $\mathbf{r}_2^+$ and vortices of strength negative one at $\mathbf{r}_1^-$ and $\mathbf{r}_2^-$; see Figure 1.3. Let the 'breadths' of the pairs denote the distances $d_1 = \left\|\mathbf{r}_1^+ - \mathbf{r}_1^-\right\|$ and $d_2 = \left\|\mathbf{r}_2^+ - \mathbf{r}_2^-\right\| > d_1$ at $t = 0$. This symmetric collinear

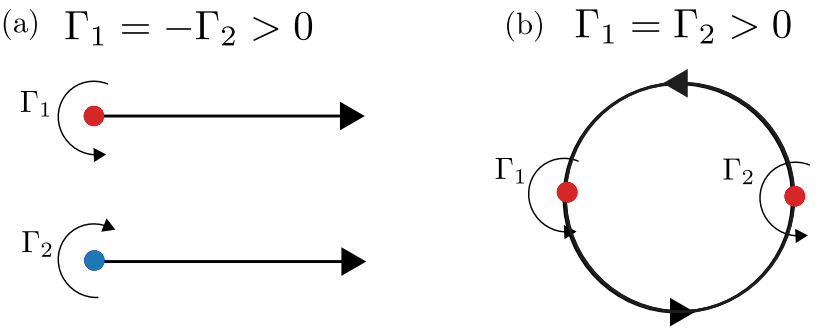

Figure 1.2 (a) Opposite-signed vortices move in parallel along straight lines. (b) Like-signed vortices move along a circular path.

state depends, after a scaling, on only one dimensionless parameter, the ratio of the breadths of the pairs, $\alpha = d_1/d_2$.

With reference to Figure 1.3, the two vortices $\mathbf{r}_2^+$ and $\mathbf{r}_2^-$ starting closer to the center of symmetry initially have larger rightward velocity than the outer pair, $\mathbf{r}_1^+$ and $\mathbf{r}_1^-$. As the 'inner pair' propagates, the distance between them increases, causing them to slow down. Simultaneously, the distance between the 'outer pair' decreases, causing them to speed up. After half a period, the inner and outer pairs' identities are interchanged, and the process repeats. This relative periodic motion exists only for a finite range of breadth-ratios $\alpha_0 < \alpha < 1$ where $\alpha_0 = 3 - 2\sqrt{2} \approx 0.171573$.

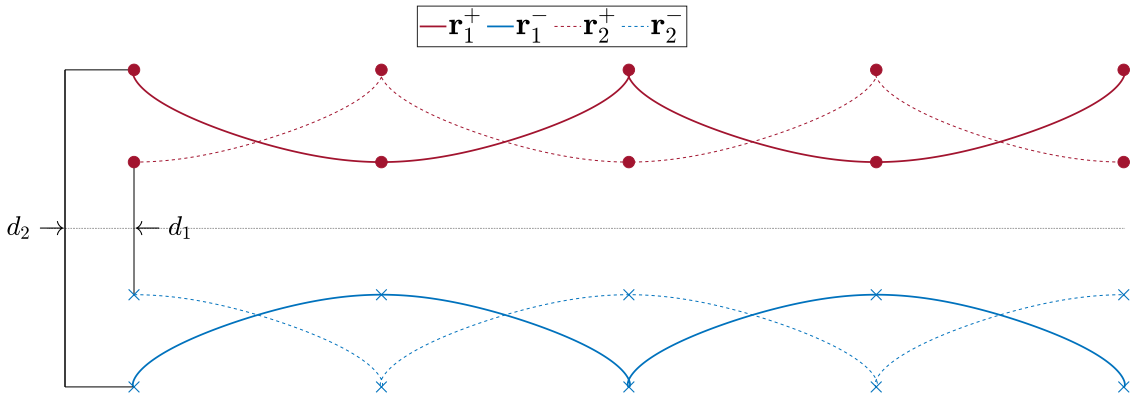

Figure 1.3 The curves show trajectories from a numerically-generated leapfrogging solution, with initial particle positions and separations labeled. Motion is from left to right with particle positions marked every half-period.

1.3 Stability of the Leapfrogging Orbit

As $\alpha \to 1^-$, it is useful to think of the system as composed of two pairs of like-signed vortices. In this limit, the separation within each pair is small relative to the distance between the two vortex pairs. In this regime, each like-signed pair 'coalesces' into a vortex of double the vorticity, when viewed from a distance, and the motion resembles that of two oppositely-spinning vortices translating along parallel lines. As α is decreased, the interaction between the two pairs is more pronounced.

The parameter α determines the stability of the motion. Direct numerical simulations by Acheson suggest that the leapfrogging solution is stable only for $\alpha > \alpha_2 = \phi^{-2} = \frac{3-\sqrt{5}}{2} \approx 0.38$, where ϕ is the golden ratio [2]. When the leapfrogging orbit is merely weakly unstable, i.e., for α just below α_c, nearby orbits remain close to the leapfrogging orbit for all time; however, the motion is now chaotic, and we observe *aperiodic* leapfrogging.

Acheson observed that, after an initial period of aperiodic leapfrogging, the perturbed solutions could transition into one of two behaviors: a bounded orbit he called '*walkabout*' and an unbounded orbit he called '*disintegration*.' In the walkabout orbit, two like-signed vortices couple together, and the motion resembles a three-vortex system. In disintegration, four vortices separate into two pairs—each pair consisting one negative and one positive vortex—that escape to infinity along two transverse rays, see Figure 1.4.

Tophøj and Aref, having noticed similar behavior in the chaotic scattering of identical point vortices [54], studied the stability problem further [55]. They examined linearized perturbations about the periodic orbit, thereby reducing the stability question to a Floquet problem. They confirm Acheson's value of α_2 via the numerical solution of this Floquet problem. However, their attempt at a more mathematical derivation of the fortuitous value of α_2 depends on an *ad hoc* argument based on 'freezing' the time-dependent coefficients at their value at $t = 0$, a method

that has been known sometimes to produce incorrect results [38, 40]. They note from numerical simulations that there does not exist a value of α that precisely separates walkabout from disintegration behavior. Instead, both can occur at the same value of α, depending on the form of the perturbation.

More recently, Whitchurch et al. [61] examined the system through the extensive use of numerically calculated Poincaré surfaces of section. They observe that the bifurcation at $\alpha = \alpha_2$ is of Hamiltonian pitchfork type. They also identify the third type of breakup behavior in addition to walkabout and disintegration, which they call *braiding*, see Figure 1.4(b). The existence of such a motion is implicit in the earlier three-vortex work of Rott [51] and the chaotic scattering work of Tophøj and Aref [54].

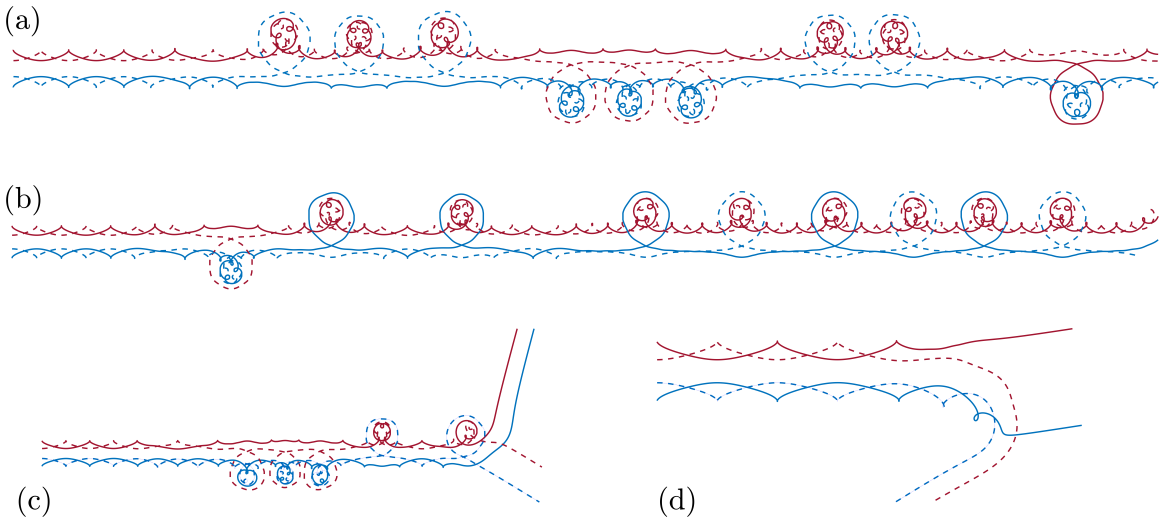

Figure 1.4 Motion in physical space. (a) A trajectory featuring several bouts of walkabout motion including one extended period of three consecutive walkabout 'dances'. (b) A trajectory featuring first walkabout orbits and later braiding orbits, as the two negative (blue) vortices take turns orbiting the tightly bound pair of positive (red) vortices.
(c) A leapfrogging motion that transitions to walkabout motion before disintegrating.
(d) A leapfrogging motion that disintegrates without a walkabout stage.

1.4 Goals

We have two goals in this dissertation:

1. **Goal I** To demonstrate, without numerics, the exact algebraic value for which the Hamiltonian pitchfork bifurcation occurs.

2. **Goal II** Understand how, as the parameter, α is decreased, the dynamics transitions between the various regimes and escape becomes first possible and then almost inevitable, as well as identifying the structures in phase-space that are responsible for the transition between these regimes.

In Chapter 2, we introduce the mathematical concepts and techniques we use throughout this dissertation. In Sections 2.1, 2.2, and 2.3 we review dynamical systems, Hamiltonian dynamics, and the stability of periodic orbits. In Chapter 3, in Sections 3.1, 3.2, and 3.3, we introduce the point-vortex model, its Hamiltonian framework and present a solution to the two-vortex. In Section 4, we present a novel reduction of the three-vortex problem zero and for the vortex quartet.

After reviewing the foundational concepts of Hamiltonian dynamical systems and the N-vortex problem, we address **Goal I** in Chapter 5. We first reduce and transform the linear stability problem to solving an *explicit* linear Hamiltonian system of differential equations with periodic coefficients. We then address Goal I and provide three distinct approaches:

1. Transforming the time-periodic linear system into one with constant coefficients by successive Lie transforms and averaging.

2. Using the method of harmonic balance to search for a value of our parameter in which there exists a periodic solution, indicating that the Floquet multipliers collide on the real axis.

3. Using the conjectured bifurcation value as an ansatz and explicitly finding a periodic solution for that value.

In order to address **Goal II**, in Section 4.3, we present a new reduction of the four-vortex problem into '*dimer*' coordinates which are used to understand the nonlinear

transitions. In Chapter 6, we provide a comprehensive phenomenology of the vortex quartet, and in Chapter 7 we utilize this knowledge to understand the transitions of the perturbed leapfrogging orbit as we vary the energy level.

CHAPTER 2

SUMMARY OF MATHEMATICAL TOOLS AND TECHNIQUES

In this chapter, we summarize the mathematical techniques and definitions used throughout this dissertation. This material can be read as needed. We begin in Section 2.1 and Section 2.2 by reviewing the basic concepts and definitions of dynamical systems in general and Hamiltonian systems in particular. This section also serves as an opportunity to introduce terminology, notation, and conventions. In Section 2.3, we review the concepts used in this dissertation regarding the stability of periodic orbits: the Poincaré map, linearized perturbation equations, Floquet theory, and the Hill's determinant. These concepts are used in Chapter 5.

In Section 2.4, we review perturbation techniques based on the concept of Lie transforms that are used in Chapter 5 and in Appendix C. In Section 2.5, we discuss the nature of chaos in Hamiltonian systems and provide a brief discussion of the relevant ideas of KAM theory needed to interpret the results of Chapters 6 and 7. We conclude this chapter in Section 2.6 by introducing a relatively new technique in dynamical systems to visualize invariant phase space structures known as Lagrangian descriptors that are used throughout this dissertation.

2.1 Basic Definitions of a Dynamical System

In this section, we introduce fundamental notions of the geometric theory of (autonomous) dynamical systems. For a complete treatment, see Meiss [40] and for a treatment aimed towards Hamiltonian systems, see Meyer and Offin [41].

2.1.1 Dynamical Systems

Consider the initial value problem

$$\frac{d\mathbf{x}}{dt} = f(\mathbf{x}) \quad \text{and} \quad \mathbf{x}(t_0) = \mathbf{x}_0 \in \mathbb{R}^n, \tag{2.1}$$

where the vector field $f : \mathcal{O} \to \mathbb{R}^n$ is a globally Lipschitz function and $\mathcal{O}$ is an open set in $\mathbb{R}^n$. For the remainder of this chapter, f is assumed to be smooth. The fundamental existence and uniqueness theorem for differential equations [40, 41, 63], states that there exists a global unique solution $\mathbf{x}(t)$ for t. The parameterized solution is a *trajectory* while the oriented but unparameterized curve is an *orbit*. If $\mathbf{x}(0) = \mathbf{y} \in \mathbb{R}^n$, then the solution $\mathbf{x}(t) = \varphi_t(\mathbf{y})$ is a *complete flow*. That is $\varphi_t(\mathbf{x})$ is a one-parameter, differentiable mapping such that:

1. φ_0 is the identity map $\varphi_0(\mathbf{x}) = \mathbf{x}$ and

2. φ_t satisfies the *group property*: for all $t, s \in \mathbb{R}$,

$$\varphi_t \circ \varphi_s = \varphi_{t+s}.$$

2.1.2 Invariant Structures

For future reference, we state a few key definitions used throughout this text. Assuming the system (2.1):

1. The *forward orbit* of a point $\mathbf{z}$ is $\Gamma^+_{\mathbf{x}} = \{\varphi_t(\mathbf{x}) : t \geq 0\}$ while the *pre-orbit* is given by $\Gamma^-_{\mathbf{x}} = \{\varphi_t(\mathbf{x}) : t \leq 0.\}$ The *full orbit* $\mathbf{x}$ is given by taking the union of the forward orbit and the pre-orbit, $\Gamma_{\mathbf{x}} = \Gamma^-_{\mathbf{x}} \cup \Gamma^+_{\mathbf{x}}$.

2. A set Λ is *forward (backward) invariant* if $\varphi_t(\Lambda) \subset \Lambda$ for all $t > 0$ ($t < 0$). A set is invariant if it is both forward and backward invariant.

3. A point $\mathbf{x}^*$ is an *equilibrium* if its image under the flow consists of only that point, i.e., $\Gamma_{\mathbf{x}^*} = \{\mathbf{x}^*\}$. For the system described by (2.1), a point is an equilibrium if $f(\mathbf{x}^*) = \mathbf{0}$.

4. A non-constant solution to (2.1), $\boldsymbol{\gamma}$, is a *periodic orbit* if there exists $T \neq 0$ such that $\varphi_{s+T}(\mathbf{x}) = \varphi_s(\mathbf{x})$ for all $s \in \mathbb{R}$ and $\mathbf{x} \in \gamma$. If T is smallest positive number with this property, it is known as the *period* of $\boldsymbol{\gamma}$.

5. The stable set of an invariant set Λ is the set of points asymptotic to Λ in forward time
$$W^s(\Lambda) = \{\mathbf{x} \notin \Lambda : \varphi_t(x) \to \Lambda \text{ as } t \to \infty\}$$
and unstable set of an invariant set Λ is the set of points asymptotic to Λ in backward time
$$W^u(\Lambda) = \{\mathbf{x} \notin \Lambda : \varphi_t(x) \to \Lambda \text{ as } t \to -\infty\}.$$

6. A *heteroclinic* orbit, Γ, is an orbit such that each $\mathbf{x} \in \Gamma$ is backward asymptotic to an invariant set B and forward asymptotic to an invariant set F, i.e., $\Gamma \subset W^u(B) \cap W^s(F)$.

7. A *homoclinic* orbit, Γ, is an orbit such that each $\mathbf{x} \in \Gamma$ is backward asymptotic and forward asymptotic to same invariant set A, i.e., $\Gamma \subset W^u(A) \cap W^s(A)$.

2.1.3 Invariant Subspaces and Manifolds

We can analyze the stability of an equilibrium point $\mathbf{x}^*$ by linearizing around that point. This analysis requires computing the eigenvalues of the Jacobian at that point, $A = Df(\mathbf{x}^*)$. The standard theory of stability for linear systems applies, allowing E, the generalized eigenspace of A, to be decomposed into invariant subspaces $E = E^u \bigoplus E^c \bigoplus E^s$, where the invariant subspaces of the equilibrium point $\mathbf{x}^*$ are as follows.

1. The unstable subspace, E^u, which consists of the span of generalized eigenvectors with eigenvalues with a positive real part.

2. The center subspace, E^c, which consists of the span of generalized eigenvectors with eigenvalues with real part equal to zero.

3. The stable subspace, E^s, which consists of the span of generalized eigenvectors with eigenvalues with a negative real part.

Invariant Manifold Theorems A k-dimensional manifold is a subset of $\mathbb{R}^n$ that is locally diffeomorphic to $\mathbb{R}^k$ where $k \leq n$. That is, it can be locally represented as a graph of a function. Assuming in (2.1) that f is smooth, i.e., $f \in C^\infty(\mathbb{R}^n)$, the invariant manifolds theorems can be summarised as: For (2.1), at the fixed point $\mathbf{x}^*$ there exists a unique smooth stable invariant manifold of $\mathbf{x}^*$, $W^s(\mathbf{x}^*)$, which is tangent to E^s such that for all $\mathbf{y} \in W^s$, $\varphi_t(\mathbf{y}) \to \mathbf{x}^*$ as $t \to \infty$.

Similarly, there exists a unique smooth unstable invariant manifold of $\mathbf{x}^*$, $W^u(\mathbf{x}^*)$, which is tangent to E^u such that for all $\mathbf{y} \in W^u(\mathbf{x}^*)$, $\varphi_t(\mathbf{y}) \to \mathbf{x}^*$ as $t \to -\infty$. There also exists a (non-unique) invariant manifold, $W^c(\mathbf{x}^*)$, tangent to E^c. For a rigorous treatment of the stable, unstable, and center manifold theorems, along with proofs, see Chicone [18], Meiss [40] or Perko [46].

2.1.4 Discrete Dynamical Systems

The preceding definitions in Section 2.1.2 also apply to maps, which can be considered as dynamical systems in discrete time. This is crucial when discussing the role of Poincaré maps in the stability of periodic orbits. Consider the rule $\mathbf{x} \mapsto g(\mathbf{x})$ and define φ_n as the n-th iterate by induction, $\varphi_n(\mathbf{x}) = g^n(\mathbf{x})$ where n is a positive integer. If g is invertible, then $g^{-m} = (g^{-1})^m$. The definitions from Section 2.1.2 can be applied to φ; however, if g is not invertible, only the forward asymptotic behavior can be defined.

Assume that g is a diffeomorphism (and therefore invertible). At a fixed point $\mathbf{x}^*$, consider the linearization, $A = Dg(\mathbf{x}^*)$, at that point. We can decompose E, the generalized eigenspace of A into invariant subspaces $E = E^u \bigoplus E^c \bigoplus E^s$, where the invariant subspaces of the fixed point $\mathbf{x}^*$ are:

1. The unstable subspace, E^u, which consists of the span of generalized eigenvectors with eigenvalues with modulus greater than one.

2. The center subspace, E^c, which consists of the span of generalized eigenvectors with eigenvalues with modulus equal to one.

3. The stable subspace, E^s, which consists of the span of generalized eigenvectors with eigenvalues with modulus less than one.

There are analogous invariant manifold theorems for maps, allowing E^s and E^u to be continued uniquely to invariant stable and unstable manifolds $W^s(\mathbf{x}^*)$ and $W^u(\mathbf{x}^*)$. The center subspace can also be continued (non-uniquely) to $W^c(\mathbf{x}^*)$.

2.2 Hamiltonian Dynamical Systems

2.2.1 Hamiltonian Equations of Motion

Let $H(\mathbf{q}, \mathbf{p}, t)$ be a smooth real-valued function defined on an open set of $\mathbb{R}^n \times \mathbb{R}^n \times \mathbb{R}$. The vectors $\mathbf{q}^T = (q_1, \ldots, q_n)$ and $\mathbf{p}^T = (p_1, \ldots, p_n)$ are called conjugate variables and are traditionally referred to as position and momentum vectors. However, in the case of vortex motion as discussed in Section 3.2 the canonical variables do not correspond to position and momentum. A Hamiltonian system is a system of $2n$ ODEs of the form

$$\frac{dq_i}{dt} = \frac{\partial H}{\partial p_i} \quad \text{and} \quad \frac{dp_i}{dt} = -\frac{\partial H}{\partial q_i} \tag{2.2}$$

where $i = 1, \ldots, n$. If H is independent of t, the system is said to be an autonomous system with n degrees-of-freedom.

Another formulation of a Hamiltonian system is to let $\mathbf{z}^T = [\mathbf{q}, \mathbf{p}]$ and define the symplectic matrix $\mathbb{J}$ as

$$\mathbb{J} = \begin{pmatrix} 0 & I_n \\ -I_n & 0 \end{pmatrix},$$

then the system of ODEs can be written compactly as

$$\frac{d\mathbf{z}}{dt} = \mathbb{J}\nabla H(\mathbf{z}, t). \tag{2.3}$$

2.2.2 Poisson Brackets

Poisson brackets define an algebraic structure that can be used to generalize a Hamiltonian system and are a powerful tool when working with canonical transformations. The Poisson bracket $\{\cdot,\cdot\}$ for two function F and G is defined as

$$\{F,G\} = \sum_{i=1}^{N} \left(\frac{\partial F}{\partial q_i}\frac{\partial G}{\partial p_i} - \frac{\partial F}{\partial p_i}\frac{\partial G}{\partial q_i} \right),$$

and for a general function $f(q,p,t)$ we have

$$\begin{aligned} \frac{d}{dt}f(q,p,t) &= \frac{\partial f}{\partial q}\frac{\partial H}{\partial p} - \frac{\partial f}{\partial p}\frac{\partial H}{\partial q} + \frac{\partial f}{\partial t} \\ &= \{f,H\} + \frac{\partial f}{\partial t} \end{aligned}$$

and the Poisson brackets of the canonical coordinates are

$$\{p_i,p_j\} = \{q_i,q_j\} = 0 \quad \text{and} \quad \{q_i,p_j\} = \delta_{ij}.$$

The Poisson bracket is a bilinear operator on a pair of functions in $C^2(\mathbb{R}^n \times \mathbb{R}^n \times \mathbb{R})$ which is: antisymmetric, a derivation (i.e., satisfies the Leibniz rule) and satisfies the Jacobi Identity. That is letting $F,G,H \in C^2(\mathbb{R}^n \times \mathbb{R}^n \times \mathbb{R})$, then

$$\begin{aligned} \{F,G\} &= -\{G,F\}, && \text{(Antisymmetry)} \\ \{aF+bG,H\} &= a\{F,H\} + b\{G,H\}, && \text{(Bilinearity)} \\ \{H,aF+bG\} &= a\{H,F\} + b\{H,G\}, && \text{(Bilinearity)} \\ \{FH,G\} &= F\{H,G\} + H\{F,G\}, && \text{(Leibniz Rule)} \end{aligned}$$

and

$$\{F,\{G,H\}\} + \{G,\{H,F\}\} + \{H,\{F,G\}\} = 0. \quad \text{(Jacobi Identity)}$$

Hamilton's equations of motion can now be conveniently written as

$$\frac{dq_i}{dt} = +\frac{\partial H}{\partial p_i} = \{q_i,H\} \quad \text{and} \quad \frac{dp_i}{dt} = -\frac{\partial H}{\partial q_i} = \{p_i,H\}.$$

Thus a quantity G is constant in time, i.e., an integral of motion if and only if $\{H, G\} = 0$. Two quantities, F and G, are functionally independent if their Poisson bracket vanishes. In this case we say they are *involutive* or *in involution*. This concept is critical for the reductions in Chapter 3.

2.2.3 Integrable Systems and Conserved Quantities

Two fundamental results that are used in Chapter 3 are *Noether's Theorem* and the *Liouville-Arnold* Theorem. Noether's Theorem states that if the Lagrangian is invariant under a one-parameter group of diffeomorphisms, there exists a corresponding conserved quantity. For the Hamiltonian systems under consideration this allows us to draw three conclusions

1. Invariance under translations in time yields that the value of the Hamiltonian is a conserved quantity (i.e., Energy is conserved).

2. Invariance under translations provides conservation of momentum.

3. Invariance under rotations provides conservation of angular momentum.

In most physical applications, the Lagrangian is the fundamental quantity, from which the Hamiltonian is derived using a Legendre transform. However, the point-vortex model considered in this text is the standard example of a system where the Hamiltonian is the fundamental quantity [9]. In this case, a corresponding Lagrangian can be found by inspection [44], and Noether's Theorem applies to this system.

In a Hamiltonian system with n degrees of freedom ($2n$-dimensional phase space) and k mutually involutive conserved quantities, one can reduce the phase space's dimension to $2(n - k)$. If $k = n$, the system is said to be completely integrable and, in principle, can be solved by quadrature. This system is said to be completely integrable in the sense of *Liouville integrability*.

The Liouville-Arnold Theorem further states that, under appropriate compactness conditions, there exists a canonical transformation that maps the phase space into

action-angle coordinates (I_i, θ_i) where the Hamiltonian is then a function of $\mathbf{I}$ alone so that $\dot{I}_i = 0$ and is a constant of motion. For a fixed $\mathbf{I}$, the angle variable $\boldsymbol{\theta}$ moves on the n-torus, $\mathbb{T}^n$, with a constant frequency given by $\dot{\theta}_i = \omega_i(I_i) = \frac{\partial H}{\partial I_i}$. Figure 2.1 shows a three-dimensional projection of a portion of phase space foliated by tori for an integrable Hamiltonian system with two-degrees-of-freedom. Each torus represents a separate value of $\mathbf{I}$, and the frequencies on each torus may not need be the same.

Let $\boldsymbol{\omega} = (\omega_1, \omega_2, \ldots, \omega_n)$; then if there exists $\mathbf{m} \in \mathbb{Z}^n \backslash 0$ such that $\boldsymbol{\omega} \cdot \mathbf{m} = 0$, $\boldsymbol{\omega}$ is said to be *commensurate*. If no such $\mathbf{m} \in \mathbb{Z}^n \backslash 0$ exists, the $\boldsymbol{\omega}$ is said to be incommensurate. If the frequency vector $\boldsymbol{\omega}$ is commensurate, the motion can not be dense on the torus $\mathbb{T}^n$. We illustrate this result with a standard example. Consider the two-degree-of-freedom Hamiltonian of an uncoupled oscillator with two frequencies ω_1, ω_2,

$$H(I_1, I_2) = \omega_1 I_1 + \omega_2 I_2.$$

Since $\dot{I}_1 = \dot{I}_2 = 0$, both I_1 and I_2 are constants of motion and since $\dot{\theta}_i = \omega_i$, $\theta_1 = \omega_1 t$ and $\theta_2 = \omega_2 t$. The motion can be visualized on the surface of a torus, where the two motions are *through* and *around* the hole of the torus.

In two-degrees-of-freedom, the commensurability condition simplifies to the motion being incommensurate if ω_2/ω_1 is an irrational number and quasi-periodic ω_2/ω_1 is a rational number. If $\omega_2/\omega_1 = 3/2$, we say that the frequencies are in a 3-2 resonance. In Figure 2.2 (a), a trajectory moving on the surface of the torus makes three complete revolutions *through* the hole of the torus and two complete revolutions *around* the hole before returning to its initial condition and the motion is periodic. However, if $\omega_2/\omega_1 = \sqrt{2}$, the trajectory not only does not return to its initial value, it is dense on the surface of the torus and is said to be quasi-periodic, see Figure 2.2(b).

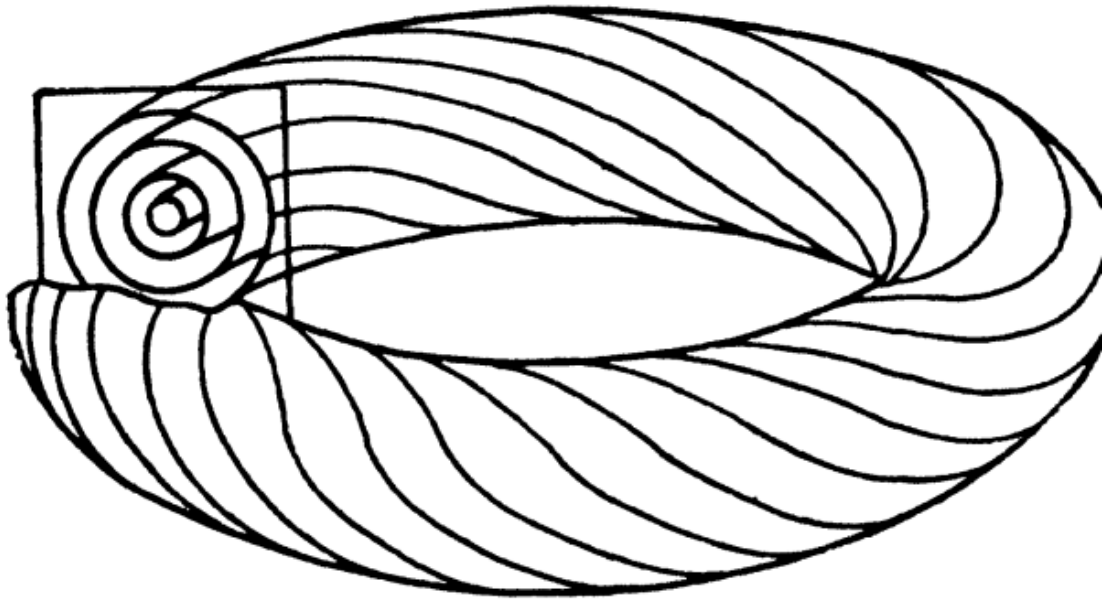

Figure 2.1 Schematic of the Liouville-Arnold Theorem from Arnold's original paper. *Source:* [24].

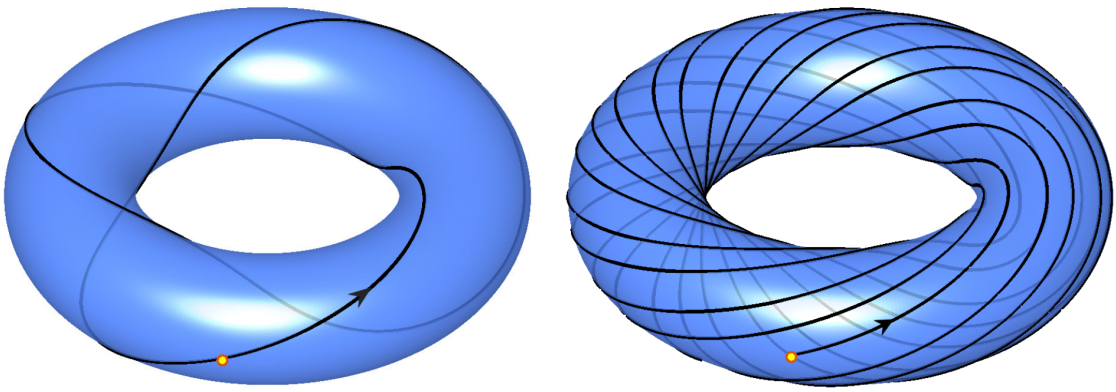

Figure 2.2 Left: (a) $\omega_2/\omega_1 = 3/2$. Right: (b) $\omega_2/\omega_1 = \sqrt{2}$. *Source: Chemistry and Mathematics in Phase Space (CHAMPS)* [4]. (Creative Commons Attribution)

2.2.4 Canonical Transformations

Canonical (or symplectic) transformations are discussed in standard graduate textbooks in classical mechanics [25,30] and we highlight a few of their relevant properties. For a Hamiltonian system, say $H(q, p, t)$, a canonical transformation to new variables (Q, P) with new Hamiltonian $K(Q, P, t) = H(q(Q, P), p(Q, P), t)$ is one that preserves the Hamiltonian structure of the equations of motion, i.e.,

$$\frac{dQ}{dt} = \frac{\partial K}{\partial P} \quad \text{and} \quad \frac{dP}{dt} = -\frac{\partial K}{\partial Q}.$$

An equivalent formulation is that a transformation is canonical if the Poisson brackets are preserved, i.e.

$$\{q_i, p_j\} = \{Q_i, P_j\} = \delta_{ij}$$

and all others vanish,

$$\{Q_i, Q_j\} = \{P_i, P_j\} = 0.$$

We use canonical transformations in two distinct ways in this project. One is to reduce the number of degrees of freedom of the system and in order to make manifest the lower degree-of-freedom system guaranteed by the Liouville-Arnold Theorem. The other is in perturbation theory, where we consider a system $H = H_0 + \epsilon H_1$ where H_0 is an integrable system with a known solution. A canonical transformation is used to transform H into a system that is (in some sense, to be defined later) more tractable.

In classical canonical perturbation theory, global generating functions create this transformation for a fixed ϵ. This approach leads to implicit equations that involve the new and old variables that cannot generally be inverted in a straightforward manner. Despite this, Delaunay calculated over 505 successive canonical transformations by hand when analyzing the motion of the Moon [12]. However, we do not discuss this

approach further and focus on the infinitesimal approach using Lie transforms, which can easily be implemented in a CAS.

2.2.5 Rescaling Time Parameter

As explained in Chapter 3, the Hamiltonian for the N-Vortex problem contains a logarithmic singularity. To regularize the singularity and for algebraic convenience, we consider the equivalent Hamiltonian $f(H)$ where $f \in C^2(\mathbb{R})$ and f is monotonically increasing, $f'(H) > 0$. This reparameterizes time, but the trajectories and levels sets of the corresponding systems still coincide. The new time parameter can be found by a simple application of the chain rule. For a system

$$\tilde{H}\left(\tilde{p}\left(\tau\right), \tilde{q}\left(\tau\right)\right) = f\left(H\left(p\left(t\right), q\left(t\right)\right)\right)$$

with equations of motion

$$\frac{dp}{dt} = \frac{\partial H}{\partial q} \quad \text{and} \quad \frac{dq}{dt} = -\frac{\partial H}{\partial p},$$

the chain rule

$$\begin{aligned} \frac{\partial \tilde{H}}{\partial \tilde{q}} &= \frac{\partial f(H)}{\partial H}\frac{\partial H}{\partial q} \\ &= f'(H)\frac{\partial H}{\partial q}, \end{aligned}$$

together with

$$\frac{dq}{dt} = \frac{d\tilde{q}}{d\tau}\frac{d\tau}{dt} \quad \text{and} \quad \frac{dp}{dt} = \frac{d\tilde{p}}{d\tau}\frac{d\tau}{dt}$$

imply that

$$\frac{d\tilde{p}}{d\tau}\frac{d\tau}{dt} = \frac{1}{f'(H)}\frac{\partial \tilde{H}}{\partial \tilde{q}} \quad \text{and} \quad \frac{d\tilde{q}}{d\tau}\frac{d\tau}{dt} = -\frac{1}{f'(H)}\frac{\partial \tilde{H}}{\partial \tilde{p}}.$$

If $\tau = \frac{1}{f'(H)}t$, the Hamiltonian structure of the equations of motion are preserved, i.e.,

$$\frac{d\tilde{q}}{d\tau} = \frac{\partial \tilde{H}}{\partial \tilde{p}} \quad \text{and} \quad \frac{d\tilde{p}}{d\tau} = -\frac{\partial \tilde{H}}{\partial \tilde{q}}.$$

2.2.6 Linear Hamiltonian Systems

Linear Hamiltonian systems are ubiquitous in the study of the stability of equilibrium and periodic orbits. When Taylor expanding around a critical point $\mathbf{z}^*$ or a periodic orbit $\mathbf{z}^*(t)$ in a Hamiltonian system,

$$H(\mathbf{z}) = H(\mathbf{z}^*) + \frac{1}{2}(\mathbf{z}-\mathbf{z}^*)^T S(\mathbf{z}-\mathbf{z}^*) + O(||\mathbf{z}-\mathbf{z}^*||^3) \tag{2.4}$$

where S is the Hessian of H at $\mathbf{z}^*$ and from (2.3), the equations of motion are

$$\frac{d\mathbf{z}}{dt} = \mathbb{J}S\mathbf{z}. \tag{2.5}$$

Matrices of the form $A = \mathbb{J}S$, where S is a symmetric matrix, define the set of Hamiltonian matrices. These $2n \times 2n$ matrices form a Lie algebra known as $\mathrm{sp}(2n, \mathbb{R})$ [28, 41]. The corresponding fundamental matrix solutions to (2.5), $Z(t, t_0)$, with $Z(t_0, t_0)$ are known as symplectic matrices and form the Lie group $\mathrm{Sp}(2n, \mathbb{R})$.

It can be shown [40, 41, 65] that if λ is an eigenvalue of a Hamiltonian matrix A, then so is $-\lambda$. Moreover, the characteristic polynomial of A is even. If A is real, then its characteristic polynomial is real and its eigenvalues come in complex conjugate pairs. Thus the eigenvalues come in four possible groupings:

(a) Hyperbolic (saddle): λ is real. Then there is a pair of eigenvalues $\{\lambda, -\lambda\}$.

(b) Elliptic (center): $\lambda = i\omega$ is imaginary. Then $-\lambda = \bar{\lambda}$ and the eigenvalues comes in a pair $\{i\omega, -i\omega\}$.

(c) Krein quartet: λ is complex and $\mathrm{Re}(\lambda) \neq 0$ so that there is a quartet of eigenvalues $\{\lambda, -\lambda, \bar{\lambda}, -\bar{\lambda}\}$.

(d) Parabolic: A double eigenvalue $\lambda = 0$.

2.3 Stability of Periodic Orbits

In this section, we consider four tightly related concepts: the Poincaré map, linearized perturbation equations, Floquet theory, and Hill's determinant. These concepts are

interrelated and must be understood together to understand our approach to the stability of periodic orbits.

2.3.1 Poincaré Maps

Poincaré maps are the primary tool for analyzing and visualizing behavior such as the flow near a periodic orbit by reducing a continuous dynamical system to a discrete dynamical system in a lower-dimensional space. Consider a general continuous dynamical system of the form of ODE given by (2.1) with a periodic solution $\bar{\mathbf{x}}(t) = \bar{\mathbf{x}}(t+T)$ of period T. Take any point in which the periodic solution passes, say $\mathbf{x}_0$. The *Poincaré Surface of Section* (PSS) at $\mathbf{x}_0$, $\Sigma_{\mathbf{x}_0}$, is a $(n-1)$-hypersurface which intersects the periodic orbit transversely at $\mathbf{x}_0$. To guarantee transversality, we take the surface of section to be orthogonal to the flow:

$$\Sigma_{\mathbf{x}_0} = \{\mathbf{x} : (\mathbf{x} - \mathbf{x}_0) \cdot f(\mathbf{x}_0) = 0\}. \tag{2.6}$$

Utilizing the PSS, the Poincaré map P is defined in a neighborhood of $\mathbf{x}_0$ by the first return to the surface of section under the flow given by f, see Figure 2.3. The transversality condition (2.6) is satisfied in an open set $U_{\mathbf{x}_0} \in \Sigma_{\mathbf{x}_0}$ but can be extended provided that tangencies with trajectories of (2.1) can be avoided. The Poincaré map P of first return is, therefore, a map from $U_{\mathbf{x}_0} \mapsto U_{\mathbf{x}_0}$, allowing for the standard theory of discrete dynamical systems to be applied. Since, by construction, $P(\mathbf{x}_0) = \mathbf{x}_0$, $\mathbf{x}_0$ is a fixed point of P and we can examine the invariant manifolds at the fixed point $\mathbf{x}_0$, Figure 2.5, see Section 2.1.4. These one-dimensional manifolds of $\mathbf{x}_0$ can also be understood of projections of the two-dimensional manifolds of the periodic orbit $\boldsymbol{\gamma}$ projected onto the plane Σ.

The eigenvalues of the linearization at the fixed point, $DP\mathbf{x}_0$, can be used to determine the fixed point's stability, $\mathbf{x}_0$.

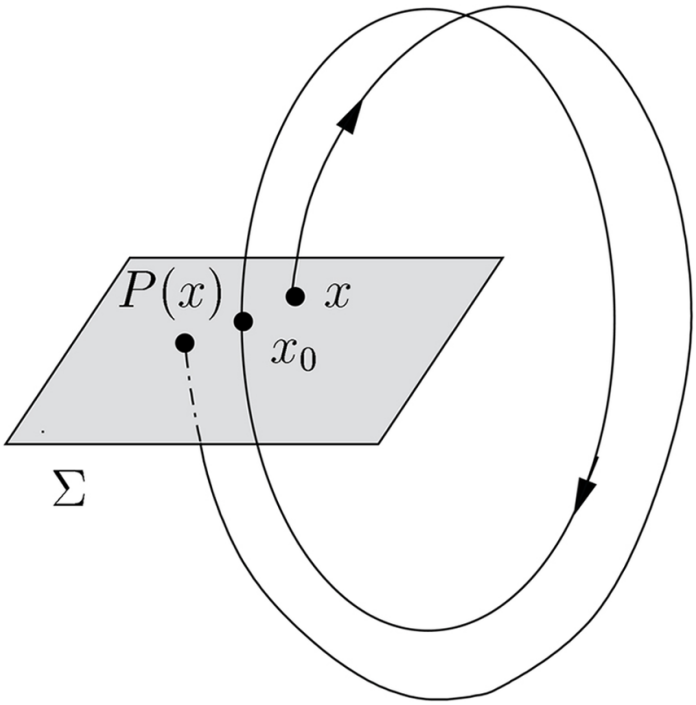

Figure 2.3 Schematic of a Poincaré of first return, Wiggins [63].

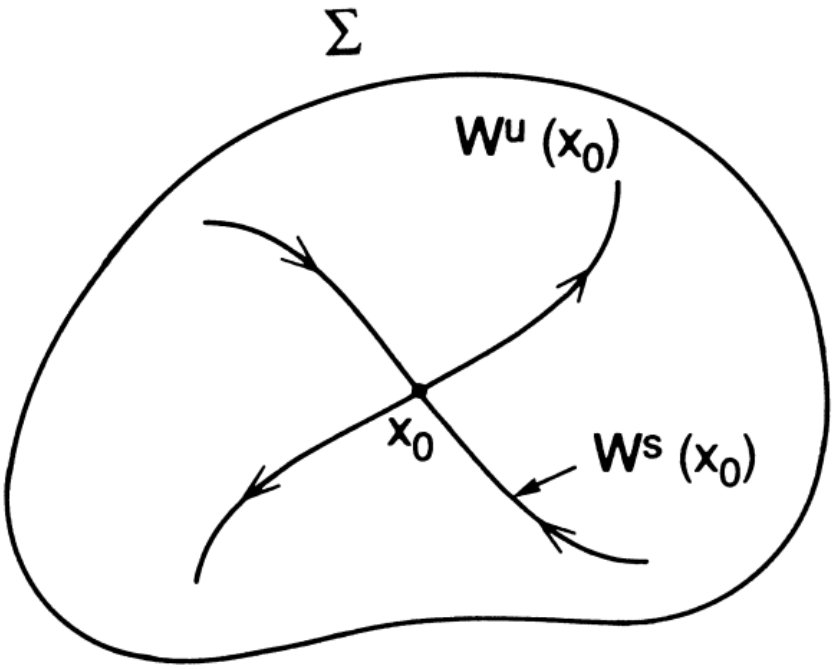

Figure 2.4 Schematic of Poincaré Map $P : \Sigma \to \Sigma$ with the one-dimensional unstable manifold $W^{\mathrm{u}}(\mathbf{x}_0)$ and the one-dimensional stable manifold $W^{\mathrm{s}}(\mathbf{x}_0)$ of the saddle-type fixed point at $\mathbf{x}_0$., *Source: Wiggins* [63].

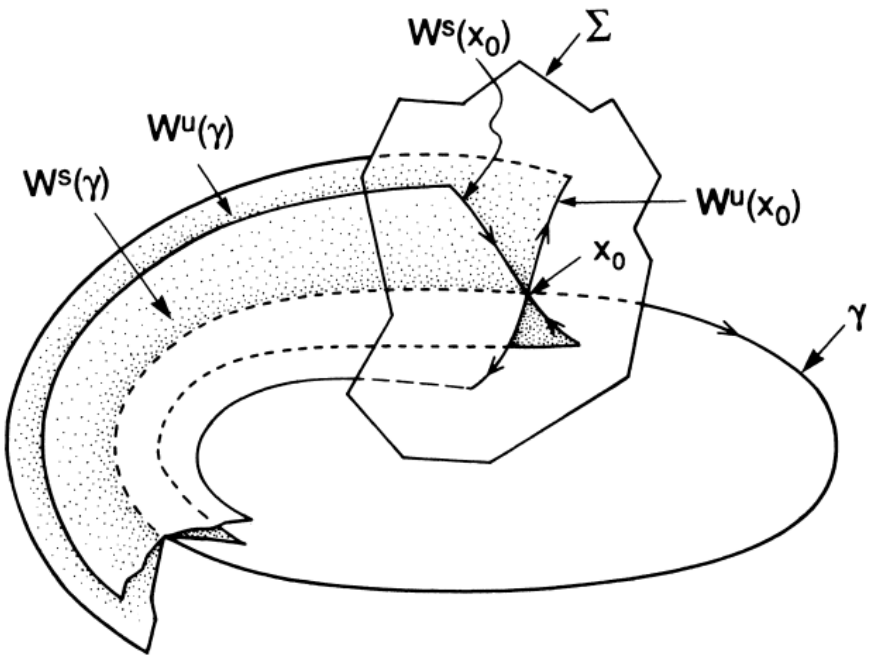

Figure 2.5 Schematic of the PSS Σ along the periodic orbit $\boldsymbol{\gamma}$ with the unstable manifold $W^{\mathrm{u}}(\mathbf{x}_0)$ and stable manifold $W^{\mathrm{s}}(\mathbf{x}_0)$ of the saddle at $\mathbf{x}_0$ along with the stable and unstable two-dimensional manifolds of the periodic orbit, $\boldsymbol{\gamma}$. *Source:* , *Wiggins* [63].

2.3.2 Linearized Perturbation Equations

Again consider a continuous dynamical system of the form of ODE given by (2.1) with a periodic solution $\bar{\mathbf{x}}$. Consider a perturbed trajectory

$$\mathbf{x}\left(t\right)=\bar{\mathbf{x}}\left(t\right)+\boldsymbol{\xi}\left(t\right)$$

then, to first-order,

$$\frac{d\boldsymbol{\xi}}{dt}=Df\left(\bar{\mathbf{x}}\left(t\right)\right)\boldsymbol{\xi}$$

where $Df\left(\bar{\mathbf{x}}\left(t\right)\right)$ is the (time-periodic) Jacobian matrix of the flow field f evaluated along the periodic orbit $\bar{\mathbf{x}}\left(t\right)$. Following the arguments in Section 2.2.6, the linearizaed perturbation equations of a periodic orbit $\bar{\mathbf{x}}\left(t\right)$ in a Hamiltonian system are

$$\frac{d\boldsymbol{\xi}}{dt}=\mathbb{J}S(t)\boldsymbol{\xi}, \tag{2.7}$$

where $S(t)$ is the Hessian of H evaluated along the periodic orbit $\bar{\mathbf{x}}(t)$. The behavior of linear equations with periodic coefficients is analyzed using Floquet Theory in Section 2.3.3.

2.3.3 Floquet Theory

In studying the stability of periodic orbits, linear systems with periodic coefficients naturally arise through the process of linearization about the periodic solution, as seen in Section 2.3.2. The mathematical tool used to study these systems is known as Floquet theory. The behavior of a linear system whose coefficients are periodic in time does not depend on the local behavior of the solutions, but rather on the solutions integrated over one period.

Consider a general n-dimensional linear system

$$\dot{\mathbf{x}} = A(t)\mathbf{x}, \quad \mathbf{x}(t_0) = \mathbf{x}_0 \tag{2.8}$$

where $A(t+T) = A(t)$. In particular the linearized perturbation equations (2.7) are of this form. The general solution is represented in terms of the fundamental matrix $\Phi(t, t_0)$ which solves

$$\dot{\Phi} = A(t)\Phi, \quad \Phi(t_0, t_0) = I. \tag{2.9}$$

The stability of these solutions is determined by the monodromy matrix, $M = \Phi(T, 0)$, where M is interpreted as a discrete map describing the evolution of the solution over one period. The eigenvalues of M are called the Floquet multipliers. In the important case where (2.8) arises from the linearization about a periodic orbit, the monodromy matrix is closely related to the linearization of the Poincaré map given by (2.3.1). In general, the monodromy matrix, M is an $n \times n$ matrix which includes an eigenvalue of 1 along the direction of the periodic orbit. Switching to a basis whose first element is a

vector perpendicular to $\Sigma_{\mathbf{x}_0}$, the restriction of M on the remaining $(n-1)$-dimensional space is the linearization of the Poincaré map.

Floquet's theorem [18, 65] states that the fundamental solution matrix can be decomposed as $\Phi(t,0) = P(t)e^{tF}$ where P is a periodic matrix, $P(t+T) = P(t)$ for all t, and F is independent of t. The interpretation of this theorem utilized in Section 2.4 is that P transforms (2.9) to a problem with constant coefficients. Let $Y(t) = \Phi(t,0)$ and consider P to be a transformation, which is invertible since solutions to equation (2.9) are unique, into new variables $Z = P^{-1}Y$. Then

$$\begin{aligned}\frac{dZ}{dt} &= \frac{d}{dt}\left(P^{-1}(t)P(t)e^{tF}\right) = \frac{d}{dt}\left(e^{tF}\right)\\ &= Fe^{tF} = FP^{-1}(t)P(t)e^{tF}\\ &= FP^{-1}(t)Y(t) = FZ(t).\end{aligned}$$

and P is a (Lyapunov) transformation that takes the linear ODE (2.9) with time-periodic coefficients to a linear ODE with constant coefficients. We use this perspective when discussing an algorithm that produce approximations for P and F in Section 2.4.

Hamiltonian Floquet Theory When analyzing the stability of a periodic orbit in a two-degree-of-freedom Hamiltonian system, the linearization will be a 4×4 linear Hamiltonian system, which must have at least one-pair of eigenvalues with $|\lambda| = 1$ corresponding to the motion tangent to the periodic orbit. The system can then be decoupled, and the stability depends on $A(t)$, which is a 2×2 Hamiltonian matrix. The Floquet multipliers of A comes in pairs λ_1 and λ_2 such that $\lambda_1\lambda_2 = 1$. If $\lambda_{1,2}$ have a nonzero imaginary part, then the two multipliers must lie on the unit circle and be conjugate. If $\lambda_{1,2}$ are real and $|\lambda_1| \neq 1$, then one multiplier lies inside the unit circle, and the other lies outside the unit circle and the system is unstable. On the

boundary between stability and instability, the two eigenvalues must lie on the unit circle and be real-valued, i.e., they must satisfy $\lambda_1 = \lambda_2 = \pm 1$.

If the system depends continuously on the parameter α then the Floquet multipliers of A_α depend continuously on α [65]. Therefore, bifurcations, i.e., changes in stability, can only occur at values of α where $\lambda_1 = \lambda_2 = \pm 1$. The existence of a multiplier $\lambda = 1$ (respectively $\lambda = -1$) corresponds to the existence of a periodic orbit with period T (respectively, an anti-periodic orbit of half-period T). The stability or instability is easily determined by examining $\mathrm{tr}(M) = \lambda_1 + \lambda_2$, with stability in the case $|\mathrm{tr}(M)| < 2$ and instability when $|\mathrm{tr}(M)| > 2$. At the bifurcation values, $\mathrm{tr}\, M = 2$ and $\mathrm{tr}\, M = -2$, the system (2.8) has a periodic orbit or an anti-periodic orbit, respectively.

2.3.4 Method of Harmonic Balance and the Hill's Determinant

As noted in Section 2.3.3, at parameter values where the system undergoes a bifurcation, there must exist either a periodic orbit or an anti-periodic orbit. The idea behind the method of harmonic balance is that if such an orbit exists, it has a convergent Fourier series, which can be found if an approximate solvability condition for its coefficients is satisfied. In this section, we provide a brief overview of the method. For a thorough classical overview, see [62].

In his 1886 account of the motion of the lunar perigee [29], Hill considered what has come to be known as Hill's equation

$$\ddot{x} = g_\alpha(t)x(t), \quad \text{where} \quad g_\alpha(t + 2\pi) = g(t). \tag{2.10}$$

This can be put in the standard Floquet form (2.8) with coefficient matrix $A(t, \alpha) = \left(\begin{smallmatrix} 0 & 1 \\ g_\alpha(t) & 0 \end{smallmatrix}\right)$. Hill formally found a relationship between the trace of the required monodromy matrix M_α and the coefficients forming the Fourier series of $g_\alpha(t)$. Hill's result, in a modern notation, can be summarized as follows. If g_α has Fourier

expansion,

$$g_\alpha(t) = \sum_{k=-\infty}^{\infty} g_k(\alpha) e^{ikt}, \qquad g_k \in \mathbb{C}, \tag{2.11}$$

then the infinite matrix, $H_\alpha = (h_{mk}(\alpha))$, with components

$$h_{mk}(\alpha) = \frac{k^2 \delta_{mk} + g_{k-m}(\alpha)}{k^2 + 1}, \qquad m, k \in \mathbb{Z}, \tag{2.12}$$

where δ_{ij} is the Kronecker delta, has determinant

$$|H_\alpha| = \frac{\mathrm{tr}(M_\alpha) - 2}{e^{2\pi} + e^{-2\pi} - 2}. \tag{2.13}$$

Notice that if the system (2.10) has a periodic orbit at parameter value α, then $\mathrm{tr}(M_\alpha) = 2$ and $|H_\alpha| = 0$.

In 1899, Poincaré proved the convergence of Hill's formula and gave a rigorous definition of the determinant of the infinite matrix H_α [47]. Hill's infinite determinant can also be given a variational interpretation as the Hessian of the action functional evaluated at the critical value given by the periodic orbit. This quantity can provide useful information regarding the stability of the periodic solution via the Morse index [13, 56].

In the study of bifurcations, the vanishing of Hill's determinant has a natural interpretation: it is a solvability condition for the values of the parameter α at which there exists either a periodic orbit or an anti-periodic orbit, which indicates that the system may undergo a change of stability. The most familiar example of an equation in Hill's form is Mathieu's equation, in which the coefficient takes the form $g = c + d\cos 2t$. Consider the ansatz where the solution to (2.10), $x(t)$, is periodic and has Fourier expansion

$$x(t) = \sum_{k=-\infty}^{\infty} x_m e^{imt}, \qquad x_j \in \mathbb{C}. \tag{2.14}$$

We seek a solvability condition for the existence of a non-trivial solution, $x(t)$. Putting (2.11) and (2.14) into (2.10) and collecting harmonics yields the formal series

$$\begin{aligned} -\ddot{x}(t) + g(t)x(t) &= \sum_{k=-\infty}^{\infty} \sum_{m=-\infty}^{\infty} \left(m^2 + g_k(\alpha)e^{ikt}\right) x_m e^{imt} \\ &= \sum_{k,m=-\infty}^{\infty} \left(k^2\delta_{mk} + g_{k-m}(\alpha)\right) x_m e^{imt} \\ &\equiv \sum_{k,m=-\infty}^{\infty} h_{mk}(\alpha) x_m e^{imt} = 0. \end{aligned} \tag{2.15}$$

This defines a matrix of infinite order, $H(\alpha) = (h_{km}(\alpha))$.

Consider a sequence of finite-dimensional matrices H_N^{trunc} obtained by truncating this system at the Nth harmonic, i.e., only including terms k and m such that $-N \leq k, m \leq N$. The matrix H_N^{trunc} has dimension $(2N+1) \times (2N+1)$. As $N \to \infty$, the roots of the equation $|H_N^{\text{trunc}}(\alpha)| = 0$ should converge to the roots of $|H(\alpha)|$.[1]

2.4 Perturbative Techniques

2.4.1 The Lie-Deprit Algorithm

In the 1960s, Lie-Deprit methods were invented as a new approach to canonical perturbation theory. Rather than defining the canonical transformation in terms of mixed variables created by a generating function, the canonical transformation is defined as the flow in ϵ of a new Hamiltonian W. The flow in ϵ is described by a Hamiltonian to guarantee that the transformations are symplectic. This method can be extended to non-Hamiltonian ODEs [31]; however, the Hamiltonian case is particularly elegant as the system can be defined in terms of the scalar quantity W. This framework can also be used to guarantee that the transformations are, for example, unitary by having the auxiliary ODE describing the flow in ϵ be linear with

[1]Note that equations (2.12) and (2.15) differ by a factor of $\frac{1}{1+k^2}$. This is a regularization factor to guarantee $h_{jj} = 1$ and is necessary for (2.13) to converge.

a skew-symmetric matrix [17]. We present the algorithm as described by Meyer and Hall [41]. For a summary of the history and different approaches, see the review article [15].

Consider a Hamiltonian, $H_*(\epsilon, x)$, that has formal expansion in terms of ϵ,

$$H_*(\epsilon, x) = \sum_{i=0}^{\infty} \frac{\epsilon^i}{i!} H_i^0(x). \tag{2.16}$$

The algorithm computes how H_* changes under the change of coordinates generated by a given Hamiltonian $W(\epsilon, x)$. Consider the flows with respect to ϵ given by

$$\frac{dx}{d\epsilon} = \mathbb{J}\nabla W(\epsilon, x), \tag{2.17}$$

with initial conditions $x(0) = y$ where W is a smooth function. This equation has a smooth solution $X(\epsilon, y)$ such that $X(0, y) = y$. Since (2.17) is a Hamiltonian system $X(\epsilon, y)$ induces a near-identity symplectic change of variables, i.e., $X(\epsilon, y)$ is a canonical change of coordinates when $x = X(\epsilon, y)$ is considered as a change of coordinates that depends on ϵ and $X(\epsilon, y) = y + O(\epsilon)$.

Using a Lie transform, the new Hamiltonian $H^*(\epsilon, y) = H(\epsilon, X(\epsilon, y))$ can be expressed in the coordinates generated by the change of variables generated by (2.17). Let

$$H^*(\epsilon, y) = \sum_{i=0}^{\infty} \frac{\epsilon^i}{i!} H_0^i(y), \tag{2.18}$$

$$W(\epsilon, x) = \sum_{i=0}^{\infty} \frac{\epsilon^i}{i!} W_{i+1}(y), \tag{2.19}$$

$$X^*(\epsilon, y) = \sum_{i=0}^{\infty} \frac{\epsilon^i}{i!} X_0^i(y), \tag{2.20}$$

then the following fundamental recursive identities are the basis of the forward algorithm describing the flow generated by W along ϵ

$$H_j^i = H_{j+1}^{i-1} + \sum_{k=0}^{j} \{H_{j-k}^{i-1}, W_{k+1}\} \tag{2.21}$$

and

$$X_j^i = X_{j+1}^{i-1} + \sum_{k=0}^{j} \{X_{j-k}^{i-1}, W_{k+1}\}. \tag{2.22}$$

We ultimately want to construct H^* and X^* that depend on H_0^n and X_0^n. We can visualize the dependencies in (2.21) (2.22) by the Lie-Deprit triangle:

$$\begin{array}{ccccc}
H_0^0 & & & & \\
\downarrow & & & & \\
H_1^0 & \longrightarrow & H_0^1 & & \\
\downarrow & & \downarrow & & \\
H_2^0 & \longrightarrow & H_1^1 & \longrightarrow & H_0^2 \\
\downarrow & & \downarrow & & \downarrow
\end{array}$$

All this assumes we know W_i, so the question remains: how do we pick W_i? This choice depends on the choice of the form we want H_0^n to take to be considered 'simple"–for example removing the higher-order terms up to that order. Finding W_i requires solving an ODE of the form

$$H_0^n = L_j^i + \{H_0^0, W_n\}, \tag{2.23}$$

for W_n where L_j^i is a combination of known quantities from earlier iterations. This equation is known as the homological or Lie equation and is similar in spirit to the equations encountered at each order in ϵ to remove resonant terms in other methods used to find normal forms. An explicit application of this algorithm is given in Appendix C.

2.4.2 The Magnus Expansion

The Magnus expansion is a method to construct a formal solution of the the form $Y(t) = \exp \Omega(t)$ of the ODE

$$Y'(t) = A(t)Y(t)$$

with $Y(0) = I$. This can be contrasted with Dyson's formal solution in terms of the time-ordering operator $\mathcal{T}$,

$$Y(t) = \mathcal{T}\left(\exp \int_0^t A(s)ds\right)$$

which was first used to prove the equivalence of Feynman's, Schwinger's, and Tomanga's frameworks of Quantum Electrodynamics [20].

The Magnus expansion is used to construct a formal series solution $\Omega(t) = \sum_{k=1}^{\infty} \Omega_k(t)$ by integrating the differential equation

$$\frac{d\Omega}{dt} = \sum_{n=0}^{\infty} \frac{B_n}{n!} \mathrm{ad}_{\Omega}^n A,$$

where B_n are the Bernoulli numbers and $\mathrm{ad}_{\Omega} B := [\Omega, B]$. The first few integrations lead to

$$\begin{aligned}
\Omega_1(t) &= \int_0^t A(t_1)dt_1, \\
\Omega_2(t) &= \frac{1}{2}\int_0^t dt_1 \int_0^{t_1} dt_2 [A(t_1), A(t_2)], \\
\Omega_3(t) &= \frac{1}{6}\int_0^t dt_1 \int_0^{t_1} dt_2 \int_0^{t_2} dt_3 \left([A(t_1), [A(t_2), A(t_3)]] + [A(t_3), [A(t_2), A(t_1)]]\right).
\end{aligned}$$

There exist recursive algorithms for this expansion [11], which are of benefit when using symbolic manipulators. It can be shown that for all orders, Ω_n is given in terms of commutators. Thus the truncated expansions Ω_n are still in the same Lie algebra as the A_n's.

2.4.3 The Casas Algorithm

Casas and collaborators [16] have constructed a perturbative algorithm for approximating the fundamental solution matrix of a linear periodic system given as an asymptotic series. The method is the combination of three ideas explored in this chapter—the Magnus expansion, the Lyapunov transform, and Lie transform perturbation theory—to construct an approximation to the monodromy matrix of a linear Hamiltonian system with periodic coefficients. There exist other algorithms to construct solutions to the Floquet problem [65] perturbatively; however, this method has two significant advantages. The Magnus expansion has the advantage that the approximate fundamental solution operator is always in the same Lie algebra as the exact operator. As the systems under consideration here are Hamiltonian, this means the approximate fundamental solution matrix is symplectic. Additionally, since the algorithm is based on Lie transformations, the solution procedure is also recursive and easy to code in a CAS.

Consider the Floquet problem

$$\frac{\partial Y(t,\epsilon)}{\partial t} = A(t,\epsilon)Y(t,\epsilon) \sim \left(A_0 + \sum_{k=1}^{\infty} A_k(t)\epsilon^k\right) Y(t,\epsilon).$$

with $Y(0,\epsilon) = I$ and $A_n(t+T) = A_n(t)$. Floquet's theorem proves the existence of a solution $Y(t,\epsilon) = P(t)e^{tF}$ where $P(t) = P(t+T)$ but is non-constructive. The idea of this solution is to construct Lyapunov transformations P to a given order in ϵ,

$$Z(t,\epsilon) = P^{-1}(t,\epsilon)Y(t,\epsilon)$$

that will make the equation

$$\frac{\partial Z(t,\epsilon)}{\partial t} = K(t,\epsilon)Z(t,\epsilon).$$

with

$$K(t,\epsilon) = P^{-1}(t,\epsilon)A(t,\epsilon)P(t,\epsilon) + \frac{\partial P^{-1}(t,\epsilon)}{\partial t}P(t,\epsilon) \tag{2.24}$$

such that the expansion of the matrix $K(t,\epsilon)$ is constant-valued up to the order constructed.

Using the idea behind Lie transforms for Hamiltonian systems, $P(t,\epsilon)$ is a near-identity transformation (thus invertible) which evolve in ϵ according to

$$\frac{\partial P^{-1}(t,\epsilon)}{\partial \epsilon} = L(t,\epsilon)P^{-1}(t,\epsilon) \tag{2.25}$$

with $P^{-1}(t,0) = I$.

As of now, $L(t,\epsilon)$ is unknown. At the final step, we can obtain L by requiring K to be independent in time to a given order in ϵ and forcing L to be periodic. That is, by requiring L to be a Lyapunov transform.

We can formally solve (2.25) by use of the Magnus expansion to get

$$P^{-1}(t,\epsilon) = \exp\Omega(t,\epsilon) = \exp\left(\Sigma_{m=1}^{\infty}\Omega_m(t,\epsilon)\right). \tag{2.26}$$

Using (2.25) and differentiating (2.24) with respect to ϵ, we have

$$\frac{\partial K}{\partial \epsilon} = [L,K] + P^{-1}\frac{\partial A}{\partial \epsilon}P + \frac{\partial L}{\partial t}.$$

It is convenient to use the identity $e^{\Omega}Be^{-\Omega} = e^{\mathrm{ad}_\Omega}B$ (see [28]) to write this as

$$\frac{\partial K}{\partial \epsilon} = [L,K] + e^{\mathrm{ad}_\Omega}\frac{\partial A}{\partial \epsilon} + \frac{\partial L}{\partial t}. \tag{2.27}$$

We now wish to write all these expressions as power series in ϵ,

$$K(t,\epsilon) = \sum_{n=0}^{\infty}\epsilon^n K_n(t) \tag{2.28}$$

$$L(t,\epsilon) = \sum_{n=0}^{\infty}\epsilon^n L_{n+1}(t) \tag{2.29}$$

$$e^{\mathrm{ad}_\Omega}\frac{\partial A}{\partial \epsilon} = \sum_{n=0}^{\infty}\epsilon^n w_n(t). \tag{2.30}$$

The w_n can be solved for by inserting (2.28) into the Magnus expansion and collecting terms. The first few terms are

$$\begin{aligned} w_0 &= A_1, \\ w_1 &= 2A_2 + [L_1, A_1], \\ w_2 &= 3A_3 + 2[L_1, A_2] + \frac{1}{2}[L_2, A_1] + \frac{1}{2}[L_1, [L_1, A_1]]. \end{aligned}$$

There exist recursive formulas [17] for the term w_n that can be programmed into a symbolic manipulator. In principle, once these are found, they can be stored and reused for any problem. In practice, it is faster to write code that finds w_n by putting A into the defining recursive relations than to insert A into the explicit formula.

Putting (2.28) into (2.27) and collecting terms in ϵ, we arrive at an inhomogeneous first order linear ODE for L_n for $n \geq 1$,

$$\frac{dL_n}{dt} = \mathrm{ad}_{A_0} L_n + nK_n - F_n \tag{2.31}$$

where $K_0 = A_0$, F_n satisfies the recursion relation

$$\begin{aligned} F_1 &:= w_0 = A_1 \\ F_n &:= \sum_{j=1}^{n-1} [L_{n-j}, K_j] + w_{n-1}. \end{aligned}$$

and K_n is determined by averaging (2.31) with the requirement that K_n be time independent. We find the forms of L_n (and thus P) by requiring it to be a Lyapunov transformation. Letting $\langle A(t) \rangle$ be the average of A over one period, the average of (2.31) is

$$nK_n = \langle F_n \rangle - [A_0, \langle L_n \rangle]. \tag{2.32}$$

We can also easily solve the ODE (2.31) and insert (2.32) with $L_n(0) = 0$,

$$\begin{aligned} L_n(t) &= e^{t\mathrm{ad}_{A_0}} \int_0^t e^{-s\mathrm{ad}_{A_0}} \left(nK_n - F_n(s)\right) ds \\ &= \left(I - e^{t\mathrm{ad}_{A_0}}\right) \langle L_n \rangle + \int_0^t e^{(t-s)\mathrm{ad}_{A_0}} \left(\langle F_n \rangle - F_n(s)\right) ds. \end{aligned}$$

Requiring L_n to be periodic, we have $L_n(T) = 0$ so that

$$\left(e^{T\mathrm{ad}_{A_0}} - I\right) \langle L_n \rangle = \int_0^T e^{(T-s)\mathrm{ad}_{A_0}} \left(\langle F_n \rangle - F_n(s)\right) ds, \tag{2.33}$$

which allows us to solve for $\langle L_n \rangle$ and thus K_n and L_n. The solution for $\langle L_n \rangle$ is not unique, so we are free to pick the simplest $\langle L_n \rangle$ that solve the *matrix* equation (2.33).

2.5 KAM Theory and the Nature of Hamiltonian Chaos

While we will not make rigorous use of KAM theorems in this dissertation, understanding the history and development of KAM theory and its conclusions provides a conceptual blueprint for understanding the phenomena observed in later Chapters where we focus on numerically computed results. However, KAM theory will provide a conceptual blueprint for the observed phenomena. Many of the phase space structures observed in Chapter 7 of the non-integrable Hamiltonian are 'integrable-like-behavior' that can be understood and interpreted using the vocabulary of KAM theory.

The standard framework for this problem is to examine the perturbation of an integrable system. Poincaré considered understanding the nature of these systems as the fundamental problem of dynamics [47]. In this section, we consider the standard example of a *nearly integrable Hamiltonian system* which is a Hamiltonian in N degrees-of-freedom of the form

$$H(\boldsymbol{\theta}, \mathbf{I}) = H_0(\mathbf{I}) + \epsilon H_1(\boldsymbol{\theta}, \mathbf{I}) \text{ where } I_i \in \mathbb{R}^+ \text{ and } \theta_i \in S^1. \tag{2.34}$$

where H_0 is an integrable system, $\epsilon > 0$ is small, and H_1 is a well-behaved function (e.g. smooth).

2.5.1 The Problem of Small Divisors

The perturbation techniques described in Section 2.4 contains an underlying unjustified assumption—that the perturbed Hamiltonian can be transformed into an integrable one. By a process such as averaging, the system is transformed into an integrable one. Stated geometrically, the torus, $\mathbb{T}^n$, of the unperturbed system provided by the Liouville-Arnold Theorem stays intact. In a one degree-of-freedom system, this is not an issue since the system is necessarily integrable. However, a priori, there is no reason to expect the perturbed system to retain this structure for two or more degrees-of-freedom.

To see the problem that can arise, consider the first iteration of the Lie series (2.23) applied to the system system (2.34). The homological equation becomes

$$H_0^1 = H_1(\boldsymbol{\theta}, \mathbf{I}) + \{H_0(\mathbf{I}), W(\boldsymbol{\theta}, \mathbf{I})\}$$

where

$$\{F, G\} = \sum_{i=1}^{N} \left(\frac{\partial F}{\partial \theta_i} \frac{\partial G}{\partial I_i} - \frac{\partial F}{\partial I_i} \frac{\partial F}{\partial \theta_i} \right).$$

Assume that H_1 and W can be expanded as Fourier series,

$$W(\boldsymbol{\theta}, \mathbf{I}) = \sum_{\mathbf{m}} W_{\mathbf{m}}(\mathbf{I}) e^{i\boldsymbol{\theta}\cdot\mathbf{m}}, \tag{2.35}$$

$$H_1(\boldsymbol{\theta}, \mathbf{I}) = \sum_{\mathbf{m}} H_{1,\mathbf{m}}(\mathbf{I}) e^{i\boldsymbol{\theta}\cdot\mathbf{m}}, \tag{2.36}$$

where the sums are taken over all sets of integers $\mathbf{m} = \{m_1, m_2, \ldots, m_n\}$ where $m_k \in \mathbb{Z}$ and $\|\mathbf{m}\| \neq 0$. Putting the expansions (2.35) into the homological equation (2.5.1)

while noting that the unperturbed frequencies are $\omega_k = \frac{\partial H_0(\mathbf{I})}{\partial I_i}$ and $\frac{\partial H_0(\mathbf{I})}{\partial \theta_i} = 0$,

$$\begin{aligned}
H_0^1 &= H_1(\boldsymbol{\theta}, \mathbf{I}) + \{H_0(\mathbf{I}), W(\boldsymbol{\theta}, \mathbf{I})\} \\
&= H_1(\boldsymbol{\theta}, \mathbf{I}) + \sum_{i=1}^{N} \left(\frac{\partial H_0(\mathbf{I})}{\partial \theta_i} \frac{\partial W(\boldsymbol{\theta}, \mathbf{I})}{\partial I_i} - \frac{\partial H_0(\mathbf{I})}{\partial I_i} \frac{\partial W(\boldsymbol{\theta}, \mathbf{I})}{\partial \theta_i} \right) \\
&= H_1(\boldsymbol{\theta}, \mathbf{I}) - \sum_{i=1}^{N} \omega_i \frac{\partial W(\boldsymbol{\theta}, \mathbf{I})}{\partial \theta_i} \\
&= \sum_{\mathbf{m}} H_{1,\mathbf{m}}(\mathbf{I}) e^{i\boldsymbol{\theta}\cdot\mathbf{m}} - \sum_{i=1}^{N} \sum_{\mathbf{m}} \omega_i m_i W_{\mathbf{m}}(\mathbf{I}) e^{i\boldsymbol{\theta}\cdot\mathbf{m}} \\
&= \sum_{\mathbf{m}} \left(H_{1,\mathbf{m}}(\mathbf{I}) - i \left(\boldsymbol{\omega} \cdot \mathbf{m} \right) W_{\mathbf{m}}(\mathbf{I}) \right) e^{i\boldsymbol{\theta}\cdot\mathbf{m}},
\end{aligned}$$

To make H_0^1 independent of $\boldsymbol{\theta}$, the generating function W must have Fourier coefficients

$$W_{\mathbf{m}}(\mathbf{I}) = \frac{H_{1,\mathbf{m}}(\mathbf{I})}{i \left(\boldsymbol{\omega} \cdot \mathbf{m} \right)}. \tag{2.37}$$

The central problem is now clear: if there are any resonances in the frequencies $\boldsymbol{\omega}$ (i.e., $\boldsymbol{\omega}(\mathbf{I}) \cdot \boldsymbol{m} = 0$), the perturbation series diverges. Even though the set of values for which the denominator is zero is countable and can be removed, the remaining values can still be made arbitrarily large leading to the divergence of the sum (2.35). It is not obvious how to proceed as this roadblock originates from *true* resonances of the unperturbed system, suggesting that the series can not be made to converge.

Poincaréś concerns over a series of this type drove the formulation of the modern geometrical view of dynamical systems in 1889. However, he could not fully resolve the question of small divisors (this would have to wait until the 1950s). He did note that there is a real phenomenon that could lead to the divergence of these series for an infinite number of starting conditions. This observation of this phenomenon, now known as a *homoclinic* tangle, is widely considered the beginning of the modern theory of chaos. In Poincaréś own words [47]:

> When one tries to depict the figure formed by these two curves and their infinity of intersections, each corresponding to a [homoclinic orbit] these intersections form a sort of trellis, web, or infinitely tight mesh; neither of the two curves can ever intersect itself but must fold back on itself in a very complex way in order to intersect all the links of the mesh infinitely many times.
>
> One is struck by the complexity of this figure that I shall not even attempt to draw. Nothing is better suited to give us an idea of the complexity of the three-body problem and all of the problems of dynamics in general where there is no uniform integral and [the perturbation] series diverge.

2.5.2 KAM Theory

Kolmogorov first elucidated a new approach to this problem in his 1954 talk to the International Congress of Mathematics (also reprinted in Abraham and Marsden's Foundation of Mechanics [1]). Arnold [24] and Moser [42] filled in the details of this program for Hamiltonian systems and maps. These results, along with later refinements and adaptations, have become to be known as KAM theory.

The Key Ideas of Kolmogorov The central elements of a KAM Theorem are (loosely)

1. Instead of computing corrections sequentially in a power series expansion $H = H_0 + \epsilon H_1 + \epsilon^2 H_2 + \ldots$, use Newton's methods for Banach spaces to create a sequence of approximations $h_0, h_1, \ldots$ that are 'superconvergent'.

2. A Diophantine criteria for when ω is poorly approximated by rationals or insufficiently incommensurate. A vector $\boldsymbol{\omega}$ is said to be Diophantine if there exist $\gamma > 0$ and $\tau > n - 1$ such that

$$\boldsymbol{\omega} \in \mathcal{D}_{\gamma,\tau} = \{\boldsymbol{\omega} \in \mathbb{R}^n : \ |\boldsymbol{\omega} \cdot \mathbf{m}| > \gamma / \|\boldsymbol{\omega}\|^\tau \ \text{ for all } \mathbf{m} \in \mathbb{Z}^n\}.$$

3. A notion of non-degeneracy or twist condition, for example $\det(D^2 H_0) = 0$. This guarantees that in a neighborhood of a given $\mathbf{I}$ there is exists a bijection with the frequencies vectors $\boldsymbol{\omega}$.

A typical KAM result tells us that for a nearly integrable Hamiltonian system (2.34) and a sufficiently nice H_1, e.g. H_1 is smooth, and H_0 satisfies an appropriate non-degeneracy condition, then for sufficiently small ϵ and an appropriate $\gamma > 0$, there exists invariant tori whose frequencies are proportional to each $\boldsymbol{\omega} \in \mathcal{D}_{\gamma,\tau}$. The perturbed flow is quasi-periodic at these frequencies, and the Lebesgue measure of these frequencies increases to the full measure of the set as $\epsilon \to 0$.

How KAM Theory is Utilized in this Dissertation The visual picture that comes alongside KAM theory is important in Chapters 6 and 7. Not only did Arnold provide a proof for a KAM theorem, but he also elucidates the qualitative behind it. It is straightforward to visualize the KAM structure numerically, but remarkably, Arnold was able to visualize this complex behavior at the heart of Hamiltonian chaos without using numerics.

The resonances that gave Poincaré so much difficulty lead to a new phenomenon. The circular cross-sections of the integrable Hamiltonian in Figure 2.1 have new fixed points, alternating as saddles and centers that arise due to the perturbation, see Figure 2.6 and Figure 2.8. These are referred to as *island chains* and are due do to resonances at which the Diophantine condition fails. At the saddles, we observe the formation of a heteroclinic tangle as the separatrix between the two saddle-type fixed points splits into stable and unstable manifolds of the saddle which intersect an infinite number of times, see Figure 2.7. These are the trellises that Poincaré was able to imagine, but not able to draw. These tangles lead to chaos as they are equivalent to a Smale horseshoe map [**?**]. However, this chaotic motion is, in general, not ergodic—it remains constrained by the remaining tori. We encounter many examples of this in Chapters 6 and 7. For the two-degree-of-freedom systems

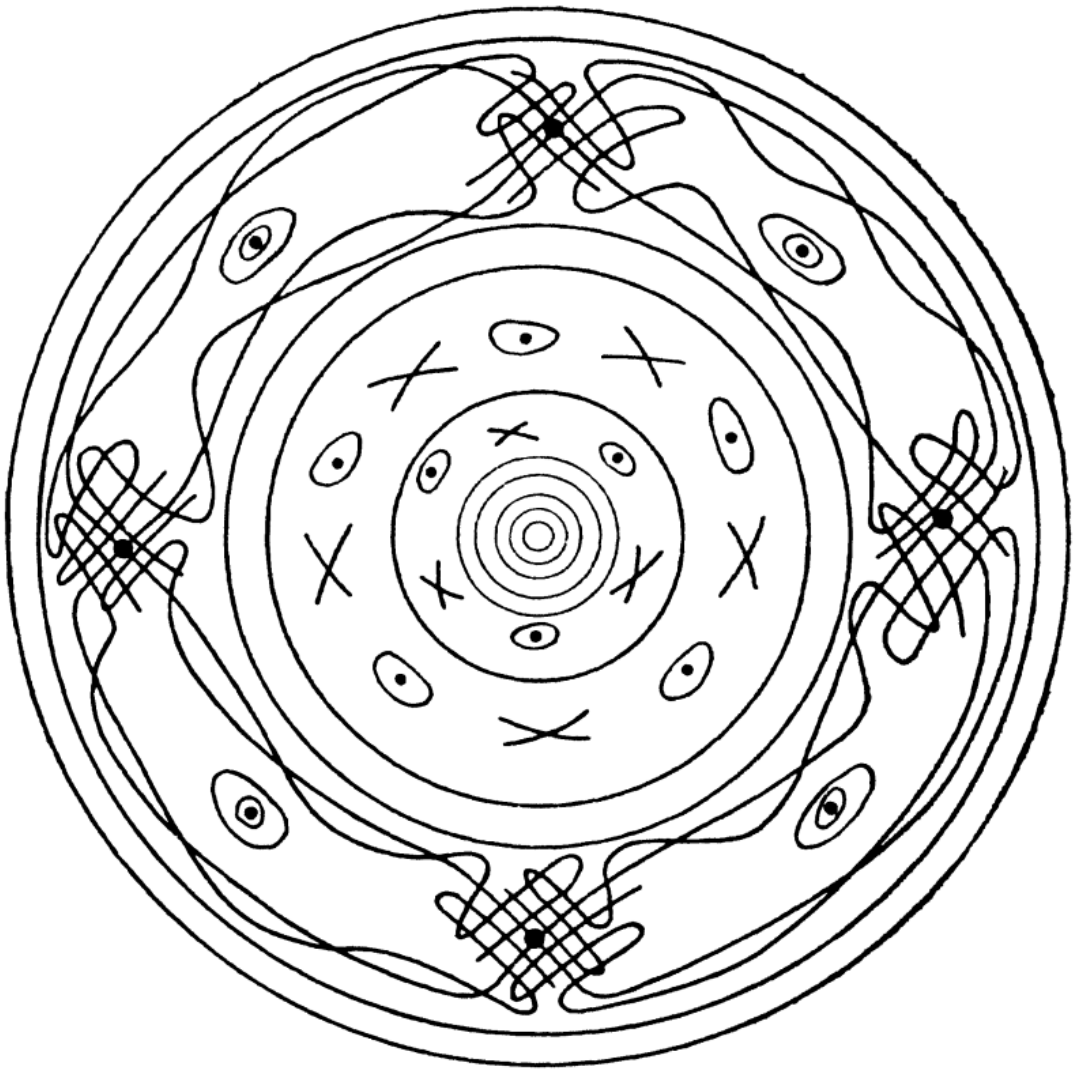

Figure 2.6 Schematic of KAM Tori from Arnold's original article. *Source:* [24].

considered in this dissertation, these barriers constrain the motion and form barriers to the chaotic motion.

Remark 2.5.1. *Since this dissertation focuses only on one and two-degree-of-freedom systems, the KAM tori form barriers in which points from inside can not be mapped to the outside. In higher degrees-of-freedom, trajectories can leak out through a process known as Arnold diffusion, albeit often only for exponentially long time scales.*

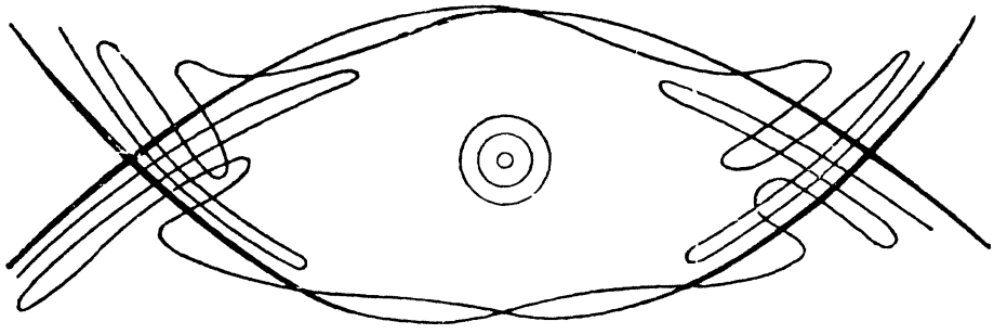

Figure 2.7 Schematic of Heteroclinic Tangles from Arnold's original article. *Source:* [24].

2.6 Lagrangian Descriptors

2.6.1 Introduction

Beginning with the modern era of the study of differential equations, which began with Poincaré's heralded study of the three-body problem [47], an overarching goal of the discipline has been to understand the geometric structures in phase-space that govern the behavior of sets of trajectories. In this dissertation, we utilize the method of Lagrangian descriptors (LD), first introduced by Madrid and Mancho, to describe Lagrangian transport processes in fluid dynamics [35] and later adapted to continuous dynamical systems [36] and to discrete dynamical systems [23]. It has also found a home in the study of chemical reactions [3]. This approach provides a way to characterize trajectories with qualitatively distinct dynamical behavior. Unlike traditional techniques such as Poincaré surface of section, LD renders visible the invariant manifolds present inside the stochastic layers and the KAM tori expected from the PSS. The LD method allows for the simultaneous visualization of both bounded and unbounded orbits, including escape regions, in a manner not possible with PSS.

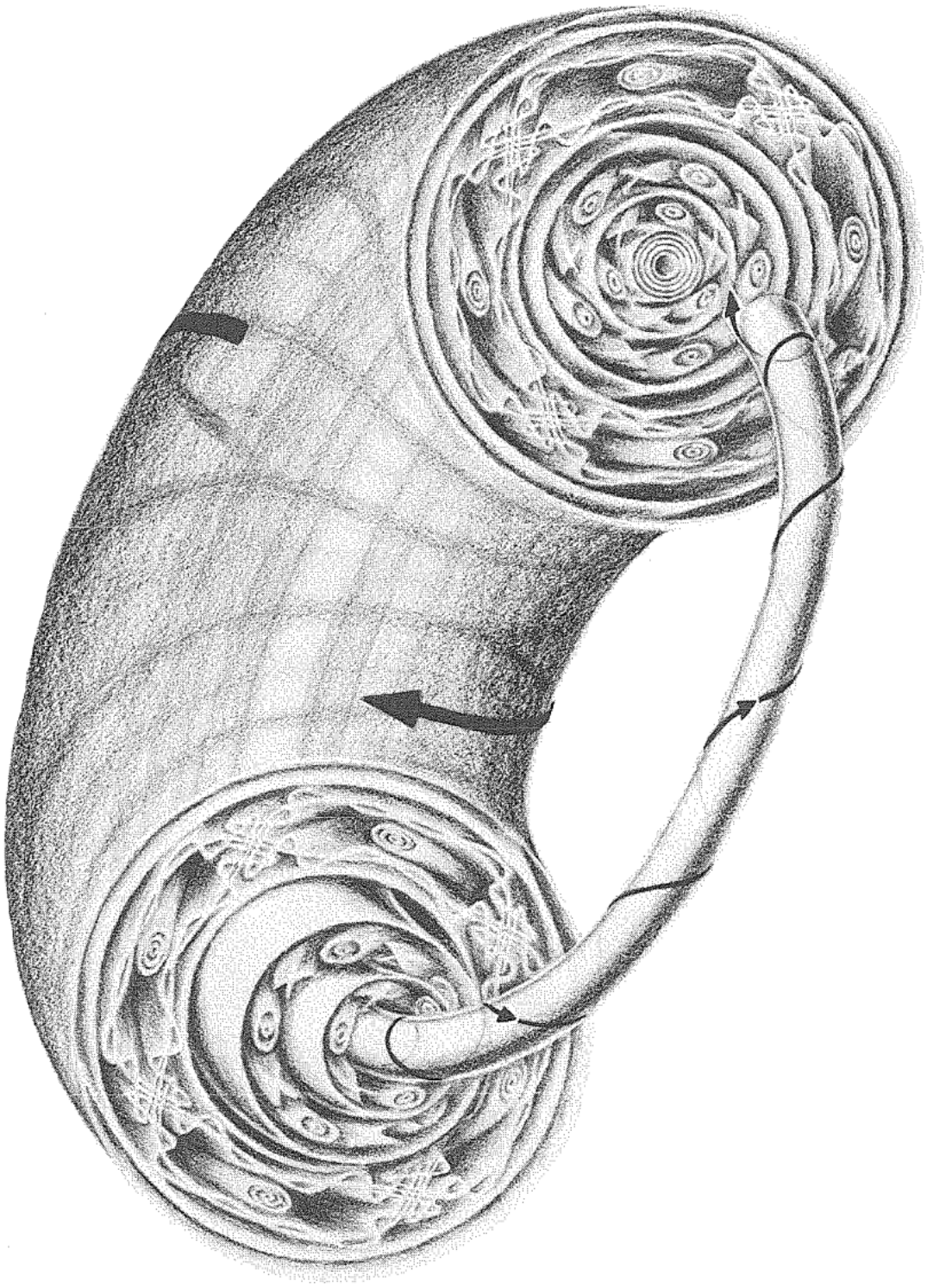

Figure 2.8 A three-dimensional projection of the KAM torus from Foundations of Mechanics. *Source:* [1].

2.6.2 Original Definition

To build intuition, first, consider the original formulation given by Madrid and Mancho [35] as it best illustrates the fundamental concept behind the approach. This method evokes the idea behind the Lagrangian description of fluid dynamics—by selecting an initial 'particle' of fluid and tracking its flow with time. The simplest definition of a Lagrangian descriptor is a function that maps each point to the arclength of the trajectory beginning at that point, forward or backward in time over a fixed time interval. Formally, consider a general continuous dynamical system,

$$\frac{d\mathbf{x}}{dt} = \mathbf{v}(\mathbf{x}, t) \tag{2.38}$$

where $\mathbf{v}$ is a continuously differentiable function of $\mathbf{x} \in \mathbb{R}^n$ and continuous in $t \in \mathbb{R}$whose. Let $\mathbf{x}(t, \mathbf{x}_0)$ be the unique solution to (2.38) with initial condition $\mathbf{x}(t_0) = \mathbf{x}_0 \in \mathbb{R}^n$. For each such initial condition $\mathbf{x}_0$, define non-negative scalar valued functions M^{f} and M^{b} by

$$\begin{aligned} M^{\mathrm{f}}(\mathbf{x}_0, t_0, \tau) &= \int_{t_0}^{t_0+\tau} \|\mathbf{v}(\mathbf{x}(t, \mathbf{x}_0), t)\| \, dt. \\ M^{\mathrm{b}}(\mathbf{x}_0, t_0, \tau) &= \int_{t_0-\tau}^{t_0} \|\mathbf{v}(\mathbf{x}(t, \mathbf{x}_0), t)\| \, dt. \end{aligned} \tag{2.39}$$

That is, $M^{\mathrm{f}}(\mathbf{x}_0, t_0, \tau)$ is the arc length of the trajectory starting at $\mathbf{x}(t_0)$ after a time τ in forward time, and $M^{\mathrm{b}}(\mathbf{x}_0, t_0, \tau)$ is the arc-length in backwards time. Plotting the forward-time (respectively, backward-time) descriptor allows visualization of the stable (respectively, unstable) manifold. The sum of these quantities

$$M(\mathbf{x}_0, t_0, \tau) = M^{\mathrm{f}}(\mathbf{x}_0, t_0, \tau) + M^{\mathrm{b}}(\mathbf{x}_0, t_0, \tau), \tag{2.40}$$

can be used to simultaneously visualize both invariant manifolds.

2.6.3 The p-psuedonorm

It has been observed that the original definition of Lagrangian descriptors (2.39) are continuous but non-differentiable along with invariant structures in phase space, allowing them to distinguish between the stable and unstable manifolds respectively. However, it has not been analytically demonstrated that they are, in fact, singular along with invariant manifolds. In the next section, we provide a modified definition that is more amenable to rigorous analysis. An alternate definition, defined for $p \in (0, 1]$ by

$$M_p(\mathbf{x}_0, \tau) = \sum_{k=1}^{n} \int_{t_0-\tau}^{t_0+\tau} |v_k(\mathbf{x}(t, \mathbf{x}_0), t)|^p \, dt \tag{2.41}$$

has been rigorously demonstrated to contain singularities in $|\nabla M_p|$ [33]. However it can not be as simply interpreted as an arclength-like-quantity as can (2.39).

Discrete Time Lagrangian Descriptors While this paper makes use of (2.41); for many regions, the *discrete time Lagrangian descriptor*(DTLD) yields a more precise visualization of the underlying phase space.

$$MD_p(\mathbf{x}_0, N) = \sum_{i=-N}^{N-1} \|\mathbf{x}_{i+1} - \mathbf{x}_i\|_p^p \tag{2.42}$$

As with the continuous time Lagrangian descriptors, the DTLD is split into forward and backward iterations

$$MD_p(\mathbf{x}_0, N) = MD_p^+(\mathbf{x}_0, N) + MD_p^-(\mathbf{x}_0, N) \tag{2.43}$$

where

$$\begin{aligned} MD_p^+(\mathbf{x}_0, N) &= \sum_{i=0}^{N-1} \|\mathbf{x}_{i+1} - \mathbf{x}_i\|_p^p \\ MD_p^-(\mathbf{x}_0, N) &= \sum_{i=-N}^{N-1} \|\mathbf{x}_{i+1} - \mathbf{x}_i\|_p^p \, . \end{aligned} \tag{2.44}$$

2.6.4 Modifications for Open Hamiltonians

For open Hamiltonians, i.e., Hamiltonian systems possessing unbounded trajectories, the definitions must be modified in the case that solutions escape to infinity in finite (continuous) time less than τ or discrete time less than N. In such systems, one restricts the flow to a finite region region $\mathcal{R}$, and replaces τ in upper limit of the integral (2.41) with $\min(\tau, t_{\mathcal{R}})$ where $t_{\mathcal{R}}$ is the minimum time for the solution to exit the region, i.e.,

$$\tau_{\mathbf{x}_0^{\pm}} = \min_{\mathbf{x}(t^{\pm};\mathbf{x}_0)\notin\mathcal{R}} \left\{\tau_0, \left|t^{\pm}\right|\right\}.$$

and the definition is then modified accordingly,

$$M_p(\mathbf{x}_0,\tau) = \sum_{k=1}^{n} \int_{t_0-\tau_{\mathbf{x}_0^-}}^{t_0+\tau_{\mathbf{x}_0^+}} |v_k(\mathbf{x}(t,\mathbf{x}_0),t)|^p \, dt. \tag{2.45}$$

The same modification can be made for unbounded maps, where instead of a fixed maximum number of iterations, we choose a variable number of iterations.

Remark 2.6.1. *For Lagrangian descriptors, the descriptors' actual values, M_p, do not provide information about the underlying phase space. Rather, it is the singularities of the gradient of those values, $|\nabla M_p|$, that provide information about the invariant structures. To best demonstrate changes in the gradient, we have chosen to use a cyclic colormap rather than a sequential colormap.*

2.6.5 An Example: Hamiltonian Pitchfork Bifurcation of a Periodic Orbit

We now provide an example to demonstrate the material discussed in Section 2.3, Section 2.5, and earlier in the present section. We use as our example the bifurcation of the leapfrogging orbit, which is the subject of Chapter 5 of this dissertation. Whitchurch et al. [61] showed numerically that this is a Hamiltonian pitchfork bifurcation. In this well-known phenomenon, a system possesses a stable periodic orbit on one side of a bifurcation, and a saddle type periodic orbit flanked by two

stable periodic orbits on the other side of the bifurcation. In the PSS, this appears as a family of nested ellipses on one side of the bifurcation and as a figure-eight shape on the other side. The figure-eight curve is formed by the stable and unstable manifolds of the hyperbolic orbit. These manifolds generally split and give rise to a homoclinic tangle as the parameter is increased further. The PSS plot does not provide a direct visualization of this tangle, but the LD plot does.

In Chapter 5, the problem is formulated such that the bifurcation occurs when a certain parameter $h = \frac{1}{8}$, with stability for smaller values. Here we present a number of PSS and LD plots, as well as some numerically-calculated invariant manifolds, for a sequence of increasing values of h, using a coordinate system due to Aref described in 4.4. At $h = 0.11$, the Hamiltonian map has one stable fixed point, see the PSS plot in Figure 2.9. As expected from KAM theory, this fixed point is surrounded by resonant island chains. As h is increased beyond the bifurcation value to $h = 0.126$, the stable fixed point becomes unstable, and two new fixed points are created, see Figure 2.10. We consider $h = 0.129$ in Figure 2.11 and 2.12. Both the PSS and LD plots show a small homoclinic tangle in a neighborhood the origin. The PSS plot more clearly reveals the island chains and the KAM tori that separate them, while the LD plot clearly indicates the existence of tangled invariant manifolds on the exterior region. Finally, we consider $h = 0.135$ in Figure 2.13 and 2.14. There are no longer any island chains around the unstable fixed point and the tangles exterior to the figure-eight region intersect the tangles at the origin as is clearly visible in the LD plot without having to manually calculate any invariant manifold. Without prior knowledge of the unstable fixed point at the origin, the PSS would no longer provide any information of the saddle; however, the invariant manifolds of the saddle are immediately apparent from examining the LD plot.

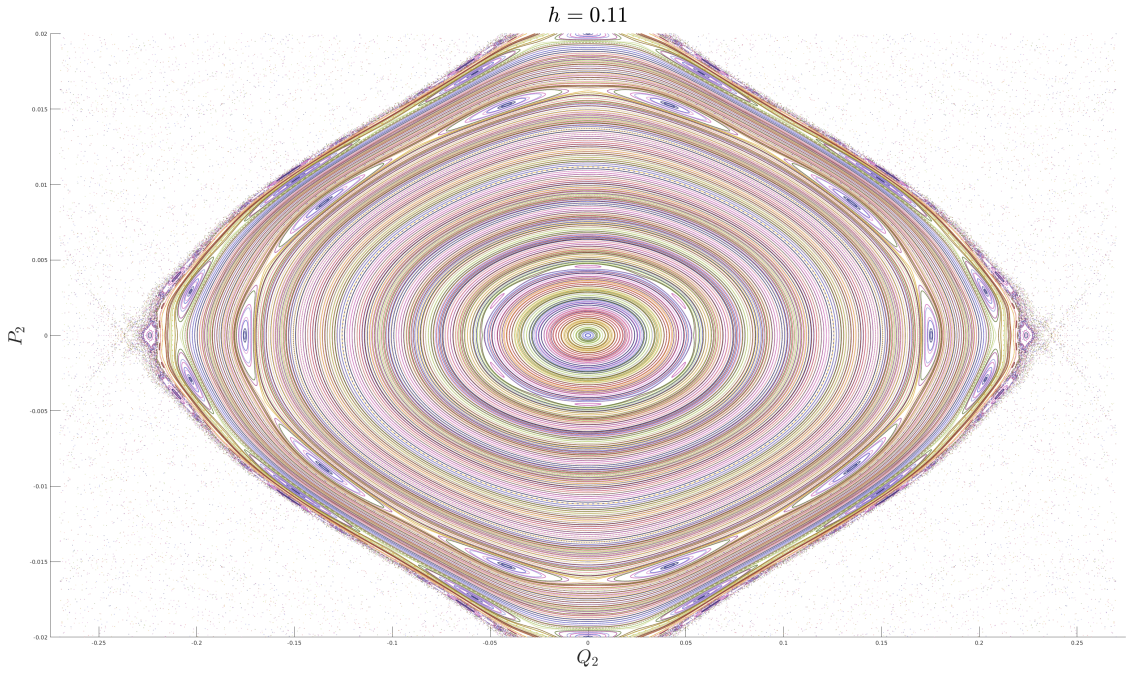

Figure 2.9 PSS for $h = 0.11 < 0.125$ when the leapfrogging orbit is a stable fixed point.

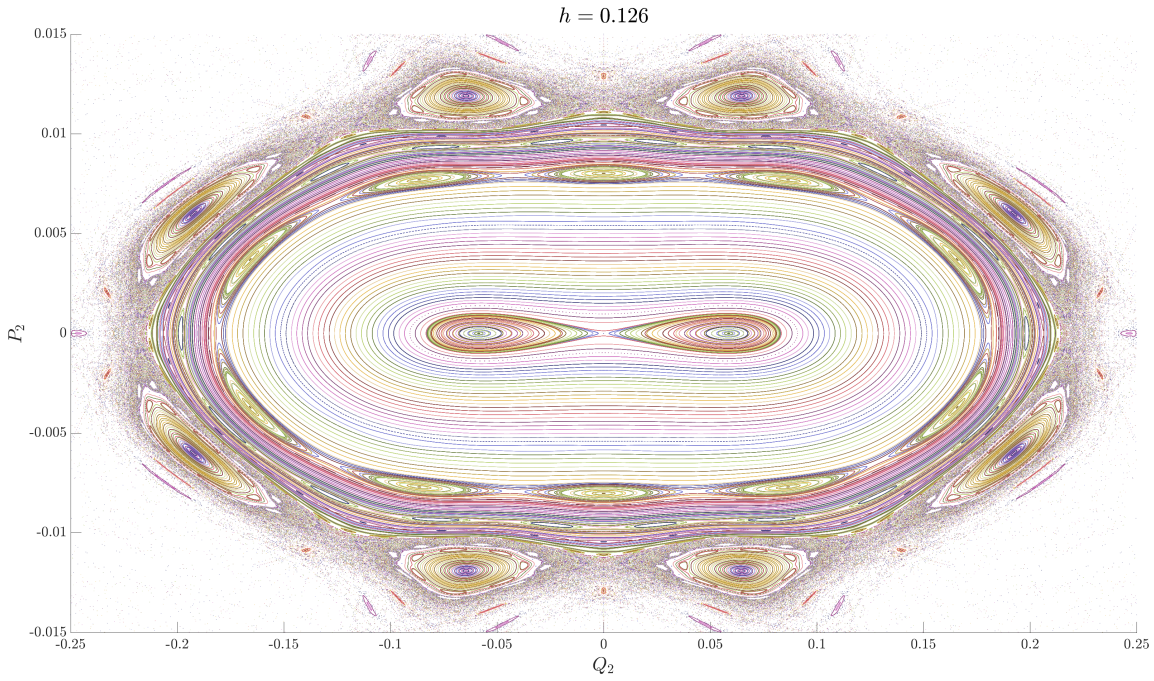

Figure 2.10 PSS for $h = 0.126 > 0.125$ when the leapfrogging orbit is an unstable fixed point.

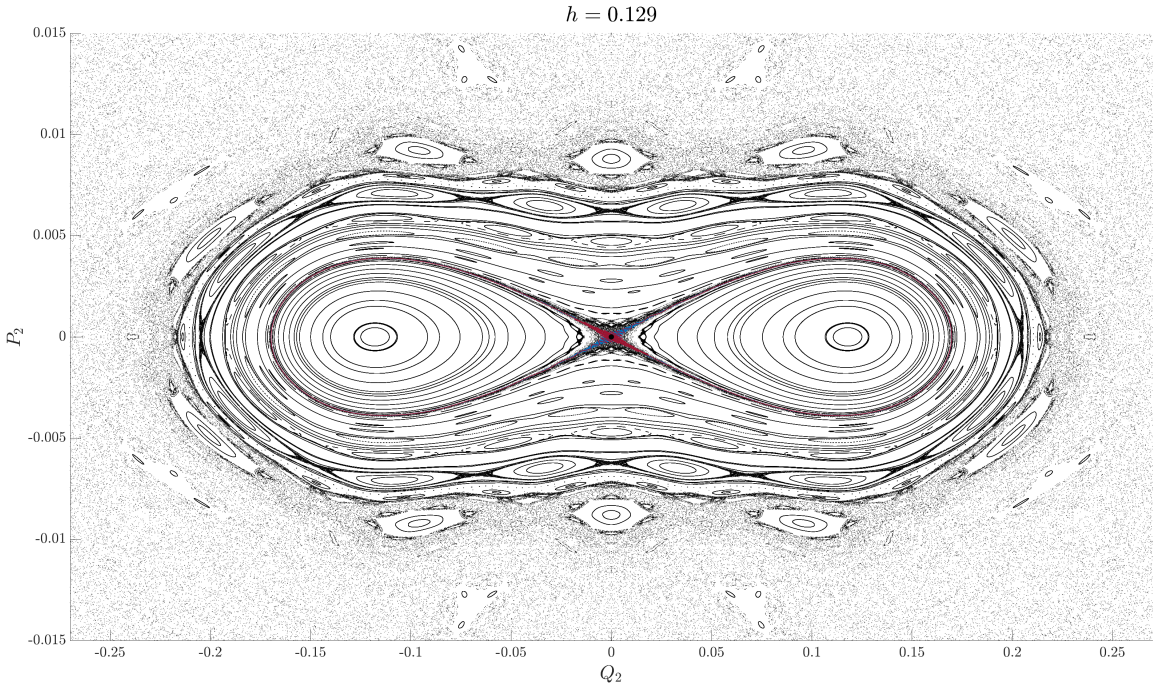

Figure 2.11 PSS near the Leapfrogging orbit in Aref-Eckhardt coordinates for $h = 0.129$. Observe the KAM tori enclosing the three fixed points formed after the pitchfork bifurcation. Stable and unstable manifolds of the hyperbolic or in blue and red, respectively.

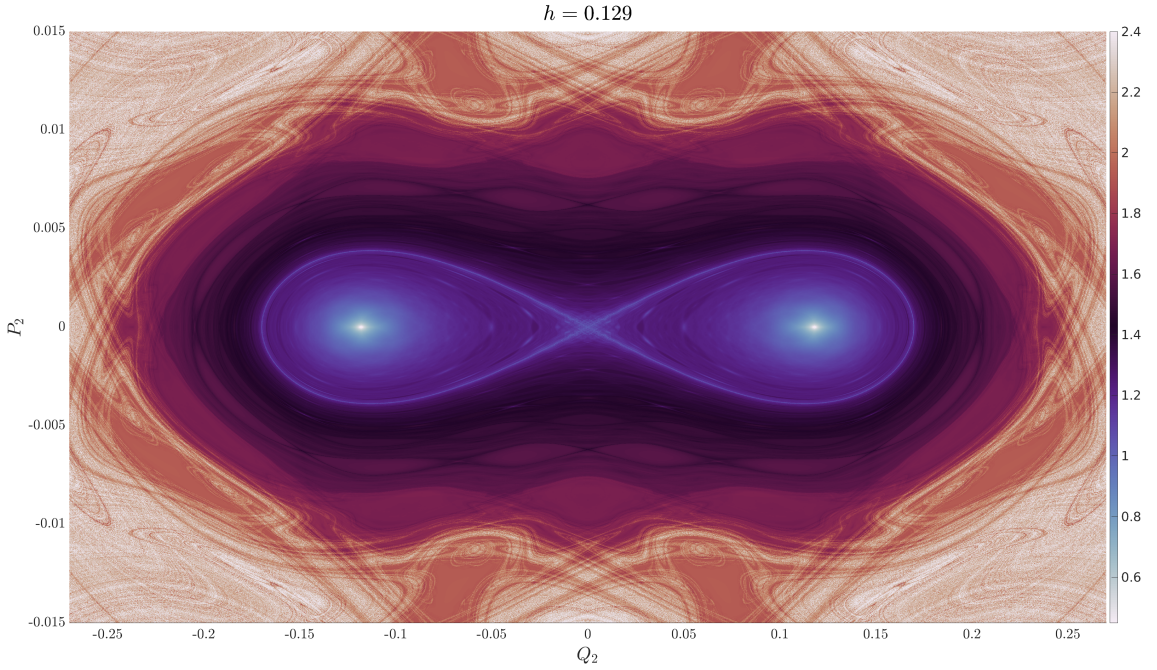

Figure 2.12 PSS near the Leapfrogging orbit in Aref-Eckhardt coordinates for $h = 0.129$. Observe the lack of overlap of the resonances in the island chain between the KAM tori.

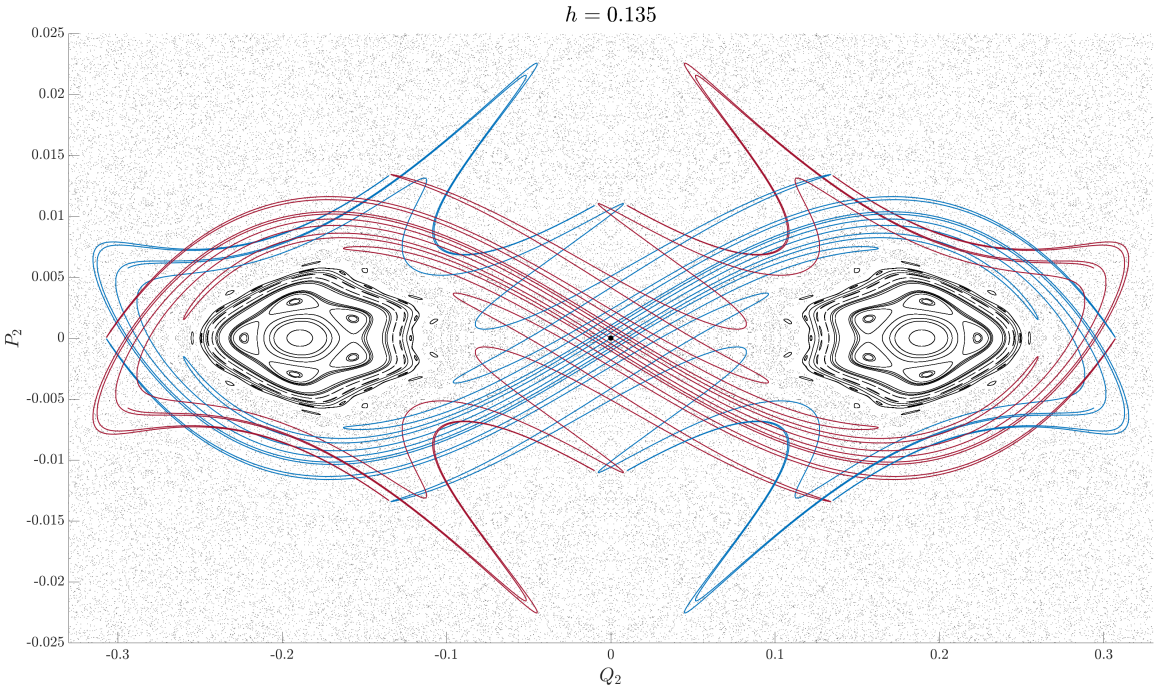

Figure 2.13 PSS near the Leapfrogging orbit in Aref-Eckhardt coordinates for $h = 0.135$. Observe that there are no remaining island chains outside the invariant manifolds. Stable and unstable manifolds of the hyperbolic or in blue and red, respectively

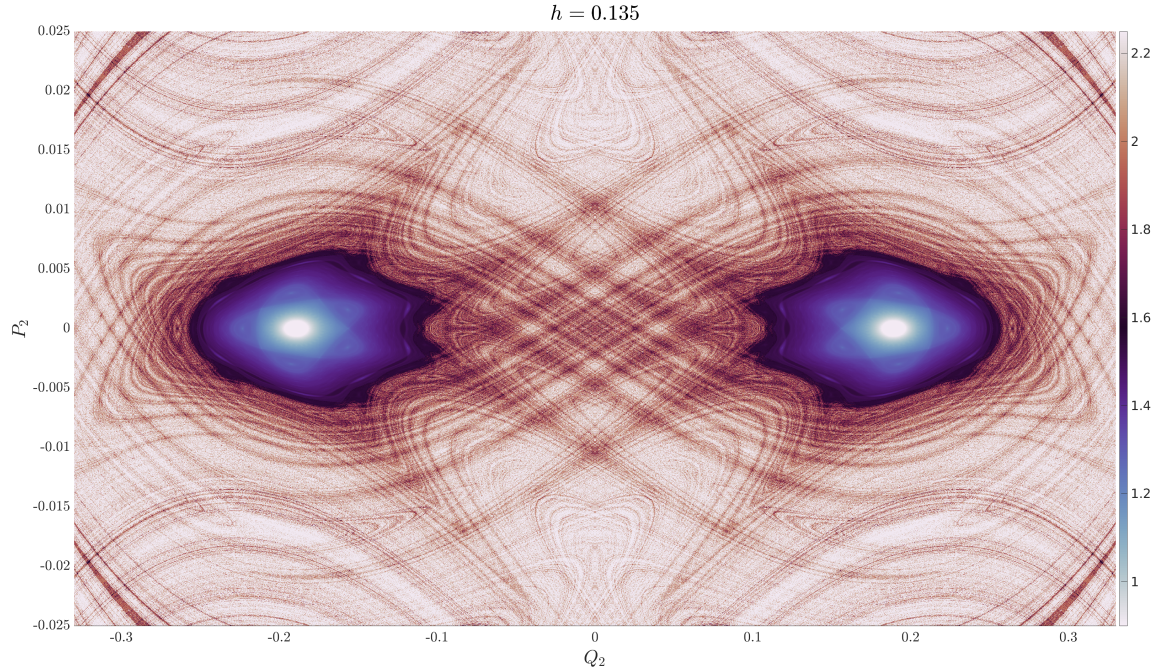

Figure 2.14 DLD near the Leapfrogging orbit in Aref-Eckhardt coordinates for $h = 0.135$.

CHAPTER 3

THE N-VORTEX PROBLEM

In this chapter, we begin in Section 3.1 by deriving the point-vortex solution to Euler's equations for an ideal fluid. This derivation leads us into Kirchhoff's Hamiltonian formulation of point-vortex motion in Section 3.2. To build intuition for subsequent calculations, in Section 3.3, we solve the two-vortex problem using methods that transfer to the novel reductions in Chapter 4.

3.1 Point-Vortex Model

3.1.1 Euler's Equation

Euler's equation for an inviscid, incompressible flow can be derived using the continuum assumption and the basic principles of physics—conservation of mass, conservation of energy and Newton's second law. Let $\mathbf{x} = (x, y, z) \in D \subset \mathbb{R}^3$ denote the position of a particle suspended in the fluid, let $\dot{\mathbf{x}} = \mathbf{u}(\mathbf{x}, t) = (u, v, w)$ be the velocity field of the fluid and let $\rho(\mathbf{x}, t)$ be the mass density. Euler's equations for an inviscid, incompressible flow with no external forces are

$$\begin{aligned} \rho \frac{D\mathbf{u}}{Dt} &= -\nabla \mathbf{p}, \\ \frac{D\rho}{Dt} &= 0, \\ \nabla \cdot \mathbf{u} &= 0. \end{aligned}$$

These correspond to Newton's third law, conservation of mass and incompressibility.

3.1.2 Vorticity Form of the Equations

We assume a constant density and scale the variables such that $\rho = 1$. A velocity field $\mathbf{u} = (u, v, w) \in \mathbb{R}^3$ has a corresponding vorticity field $\boldsymbol{\omega} = \nabla \times \mathbf{u}$. A velocity

field $\mathbf{u}$ is said to be irrotational if $\boldsymbol{\omega} = 0$. Taking the curl and divergence of $\boldsymbol{\omega}$,

$$\begin{aligned}
\nabla \cdot \boldsymbol{\omega} &= \nabla \cdot (\nabla \times \mathbf{u}) = 0 \\
\nabla \times \boldsymbol{\omega} &= \nabla \times (\nabla \times \mathbf{u}) \\
&= \nabla(\nabla \cdot \mathbf{u}) - \nabla^2 \mathbf{u} = -\nabla^2 \mathbf{u}.
\end{aligned}$$

That is

$$\begin{aligned}
\nabla \cdot \boldsymbol{\omega} &= 0 \\
\nabla \times \boldsymbol{\omega} &= -\nabla^2 \mathbf{u}.
\end{aligned}$$

An irrotational incompressible flow is a potential flow, i.e., there exists a potential ϕ such that $\mathbf{u} = \nabla\phi$. If the flow has a rotational component, then utilizing the Helmholtz-Hodge decomposition, $\mathbf{u}$ can be written as a sum of a velocity potential and a solenoidal vector potential

$$\mathbf{u} \equiv \mathbf{u}_\phi + \mathbf{u}_\omega = \nabla\phi + \nabla \times \boldsymbol{\psi}.$$

It then follows that

$$\begin{aligned}
\nabla \times \mathbf{u} =& \nabla \times (\nabla\phi + \nabla \times \nabla\boldsymbol{\psi}) \\
=& \nabla \times \nabla\boldsymbol{\psi} \\
=& \nabla(\nabla \cdot \mathbf{u}) - \nabla^2 \boldsymbol{\psi} = -\nabla^2 \boldsymbol{\psi},
\end{aligned}$$

which is just the Poisson equation

$$\nabla^2 \boldsymbol{\psi} = -\boldsymbol{\omega}. \tag{3.1}$$

In two dimensions, the Poisson kernel in the plane,

$$G(\mathbf{x}) = -\frac{1}{2\pi} \log \|\mathbf{x}\|,$$

can be used to find $\boldsymbol{\psi}$,

$$\boldsymbol{\psi}(\mathbf{x}) = \int G(\mathbf{x}-\mathbf{y})\boldsymbol{\omega}(\mathbf{y})\, d\mathbf{y}.$$

For two dimensional flow $\mathbf{u} = (u, v, 0)$, the vorticity has only one component $\boldsymbol{\omega} = (0, 0, \omega)$ which is given by

$$\omega(x, y, t) = (\nabla \times \mathbf{u})_z = \partial_x v - \partial_y u.$$

We can then solve the Poisson equation (3.1) to find $\boldsymbol{\psi} = (0, 0, \psi)$ and get the equations of motion for a particle in the flow field

$$\dot{\mathbf{x}} = \mathbf{u} = \nabla \times \psi = (\partial_y \psi, -\partial_x \psi, 0).$$

3.1.3 Discrete Vortex Representations

Restricting to motion on a plane, we can solve (3.1.2) in the case of discrete point vortex motion

$$\omega(\mathbf{x}) = \sum_{i=0}^{N} \Gamma_i\, \delta(\mathbf{x} - \mathbf{x_i})$$

The resulting flow is irrotational except at the location of the point vortices at $\mathbf{x}_i$ which have *vorticity* (or *circulation*) Γ_i. This is analogous to the point-mass approximation for the gravitational N-body problem. However, importantly, Γ_i can either be positive or negative (corresponding to counter-clockwise and clockwise flows), while Newtonian mass is strictly positive. Taking N vortices located at $\mathbf{x}_\alpha = (x_\alpha(t), y_\alpha(t))$ with vorticity Γ_α, then the Green's function for ψ gives

$$\begin{aligned}\psi_\alpha(\mathbf{x}) &= -\frac{1}{2\pi} \int \Gamma_\alpha \log \|\mathbf{x}-\mathbf{y}\|\, \delta(\mathbf{x}_\alpha - \mathbf{y})\, d\mathbf{y} \\ &= -\frac{\Gamma_\alpha}{2\pi} \log \|\mathbf{x} - \mathbf{x}_\alpha\|\,.\end{aligned}$$

Since the velocity field is obtained by linear superposition, the motion of a particle at $\mathbf{x}$ is

$$\dot{\mathbf{x}} = \sum_{\alpha=1}^{N} \nabla \times \boldsymbol{\psi}_\alpha(\mathbf{x}, t),$$

and since each point vortex moves with the local velocity field, the equations of motion for a collection of N-vortices are

$$\dot{\mathbf{x}}_\beta = \sum_{\alpha\neq\beta}^{N} \nabla \times \boldsymbol{\psi}_\alpha(\mathbf{x}_\beta, t).$$

The equations of motion can be written in component form using $\nabla \times \boldsymbol{\psi} = (\partial_y\psi, -\partial_x\psi)$ as

$$\dot{x}_\alpha = -\frac{1}{2\pi} \sum_{\alpha\neq\beta}^{N} \Gamma_\beta \frac{(y_\alpha - y_\beta)}{\|\mathbf{x}_\beta - \mathbf{x}_\alpha\|^2}, \tag{3.2a}$$

$$\dot{y}_\alpha = +\frac{1}{2\pi} \sum_{\alpha\neq\beta}^{N} \Gamma_\beta \frac{(x_\alpha - x_\beta)}{\|\mathbf{x}_\beta - \mathbf{x}_\alpha\|^2}. \tag{3.2b}$$

3.2 The Hamiltonian N-Vortex Problem

In this section, we review the Hamiltonian framework for the N-vortex problem. Consider a system consisting of N point vortices in the plane, each with position coordinates $\mathbf{r}_i = (x_i, y_i)$ and denote their (signed) vorticities by Γ_i. The system of ODEs describing the N-vortex motion can be described by the Hamiltonian [44],[1]

$$H(\mathbf{r}_i) = -\sum_{i<j}^{N} \Gamma_i\Gamma_j \log \|\mathbf{r}_i - \mathbf{r}_j\|^2 \tag{3.3}$$

with the non-canonical equations of motion

$$\Gamma_j \frac{dx_j}{dt} = +\frac{\partial H}{\partial y_j} \quad \text{and} \quad \Gamma_j \frac{dy_j}{dt} = -\frac{\partial H}{\partial x_j} \tag{3.4}$$

[1]The Hamiltonian given here, and throughout this paper, is 4π times the Hamiltonian derived by Kirchhoff. We have systematically ignored this factor throughout the paper, which amounts to a rescaling of time.

and where the Poisson brackets are defined by

$$\{f,g\} = \sum_{i=1}^{N} \frac{1}{\Gamma_i}\left(\frac{\partial f}{\partial x_i}\frac{\partial g}{\partial y_i} - \frac{\partial f}{\partial y_i}\frac{\partial g}{\partial x_i}\right) \text{ so that } \{x_i, y_j\} = \frac{1}{\Gamma_i}\delta_{ij}.$$

Because the Hamiltonian (3.3) is invariant with respect to rotations and translations in the plane, we have three integrals of motion

$$Q = \sum_{i=1}^{n} \Gamma_i x_i, \quad P = \sum_{i=1}^{n} \Gamma_i y_i \quad \text{and} \quad I = \sum_{i=1}^{n} \Gamma_i (x_i^2 + y_i^2), \tag{3.5}$$

where Q and P are the components of the linear impulse in the x and y-directions and I is the angular impulse. In general, these quantities are **not** in involution

$$\{Q,P\} = \sum_{i=1}^{N} \Gamma_i, \quad \{P,I\} = -2Q \quad \text{and} \quad \{Q,I\} = 2P. \tag{3.6}$$

However, this dissertation considers the special case in which the net circulation vanishes, $\Gamma = \sum_i^N \Gamma_i = 0$. Therefore, $\{Q,P\} = 0$, i.e. Q and P are independent conserved quantities. It is convenient to introduce coordinates

$$q_j = \sqrt{|\Gamma_j|}x_j \quad \text{and} \quad p_j = \sqrt{|\Gamma_j|}\text{sgn}(\Gamma_j)y_j, \tag{3.7}$$

such that the Poisson bracket defined by

$$\{f,g\} = \sum_{i=1}^{N} \left(\frac{\partial f}{\partial q_i}\frac{\partial g}{\partial p_i} - \frac{\partial f}{\partial q_i}\frac{\partial g}{\partial p_i}\right).$$

are canonical, $\{q_i, p_j\} = \delta_{ij}$ and q_i and p_i evolve with equations of motion

$$\frac{dq_j}{dt} = +\frac{\partial H}{\partial p_j} \quad \text{and} \quad \frac{dq_j}{dt} = -\frac{\partial H}{\partial q_j}. \tag{3.8}$$

3.3 Two-Vortex Motion

We first consider the motion of two vortices to illustrate the principles in the last section. In this section, we demonstrate that two vortices of equal and opposite-signed vorticity move in parallel at a uniform speed with their common velocity inversely

proportional to the distance between them. Two vortices of equal and like-signed vorticity, by contrast, trace a circular path with a constant rotation rate proportional to the inverse square of the distance between them. This result summarized in Figure 3.1.

The solution to this system is a standard result; however, we will solve it using canonical transformation to build intuition for understanding the reduction of the three and four vortex configurations considered in Section 4.2 and Section 4.3.

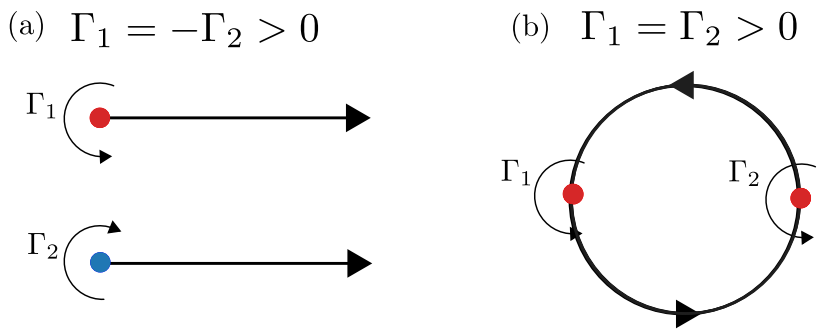

Figure 3.1 (a) Opposite-signed vortices move in parallel along straight lines. (b) Like-signed vortices move along a circular path.

Considering a vortex with circulation Γ_1 at $\mathbf{r}_1 = (x_1, y_1)$ and a second vortex with circulation Γ_2 at $\mathbf{r}_2 = (x_2, y_2)$, the Hamiltonian is

$$H(\mathbf{r}_1, \mathbf{r}_2) = -\Gamma_1 \Gamma_2 \log \|\mathbf{r}_1 - \mathbf{r}_2\|^2 , \tag{3.9}$$

The behavior depends on whether the net circulation is zero, so each case will be considered separately.

1. **The case $\Gamma_1 + \Gamma_2 \neq 0$:** We make the canonical transformation into center-of-vorticity and difference coordinates

$$\mathbf{R} = \frac{\Gamma_1 \mathbf{r}_1 + \Gamma_2 \mathbf{r}_2}{\Gamma_1 + \Gamma_2} \text{ and } \mathbf{r} = \mathbf{r}_1 - \mathbf{r}_2. \tag{3.10}$$

where $\mathbf{R} = (X, Y)$ and $\mathbf{r} = (x, y)$ and can be inverted as

$$\mathbf{r}_1 = \mathbf{R} + \frac{\Gamma_2}{\Gamma_1 + \Gamma_2}\mathbf{r} \tag{3.11}$$

$$\mathbf{r}_2 = \mathbf{R} - \frac{\Gamma_1}{\Gamma_1 + \Gamma_2}\mathbf{r}. \tag{3.12}$$

The Poisson brackets in the center-of-vorticity coordinates are

$$\{x, y\}_{\mathbf{r},\mathbf{R}} = \frac{\Gamma_1 + \Gamma_2}{\Gamma_1\Gamma_2} := \frac{1}{\Gamma_r} \quad \text{and} \quad \{X, Y\}_{\mathbf{r},\mathbf{R}} = \frac{1}{\Gamma_1 + \Gamma_2} := \frac{1}{\Gamma_R}.$$

The two-degree-of-freedom Hamiltonian (3.9) is now reduced to the one one-degree-of-freedom in $\mathbf{r}$, since $\mathbf{R}$ is a constant of motion

$$H(\mathbf{r}) = -\Gamma_1\Gamma_2 \log \|\mathbf{r}\|^2 = -\Gamma_r\Gamma_R \log\left(x^2 + y^2\right).$$

Using canonical polar variables (J, θ) defined by the relationships $x = \sqrt{2J}\cos\theta$ and $y = \sqrt{2J}\sin\theta$ where $\{\theta, J\} = \frac{1}{\Gamma_r}$, the Hamiltonian can be written as

$$H(\theta, J) = -\Gamma_r\Gamma_R \log(2J))$$

with equations of motion

$$\begin{aligned} \dot{J} &= -\frac{1}{\Gamma_r}\frac{\partial H}{\partial \theta} = \quad 0 \\ \dot{\theta} &= \quad \frac{1}{\Gamma_r}\frac{\partial H}{\partial J} = -\frac{\Gamma_R}{J}. \end{aligned}$$

Therefore, $J = \frac{x^2+y^2}{2}$ is a constant of motion and the frequency, $\omega = \frac{\Gamma_r}{J}$, is a constant. If we let the distance between r_1 and r_2 be $\|\mathbf{r}\| = D$, then $D^2 = 2J$ is a constant of motion. In terms of the original units, $\omega = 2\frac{\Gamma_1+\Gamma_2}{D^2}$. Since $\mathbf{r}$ moves in a circle with frequency ω and radius D, equation (3.11) implies that the vortices at $\mathbf{r}_1$ and $\mathbf{r}_2$ rotate on concentric circles about their center of vorticity

located at $\mathbf{R}$. If $\Gamma = \Gamma_1 = \Gamma_2$, then (3.11) states that

$$\begin{aligned} \mathbf{r}_1 - \mathbf{R} &= \frac{1}{2}\mathbf{r} \\ \mathbf{r}_2 - \mathbf{R} &= -\frac{1}{2}\mathbf{r}, \end{aligned}$$

and the vortices located at $\mathbf{r}_1$ and $\mathbf{r}_2$ rotate at constant speed at opposite ends of a diameter of a circle.

2. **The case $\Gamma_1 + \Gamma_2 = 0$:** Note that we cannot define the center of vorticity and difference coordinates when considering a pair of oppositely signed vortices since (3.10) is no longer defined. While the center-of-vorticity is not defined when the net circulation is zero, from, (3.6) the coordinates of the linear impulse $\mathbf{M} = (Q, P) = \sum \Gamma_i \mathbf{r}_i$ are independently conserved.

   Fixing the linear impulse to lie in the y direction $Q = 0$, $P = D$, and scaling the vorticity so that $\Gamma = \Gamma_1 = -\Gamma_2 = 1$, the linear impulse is $\mathbf{M} = \mathbf{r}_1 - \mathbf{r}_2 = (0, D)$. That is, $x_1 = x_2$ and $y_1 = y_2 + D$ so the difference between the x-components is zero and that between the the y-components is D. The equations of motion (3.4) yield $\dot{x}_1 = \dot{x}_2 = \frac{1}{D}$ and $\dot{y}_1 = \dot{y}_2 = 0$. That is, the vortices move in parallel along the x-axis with a constant speed of $\frac{1}{D}$.

CHAPTER 4

HAMILTONIAN REDUCTIONS OF SPECIAL CASES OF THE THREE AND FOUR-VORTEX PROBLEMS

4.1 Introduction

The driving inspiration for this chapter is the observation is that in both the walkabout and braiding motions of the unstable leapfrog motion seen in Figure 1.4, one of the pairs of like-signed orbits becomes tightly bound together and moves as a single unit (a *dimer*), at least for a finite time. This is illustrated in Figure 4.1. Therefore, the dynamics come close to that of a three-vortex system, with one vortex of strength two, and two vortices of the opposite sign with strength one.

In any dynamical study, it is crucial to pick the coordinate system that most illuminates the dynamics. The coordinate system used in previous studies was very useful in understanding the dynamics in a neighborhood of the leapfrogging orbit [10, 55, 61], but we have found it less useful when one pair of of the vortices forms a dimer. It makes sense to use a coordinate system in which one like-signed pair of vortices is coalesced into a dimer, while no such assumption is made about the other pair of vortices. Therefore, we construct a coordinate system in the present study

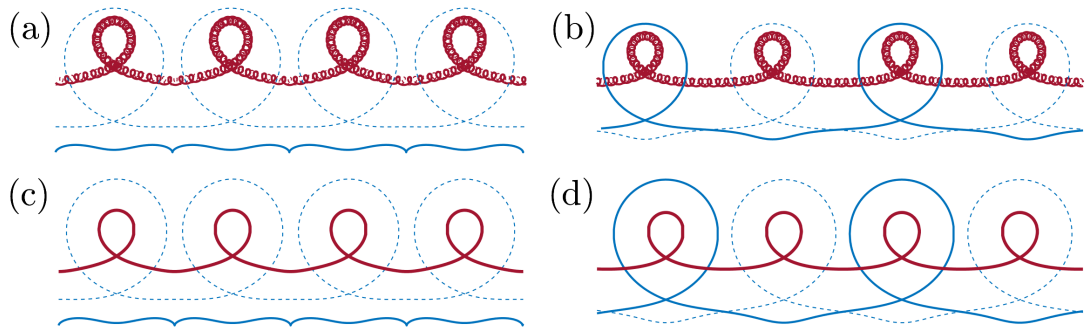

Figure 4.1 The braiding and walkabout motion for the vortex quartet along with the corresponding three-vortex system.

where the near-dimer dynamics are more easily visible. Such a system would resemble a three-vortex system with vorticities in the ratio -1:-1:2, coupled to an additional degree-of-freedom representing the dynamics within the dimer.

In Section 4.2, we study the three vortex problem with circulations -1:-1:2. The integrability of this system was demonstrated by Aref and Rott [6, 51]. We describe in detail the phase-space of this one-degree-of-freedom system. Understanding the dynamics of this system allows us to interpret the fundamental motions of the vortex quartet. We also present a new reduction using simple canonical transformations that forms part of the reduction of the vortex quartet.

We then proceed to Section 4.3 to discuss the four-vortex problem of two identical pairs of vortices, i.e., the vortex quartet. We write the Hamiltonian for the vortex quartet in a way that consists of the Hamiltonian of the three-vortex system coupled to an additional degree of freedom. This coordinate system, known as the 'dimer' system, is used in Chapters 6 and 7 when studying the nonlinear transitions of the vortex quartet.

Finally, in Section 4.4, we perform an additional canonical transformation that brings us to a new coordinate system for the vortex quartet, which is equivalent to the one found by Aref and Eckhardt [21] and well suited for the study of the stability of the leapfrogging orbit [10, 55, 61] and is used in Chapter 5.

4.2 The Three-Vortex Problem with Circulations -1:-1:2

Before analyzing the bound states of the vortex quartet, we first consider the three-vortex problem with vortices located at $\mathbf{r}_1$, $\mathbf{r}_2$ and $\mathbf{r}_3$ and vorticities $\Gamma_1 = \Gamma_2 = -1$ and $\Gamma_3 = 2$ respectively. The Hamiltonian for this three-vortex system is given by

$$H(\mathbf{r}_1, \mathbf{r}_2, \mathbf{r}_3) = -\log \|\mathbf{r}_1 - \mathbf{r}_2\|^2 + 2\log \|\mathbf{r}_1 - \mathbf{r}_3\|^2 + 2\log \|\mathbf{r}_2 - \mathbf{r}_3\|^2 . \tag{4.1}$$

The linear impulse $\mathbf{M} = (Q, P)$ given by (3.5) is a constant of motion. In general, Q and P are not independent constants of motion. However, since $\{Q, P\} = \sum_{i=1}^{3} \Gamma_i = 0$, Q and P are in involution and thus independent conserved quantities, and

$$\mathbf{M} = (Q, P) = \sum_{i=1}^{3} \Gamma_i \mathbf{r}_i = -\mathbf{r}_1 - \mathbf{r}_2 + 2\mathbf{r}_3$$

is a constant of motion.

We first switch into the center-of-vorticity coordinates of the two identical vortices, located at $\mathbf{r}_1$ and $\mathbf{r}_2$,

$$\mathbf{R} = \frac{\mathbf{r}_1 + \mathbf{r}_2}{2} \text{ and } \mathbf{r} = \mathbf{r}_1 - \mathbf{r}_2. \tag{4.2}$$

In these coordinates, the conserved impulse is

$$\mathbf{M} = (Q, P) = \sum_{i=1}^{3} \Gamma_i \mathbf{r}_i = 2(\mathbf{r}_3 - \mathbf{R}),$$

which gives a relation between $\mathbf{r}_3$ and $\mathbf{R}$, $\mathbf{r}_3 = \mathbf{R} + \frac{\mathbf{M}}{2}$. The Hamiltonian can now be reduced to a one-degree-of-freedom system

$$\begin{aligned} H(\mathbf{r}, \mathbf{R}) &= -\log \|\mathbf{r}_1 - \mathbf{r}_2\|^2 + 2\log \|\mathbf{r}_1 - \mathbf{r}_3\|^2 + 2\log \|\mathbf{r}_2 - \mathbf{r}_3\|^2 \\ &= -\log \|\mathbf{r}\|^2 + 2\log \left\|\mathbf{R} + \frac{\mathbf{r}}{2} - \mathbf{R} - \frac{\mathbf{M}}{2}\right\|^2 + 2\log \left\|\mathbf{R} - \frac{\mathbf{r}}{2} - \mathbf{R} - \frac{\mathbf{M}}{2}\right\|^2 \\ &= -\log \|\mathbf{r}\|^2 + 2\log \|\mathbf{r} - \mathbf{M}\|^2 + 2\log \|\mathbf{r} + \mathbf{M}\|^2 + C. \end{aligned} \tag{4.3}$$

This Hamiltonian can be understood as that of the advection of a tracer particle located at $\mathbf{r}$ moving in the flow due to three static vortices, with vorticity -2, 1 and -2 located at positions $\mathbf{M}$, $\mathbf{0}$ and $-\mathbf{M}$. For the general three-vortex system with net circulation zero, the same process can be followed considering (without loss of generality) $\Gamma_1 = -1 - \lambda$, $\Gamma_2 = -1 + \lambda$ and $\Gamma_3 = 2$ and the general center-of-vorticity and difference coordinates (3.11); however, we only make use of the

symmetric case and only present the $\lambda = 0$ case for clarity. Aref [8] also found this result; however, we believe the approach that is given here, which uses elementary canonical transformations, to be more transparent. Additionally, these canonical transformations are critical to transforming the Hamiltonian for the four-vortex system in Section 4.3.

Because both components of the linear impulse, $\mathbf{M}$, are independently conserved, we can choose the magnitude and direction $\mathbf{M}$. The Hamiltonian (4.3), with $\mathbf{M} = (0, -2)$, $\mathbf{r} = (\sqrt{2}q, \sqrt{2}p)$ and a time rescaling, $f(H) = Ce^{-H}$, yields a canonical Hamiltonian with,

$$H(q,p) = \frac{1}{2} \frac{q^2 + p^2}{\left(q^2 + (p - \sqrt{2})^2\right)^2 \left(q^2 + (p + \sqrt{2})^2\right)^2}. \tag{4.4}$$

where $\{q, p\} = 1$.

The Hamiltonian (4.4) has five fixed points, $(0,0)$, $(0, \pm\sqrt{2})$, $(\pm\frac{\sqrt{6}}{3}, 0)$. The corresponding Hessians show that these are three centers and two saddles, respectively. The three center-type fixed points represent degenerate states. The phase plane has three distinct regions and separatrices at the critical energy $H_{\text{separatrix}} = \frac{3^3}{2^{12}}$ The behavior of the solutions in each of the three regions are shown in Figure 4.2 along with the representations of the corresponding vortex trajectories. All periodic orbits in Regions I, II, and III correspond to (relative) periodic motions of the three-vortex motion in the lab frame.

Region I is foliated by periodic motions about the origin, which correspond to hierarchical orbits in which the two vortices of circulation -1 are bound together and move as a pair in parallel to the vortex of circulation +2. We have borrowed the term *hierarchical* from the gravitational three-body problem. The origin itself represents a degenerate state. As the family of periodic orbits shrinks to the fixed point at the origin, the distance between the two negative vortices of unit circulation approaches zero while the distance between this pair and the positive vortex at $\mathbf{r}_3$

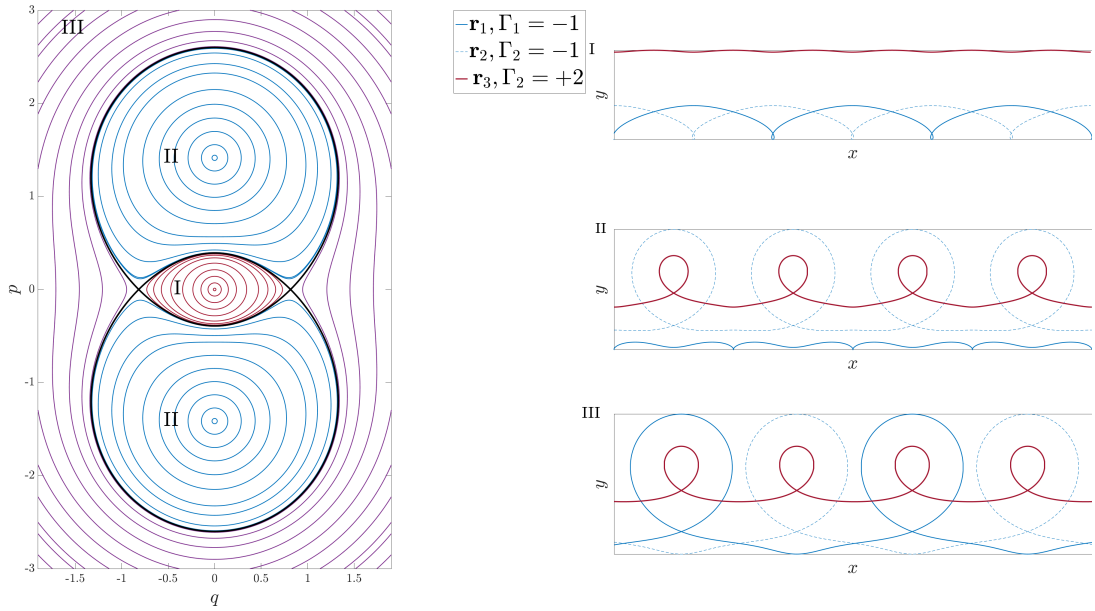

Figure 4.2 The phase plane for the reduced -1:-1:2 three-vortex system (left) along with typical trajectories in each region (right).

remains finite. In this limit, the pair of negative signed vortices behaves like a single vortex of circulation -2, and the overall motion is the straight parallel translation of two vortices of circulation ± 2.

Each connected component of Region II is also foliated by periodic motions about the fixed points at $(0, \pm\sqrt{2})$. In these hierarchical orbits, the vortex of circulation $+2$ and one of the vortices with circulation -1 are bound together, and this pair moves in parallel with the remaining vortex of circulation -1. Note the similarity between this orbit and the walkabout orbit of the vortex quartet described by Acheson. As the two families of periodic orbits shrink to the fixed points at $(0, \pm\sqrt{2})$, the distance between the vortex of circulation $+2$ and one of the vortices with circulation -1 become small, and they act like a vortex of circulation $+1$. The overall motion is then the straight parallel translation of two vortices of circulation ± 1.

The periodic orbits in Region III correspond to non-hierarchical vortex motions. These periodic motions are analogous to the braiding motions seen in the vortex

quartet. Since the vortices of circulation -1 alternate, there is no hierarchy of these orbits that can be shrunk to a degenerate state.

The saddle type fixed points at $(\pm\frac{\sqrt{6}}{3}, 0)$ represent orbits in which the three vortices form an equilateral triangle that rigidly translates at a constant velocity parallel to the line segment connecting the two negative vortices; see Fig 4.3. These *rigidly translating triangles* (RTT), are fundamental to understand the nonlinear transitions in Chapter 7. We refer to the separatrices between Regions I and Regions II as the *interior* separatrices and the separatices between Regions II and III as the *exterior* separatrices. As is so often the case, we will show that understanding these saddle points, their separatrices, and especially the splitting of the separatrices is fundamental to explaining the dynamics.

4.3 The Dimer Coordinates for the Vortex Quartet

We established all the basic motions of the integrable three-vortex system with circulations -1:-1:2 in Section 4.2 and progress to the four-vortex system consisting of two pairs of vortices with circulations +1:+1:-1:-1. The goal of this section is to write the four-vortex Hamiltonian in a way such that it consists of the Hamiltonian of the three-vortex system in Section 4.2 coupled to an additional degree-of-freedom. If the coupling term is small, then this can be thought of as a small perturbation. We implement a factorization used by Smith [53] to write the Hamiltonian in a form where two negative vortices are bound close together into a 'dimer' that interacts with the remaining two vortices. We consider a system of four vortices composed of

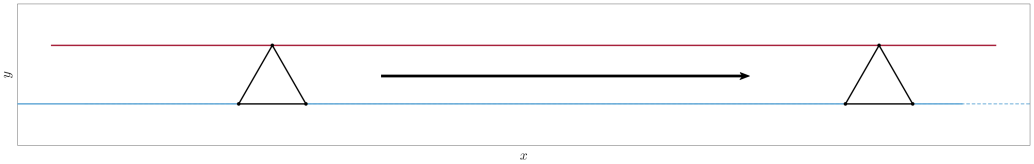

Figure 4.3 The rigidly translating triangles (RTT) at the saddle type fixed point at $(\frac{\sqrt{6}}{3}, 0)$ in Figure 4.2.

two vortices of vorticity $\Gamma = +1$, with coordinates $\mathbf{r}_1^+ = (x_1^+, y_1^+)$ and $\mathbf{r}_2^+ = (x_2^+, y_2^+)$, and two with vorticity $\Gamma = -1$, with coordinates $\mathbf{r}_1^- = (x_1^-, y_1^-)$ and $\mathbf{r}_2^- = (x_2^-, y_2^-)$. The Hamiltonian then takes the form

$$\begin{aligned} H(\mathbf{r}_1^-, \mathbf{r}_1^-, \mathbf{r}_2^-, \mathbf{r}_2^+) = &- \log \left\|\mathbf{r}_2^+ - \mathbf{r}_1^+\right\|^2 - \log \left\|\mathbf{r}_1^- - \mathbf{r}_2^-\right\|^2 + \log \left\|\mathbf{r}_1^- - \mathbf{r}_1^+\right\|^2 \\ &+ \log \left\|\mathbf{r}_2^- - \mathbf{r}_1^+\right\|^2 + \log \left\|\mathbf{r}_1^- - \mathbf{r}_2^+\right\|^2 + \log \left\|\mathbf{r}_2^- - \mathbf{r}_2^+\right\|^2 . \end{aligned} \tag{4.5}$$

The first step is to perform a canonical transformation that treats the two positive vortices as a dimer. Let $\mathbf{R}_+$ be the center of vorticity of the vortices at $\mathbf{r}_1^+$ and $\mathbf{r}_2^+$ and let $\mathbf{r}_+$ be the vector difference between them,

$$\mathbf{R}_+ = \frac{\mathbf{r}_1^+ + \mathbf{r}_2^+}{2} \quad \text{and} \quad \mathbf{r}_+ = \mathbf{r}_1^+ - \mathbf{r}_2^+. \tag{4.6}$$

Putting (4.6) into the Hamiltonian (4.5),

$$\begin{aligned} H\left(\mathbf{r}_1^-, \mathbf{r}_2^-, \mathbf{r}_+, \mathbf{R}_+\right) = &- \log \|\mathbf{r}_+\|^2 - \log \left\|\mathbf{r}_1^- - \mathbf{r}_2^-\right\|^2 \\ &+ \log \left\|\mathbf{r}_1^- - \mathbf{R}_+ - \frac{1}{2}\mathbf{r}_+\right\|^2 + \log \left\|\mathbf{r}_2^- - \mathbf{R}_+ - \frac{1}{2}\mathbf{r}_+\right\|^2 \\ &+ \log \left\|\mathbf{r}_1^- - \mathbf{R}_+ + \frac{1}{2}\mathbf{r}_+\right\|^2 + \log \left\|\mathbf{r}_2^- - \mathbf{R}_+ + \frac{1}{2}\mathbf{r}_+\right\|^2 . \end{aligned} \tag{4.7}$$

Our goal is to understand the dynamics when the diameter of the positive dimer, $\|\mathbf{r}_+\|$, is small. In the third term of H, we can factor out the distance between the vortex located at $\mathbf{r}_1^-$ and center of the dimer, $\mathbf{R}_+$,

$$\begin{aligned} \left\|\mathbf{r}_1^- - \mathbf{R}_+ - \frac{1}{2}\mathbf{r}_+\right\|^2 &= \left\langle \left(\mathbf{r}_1^- - \mathbf{R}_+\right) - \frac{1}{2}\mathbf{r}_+, \left(\mathbf{r}_1^- - \mathbf{R}_+\right) - \frac{1}{2}\mathbf{r}_+ \right\rangle \\ &= \left\|\mathbf{r}_1^- - \mathbf{R}_+\right\|^2 - \left\langle \mathbf{r}_1^- - \mathbf{R}_+, \mathbf{r}_+ \right\rangle + \frac{1}{4}\|\mathbf{r}_+\|^2 \\ &= \left\|\mathbf{r}_1^- - \mathbf{R}_+\right\|^2 \left| 1 - \frac{\left\langle \mathbf{r}_1^- - \mathbf{R}_+, \mathbf{r}_+ \right\rangle}{\left\|\mathbf{r}_1^- - \mathbf{R}_+\right\|^2} + \frac{1}{4}\frac{\|\mathbf{r}_+\|^2}{\left\|\mathbf{r}_1^- - \mathbf{R}_+\right\|^2} \right| . \end{aligned} \tag{4.8}$$

An analogous calculation applies for the remaining three terms of (4.7). Using the fundamental relation between the logarithm of a product and the sum of the

logarithms allows (4.5) to be written as $H = H_0 + H_1$ where

$$\begin{aligned} H_0(\mathbf{r}_1^-, \mathbf{r}_2^-, \mathbf{r}_+, \mathbf{R}_+) = &\quad H_{01}(\mathbf{r}_+) + H_{02}(\mathbf{r}_1^-, \mathbf{r}_2^-, \mathbf{R}_+) \\ = &- \log \|\mathbf{r}_+\|^2 \\ &- \log \left\|\mathbf{r}_1^- - \mathbf{r}_2^-\right\|^2 + 2\log \left\|\mathbf{r}_1^- - \mathbf{R}_+\right\|^2 + 2\log \left\|\mathbf{r}_2^- - \mathbf{R}_+\right\|^2 \end{aligned}$$

and

$$\begin{aligned} H_1 = &\quad \log \left| 1 - \frac{\langle \mathbf{r}_1^- - \mathbf{R}_+, \mathbf{r}_+ \rangle}{\left\|\mathbf{r}_1^- - \mathbf{R}_+\right\|^2} + \frac{1}{4} \frac{\|\mathbf{r}_+\|^2}{\left\|\mathbf{r}_1^- - \mathbf{R}_+\right\|^2} \right| \\ &+ \log \left| 1 + \frac{\langle \mathbf{r}_1^- - \mathbf{R}_+, \mathbf{r}_+ \rangle}{\left\|\mathbf{r}_1^- - \mathbf{R}_+\right\|^2} + \frac{1}{4} \frac{\|\mathbf{r}_+\|^2}{\left\|\mathbf{r}_1^- - \mathbf{R}_+\right\|^2} \right| \\ &+ \log \left| 1 - \frac{\langle \mathbf{r}_2^- - \mathbf{R}_+, \mathbf{r}_+ \rangle}{\left\|\mathbf{r}_2^- - \mathbf{R}_+\right\|^2} + \frac{1}{4} \frac{\|\mathbf{r}_+\|^2}{\left\|\mathbf{r}_2^- - \mathbf{R}_+\right\|^2} \right| \\ &+ \log \left| 1 + \frac{\langle \mathbf{r}_2^- - \mathbf{R}_+, \mathbf{r}_+ \rangle}{\left\|\mathbf{r}_2^- - \mathbf{R}_+\right\|^2} + \frac{1}{4} \frac{\|\mathbf{r}_+\|^2}{\left\|\mathbf{r}_2^- - \mathbf{R}_+\right\|^2} \right|. \end{aligned}$$

The term H_{01} represents the internal motion of the dimer, which is decoupled from H_{02}, which describes the motion of vortices at $\mathbf{r}_1^-, \mathbf{r}_2^-$ and $\mathbf{R}_+$ with vorticities -1:-1:2 respectively. The sum of three terms that form H_{02} is identical to the Hamiltonian (4.1) for the -1:-1: 2 system. Therefore, we can use the same systematic canonical transformations (4.2) on H_{02} to reduce the dimer system from a four to a two-degree-of-freedom system. To do so, let

$$\mathbf{R}_- = \frac{\mathbf{r}_1^- + \mathbf{r}_2^-}{2} \quad \text{and} \quad \mathbf{r}_- = \mathbf{r}_1^- - \mathbf{r}_2^-. \tag{4.9}$$

The linear impulse $\mathbf{M}$, is a constant of motion, equal to

$$\mathbf{M} = (Q, P) = \sum_{i=1}^{4} \Gamma_i \mathbf{r}_i = 2\left(\mathbf{R}_+ - \mathbf{R}_-\right), \tag{4.10}$$

thus $\mathbf{R}_+ = \mathbf{R}_- + \frac{\mathbf{M}}{2}$ and (4.9) can be rewritten as $\mathbf{r}_1^- = \mathbf{R}_- + \frac{\mathbf{r}_-}{2}$, allowing the summands defining H_{02} to be rewritten as

$$\mathbf{r}_1^- - \mathbf{R}_+ = \mathbf{R}_- + \frac{\mathbf{r}_-}{2} - \left(\mathbf{R}_- + \frac{\mathbf{M}}{2}\right) = \frac{1}{2}\left(\mathbf{r}_- - \mathbf{M}\right), \tag{4.11}$$

and similarly

$$\mathbf{r}_2^- - \mathbf{R}_+ = -\frac{1}{2}\left(\mathbf{r}_- + \mathbf{M}\right). \tag{4.12}$$

Then the coupling term H_1 can be written in terms of $(\mathbf{r}_+, \mathbf{r}_-)$ and the conserved quantity $\mathbf{M}$,

$$\begin{aligned} H_1(\mathbf{r}_+, \mathbf{r}_-) = \quad & \log\left|1 - 2\frac{\langle \mathbf{r}_+ - \mathbf{M}, \mathbf{r}_-\rangle}{\|\mathbf{r}_+ - \mathbf{M}\|^2} + \frac{\|\mathbf{r}_-\|^2}{\|\mathbf{r}_+ - \mathbf{M}\|^2}\right| \\ & + \log\left|1 + 2\frac{\langle \mathbf{r}_+ - \mathbf{M}, \mathbf{r}_-\rangle}{\|\mathbf{r}_+ - \mathbf{M}\|^2} + \frac{\|\mathbf{r}_-\|^2}{\|\mathbf{r}_+ - \mathbf{M}\|^2}\right| \\ & + \log\left|1 - 2\frac{\langle \mathbf{r}_+ + \mathbf{M}, \mathbf{r}_-\rangle}{\|\mathbf{r}_+ + \mathbf{M}\|^2} + \frac{\|\mathbf{r}_-\|^2}{\|\mathbf{r}_+ + \mathbf{M}\|^2}\right| \\ & + \log\left|1 + 2\frac{\langle \mathbf{r}_+ + \mathbf{M}, \mathbf{r}_-\rangle}{\|\mathbf{r}_+ + \mathbf{M}\|^2} + \frac{\|\mathbf{r}_-\|^2}{\|\mathbf{r}_+ + \mathbf{M}\|^2}\right|. \end{aligned}$$

Putting this all together, we can now write

$$H(\mathbf{r}_-, \mathbf{r}_+) = H_{01}(\mathbf{r}_-) + H_{02}(\mathbf{r}_+) + H_1(\mathbf{r}_-, \mathbf{r}_+), \tag{4.13}$$

where H_{01} is the motion of the dimer

$$H_{01}(\mathbf{r}_-) = -\log\|\mathbf{r}_-\|^2$$

and H_{02} can be reduced to the form given by (4.3),

$$H_{02}(\mathbf{r}_+) = -\log\|\mathbf{r}_+\|^2 + 2\log\|\mathbf{r}_+ + \mathbf{M}\|^2 + 2\log\|\mathbf{r}_+ + \mathbf{M}\|^2.$$

Moreover, H_1 determines the coupling between the $\mathbf{r}_+$ and $\mathbf{r}_-$ degrees of freedom. This term is small while $\|\mathbf{r}_+\|$, the distance between the two positive vortices, is small. However, as we see with the walkabout orbits, the vortex quartet can switch back and forth from regions where $\|\mathbf{r}_+\|$ is small and regions where $\|\mathbf{r}_-\|$ is small. This transition happens as the system switches from the positive-signed pairs being close together and the negative-signed pairs being close together.

We now choose to normalize the coordinates. The Hamiltonian (4.16) can be be written in a standard canonical form by utilizing (3.7),

$$(q_1, p_1) = \frac{1}{\sqrt{2}}\mathbf{r}_+ \quad \text{and} \quad (q_2, -p_2) = \frac{1}{\sqrt{2}}\mathbf{r}_- \tag{4.14}$$

or in the lab coordinates

$$\begin{aligned} q_1 &= \frac{1}{\sqrt{2}}\left(x_1^+ - x_2^+\right), \quad q_2 = \frac{1}{\sqrt{2}}\left(x_2^- - x_2^-\right), \\ p_1 &= \frac{1}{\sqrt{2}}\left(y_1^+ - y_2^+\right), \quad p_2 = \frac{1}{\sqrt{2}}\left(y_2^- - y_1^-\right). \end{aligned} \tag{4.15}$$

With this choice, the Poisson brackets are now normalized, i.e. $\{q_i, p_j\} = \delta_{ij}$ and the he new canonical pairs with given by the coordinates of $\mathbf{z}_1 = (q_1, p_1)$ and $\mathbf{z}_2 = (q_2, p_2)$.

4.4 Connection to the Aref-Eckhardt Coordinates

We derived the coordinate system and Hamiltonian appropriate for studying the nonlinear transitions discussed in Chapter 7. In this section, we discuss another coordinate system well-suited for studying the stability of the leapfrogging orbit, which was used in prior studies [10, 55, 61]. Aref and Eckhardt [21] also derived an equivalent Hamiltonian for an arbitrary collection of non-identical pairs of point vortices.

We note that we could have used the canonical transformations (4.2) and (4.6) and the conserved linear impulse (4.10) without employing the factorization (4.8). Directly applying these canonical transformation yields

$$\begin{aligned} H(\mathbf{r}_+, \mathbf{r}_-) = &- \log|\mathbf{r}_+|^2 - \log|\mathbf{r}_-|^2 \\ &+ \log\|\mathbf{M} - (\mathbf{r}_+ + \mathbf{r}_-)\|^2 + \log\|\mathbf{M} - (\mathbf{r}_+ - \mathbf{r}_-)\|^2 \\ &+ \log\|\mathbf{M} + (\mathbf{r}_+ + \mathbf{r}_-)\|^2 + \log\|\mathbf{M} + (\mathbf{r}_+ - \mathbf{r}_-)\|^2. \end{aligned} \tag{4.16}$$

The benefit of the near-integrable form (4.13) is to see the relationship between the three-vortex problem in regions where a pair of like signed vortices are close together while (4.16) has no such physical interpretation while it is manifest in (4.13). However, both the Hamiltonians (4.13) and (4.16) are, of course, algebraically equivalent.

We remarked in Section 2.3.3 that coordinates such the periodic orbit is perpendicular to the Poincaré section of surface, the analysis will be greatly simplified. Performing an additional canonical transformation

$$\begin{aligned} Q_1 &= \frac{1}{\sqrt{2}}\left(q_1 + q_2\right), \quad Q_2 = \frac{1}{\sqrt{2}}\left(q_1 - q_2\right), \\ P_1 &= \frac{1}{\sqrt{2}}\left(p_1 + p_2\right), \quad P_2 = \frac{1}{\sqrt{2}}\left(p_1 - p_2\right) \end{aligned} \tag{4.17}$$

and converting to lab coordinates yields

$$\begin{aligned} Q_1 &= \frac{1}{2}\left(x_1^+ - x_2^+ + x_2^- - x_2^-\right), \quad Q_2 = \frac{1}{2}\left(x_1^+ - x_2^+ - x_2^- + x_2^-\right), \\ P_1 &= \frac{1}{2}\left(y_1^+ - y_2^+ - y_1^- + y_2^-\right), \quad P_2 = \frac{1}{2}\left(y_1^+ - y_2^+ + y_1^- - y_2^-\right). \end{aligned}$$

To satisfy the initial conditions of the leapfrogging orbit in Figure 4.4, we seek a configuration symmetric with respect to reflection along the x-axis, i.e.

$$\begin{aligned} x_1^- &= x_2^-, \qquad x_1^+ = x_2^+, \\ y_1^- &= -y_2^-, \quad y_1^+ = -y_2^+. \end{aligned} \tag{4.18}$$

We see that for the leapfrogging orbits, which satisfy (4.18), then the subspace $Q_2 = P_2 = 0$ is invariant under the dynamics. Choosing the initial impulse to be $\mathbf{M} = (0, 2)$, in order to agree with the conventions chosen in the previous studies, the Hamiltonian

of the vortex quartet becomes

$$\begin{aligned} H_{\mathrm{Ar}}(Q_1, Q_2, P_1, P_2) = \quad & \log\left((Q_1+Q_2)^2 + (P_1+P_2)^2\right) \\ & + \log\left((Q_1-Q_2)^2 + (P_1-P_2)^2\right) \\ & - \log\left(Q_1^2 + (P_2-1)^2\right) - \log\left(Q_1^2 + (P_2+1)^2\right) \\ & - \log\left(Q_2^2 + (P_1-1)^2\right) - \log\left(Q_2^2 + (P_1+1)^2\right). \end{aligned}$$

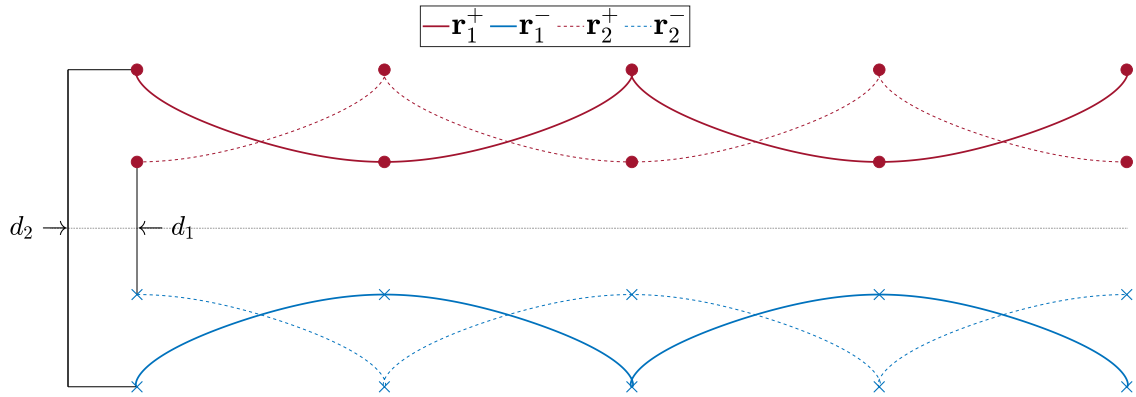

Figure 4.4 The curves show trajectories from a numerically-generated leapfrogging solution, with initial particle positions and separations labeled. Motion is from left to right with particle positions marked every half-period.

Letting $Q_1 = X$, $P_1 = Y$, $Q_2 = 0$ and $P_2 = 0$ the coordinates (X, Y) evolve under the one degree-of-freedom Hamiltonian

$$\begin{aligned} H_{\mathrm{leapfrog}}(X, Y) =& 2\log\left(X^2+Y^2\right) - 2\log\left(1+X^2\right) \\ & - \log\left(1-Y^2\right) - \log\left(1+Y^2\right)^2 \\ =& \log\left(\frac{X^2+Y^2}{(1+X^2)(1-Y^2)}\right)^2 \\ =& 2\log\left|\frac{1}{1-Y^2} - \frac{1}{1+X^2}\right| + C. \end{aligned}$$

In Chapter 5 the solutions to this Hamiltonian are discussed in detail.

CHAPTER 5

STABILITY OF THE LEAPFROGGING ORBIT

5.1 Introduction

In this chapter, we discuss the bifurcation of the leapfrogging orbit using the Hamiltonian formulation of the equations derived in Section 4.4. In Section 5.2, we discuss the equations of motion for the leapfrogging solution introduced in Chapter 1 and summarize some of its properties. In Section 5.3, we write down the linearized perturbation equations about the leapfrog orbit and discuss the relevant Floquet theory needed to understand its stability. In Section 5.4, we provide a transformation of the linearized perturbation equations so that the coefficients are given in an explicit form. We then address **Goal I** and provide four approaches:

1. In Section 5.4.2, utilizing the explicit closed-form version of the Floquet, we confirm the rational value of the bifurcation value using high precision arithmetic to an order of 10^{-120}.

2. In Section 5.5, we transform the time-periodic linear system into one with constant coefficients by successive Lie transforms and averaging.

3. In Section 5.6, we use the method of harmonic balance to search for a value of our parameter in which there exists a periodic solution, indicating that the Floquet multipliers collide on the real axis.

4. In Section 5.7, we use the conjectured bifurcation value as an ansatz and explicitly find a periodic solution to the Floquet problem for that value, demonstrating the existence of a bifurcation of the leapfrogging orbit.

Approaches two and three provide systematic and semi-analytic approximations to the bifurcation value via different techniques. Using these results as an ansatz, approach four provides a *proof* that the bifurcation happens at the ostensibly fortuitous value.

5.2 The Leapfrogging Trajectory

Consider the vortex quartet, which is system of four vortices composed of two vortices of vorticity $\Gamma^+ = +1$, with coordinates $\mathbf{r}_1^+ = (x_1^+, y_1^+)$ and $\mathbf{r}_2^+ = (x_2^+, y_2^+)$, and two with vorticity $\Gamma^- = -1$, with coordinates $\mathbf{r}_1^- = (x_1^-, y_1^-)$ and $\mathbf{r}_2^- = (x_2^-, y_2^-)$. As seen in Section 4.4, the Aref-Eckhardt coordinates defined by

$$\begin{aligned} Q_1 &= \frac{1}{2}\left(x_1^+ - x_2^+ + x_2^- - x_2^-\right), \quad Q_2 = \frac{1}{2}\left(x_1^+ - x_2^+ - x_2^- + x_2^-\right), \\ P_1 &= \frac{1}{2}\left(y_1^+ - y_2^+ - y_1^- + y_2^-\right), \quad P_2 = \frac{1}{2}\left(y_1^+ - y_2^+ + y_1^- - y_2^-\right), \end{aligned} \tag{5.1}$$

and an initial impulse of $\mathbf{M} = (0, 2)$, the dynamics of the vortex quartet is described by the Hamiltonian

$$\begin{aligned} H_{\mathrm{Ar}}(Q_1, Q_2, P_1, P_2) = \; & \log\left((Q_1 + Q_2)^2 + (P_1 + P_2)^2\right) \\ & + \log\left((Q_1 - Q_2)^2 + (P_1 - P_2)^2\right) \\ & - \log\left(Q_1^2 + (P_2 - 1)^2\right) - \log\left(Q_1^2 + (P_2 + 1)^2\right) \\ & - \log\left(Q_2^2 + (P_1 - 1)^2\right) - \log\left(Q_2^2 + (P_1 + 1)^2\right). \end{aligned} \tag{5.2}$$

Looking for orbits that satisfy the proper symmetry conditions when reflected along the x-axis, (4.18), leads to the examination of the subspace $Q_2 = P_2 = 0$ for a family of periodic orbits. Letting $Q_1 = X$, $P_1 = Y$, $Q_2 = 0$ and $P_2 = 0$, the coordinates (X, Y) evolve under the one degree-of-freedom Hamiltonian system with Hamiltonian

$$H(X, Y) = 2\log\left(\frac{1}{1 - Y^2} - \frac{1}{1 + X^2}\right). \tag{5.3}$$

To simplify the mathematical analysis and allow the use of standard perturbation techniques, we make the following elementary observation. In Section 2.2, we demonstrate that for a Hamiltonian system with Hamiltonian $H(q, p)$, the modified system with Hamiltonian $\tilde{H}(q, p) = f \circ H(q, p)$, where $f \in C^1$ and is monotonic, is

also canonical. The two systems have the same trajectories and equivalent dynamics up to a reparameterization of time by a factor of $f'(H)$.

We apply this observation to the Hamiltonian (5.3), which we note is singular at $(X, Y) = (0, 0)$. In this limit $\alpha \to 1^-$, in which each of the like-signed pairs coalesces into vortex with circulation either plus or minus two. This causes the frequency of nearby oscillations to diverge to infinity. In order to desingularize the dynamics in this neighborhood, we redefine the Hamiltonians (5.3) using

$$\tilde{H} = f(H) = \frac{1}{2} e^{\frac{1}{2}H},$$

yielding the non-singular Hamiltonian in the invariant plane

$$\tilde{H}(X, Y) = e^{\frac{1}{2}H(X,Y)} = \frac{1}{2}\left(\frac{1}{1 - Y^2} - \frac{1}{1 + X^2}\right) \tag{5.4}$$

and the new time scale

$$\tilde{t} = \frac{1}{f'(H)} t = e^{-\frac{1}{2}H} t. \tag{5.5}$$

For ease of notation, we will drop the tildes for the remainder of the paper. We also break with prior convention and use the value h of the Hamiltonian H in (5.4) to parameterize the family of solutions, rather than using the ratio of the breadths of the vortex pairs, α, as was done in previous work [2,34,55]. With regards to α, Aref's critical value is $\alpha_c = \frac{3-\sqrt{5}}{2}$ and leapfrogging motion occurs for $3 - 2\sqrt{2} < \alpha < 1$. With respect to energy level, h, leapfrogging motions occur for $0 < h < h_s = \frac{1}{2}$ and the leapfrogging motion has been found numerically to be stable for $0 < h < h_c = \frac{1}{8}$. The two parameters are related by $h = \frac{(1-\alpha)^2}{8\alpha}$. A detailed comparison of parameters and their critical values in the literature can be found in Appendix A.

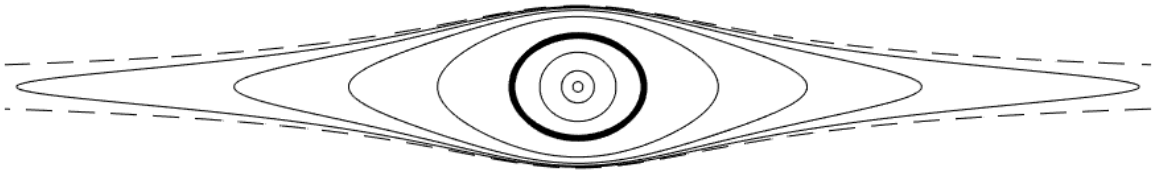

Figure 5.1 Level sets of the one-degree-of-freedom Hamiltonian (5.4) in the $X-Y$ plane, including the critical energy level $H = h_c$ (bold) and the separatrix at $H = h_s = \frac{1}{2}$ (dashed). Unbounded orbits not shown. The center at the origin corresponds $h = 0$ in (5.4) and to the limiting physical state in which the pairs of like-vorticity are at an infinitesimal distance and rotate with a divergent frequency as described by the original Hamiltonian. Stable orbits foliate the area between this point and the critical energy level.

The Hamiltonian (5.4) yields evolution equations

$$\begin{aligned} \frac{dX}{dt} &= \frac{\partial H}{\partial Y} = \frac{Y}{(1-Y^2)^2}, \\ \frac{dY}{dt} &= -\frac{\partial H}{\partial X} = -\frac{X}{(1+X^2)^2}, \end{aligned} \tag{5.6}$$

whose phase plane is shown in Figure 5.1. In [27], Gröbli integrated the equations of motion (5.6) to find an implicit formula for $X_h(t)$. In our notation, this is given by

$$\begin{aligned} t(X) = &\frac{1}{2h^2\sqrt{1-4h^2}} F\left(\sin^{-1}\theta \middle| k\right) - E\left(\sin^{-1}\theta \middle| k\right) \\ &- \frac{1+2h}{2h\sqrt{(1-2h)\left(2h\left(X^2+1\right)+1\right)}}, \end{aligned} \tag{5.7}$$

where $\theta = X\sqrt{\frac{2h-1}{2h}}$, $k^2 = \frac{4h^2}{4h^2-1}$, and F and E are incomplete elliptic integral of the first and second kind respectively. For details on this calculation, see Appendix B. To study the stability of these trajectories as solutions to (5.3), it would be useful to write $X(t)$ and $Y(t)$ in an explicit closed form. Unfortunately, (5.7) does not seem to be invertible to yield an explicit formula for $X(t)$. Nonetheless, in Section 5.4 we reformulate the problem in order to provide an explicit formulation of the stability problem without having to invert this formula.

5.3 Floquet Theory and the Linearized Perturbation Equations

As discussed in Section 2.3.2, to analyze the linear stability of the periodic orbit γ_h given by $(X_h(t), Y_h(t), 0, 0)$, we perturb the evolution equations corresponding to Hamiltonian (5.2) about the leapfrogging solution $(Q_1, P_1, Q_2, P_2) = (X(t), Y(t), 0, 0)$. We introduce perturbation coordinates

$$(Q_1(t), P_1(t), Q_2(t), P_2(t)) = (X(t) + \epsilon\xi_+(t), Y(t) + \epsilon\eta_-(t), \epsilon\xi_-(t), \epsilon\eta_+(t))$$

and expand the ODE system, keeping terms of linear order in ϵ. The resulting equations decouple into two 2×2 systems,

$$\frac{d}{dt}\left[\xi_+, \eta_-\right]^\mathsf{T} = A^\mathsf{T}(X, Y)\ \left[\xi_+, \eta_-\right]^\mathsf{T} \quad \text{and} \tag{5.8a}$$

$$\frac{d}{dt}\left[\xi_-, \eta_+\right]^\mathsf{T} = A(X, Y)\left[\xi_-, \eta_+\right]^\mathsf{T}, \tag{5.8b}$$

where $A(X, Y)$ is given by

$$A = \begin{pmatrix} \frac{XY}{(X^2+Y^2)(1+X^2)(1-Y^2)} & -\frac{3Y^4+X^2Y^2+X^2-Y^2}{2(X^2+Y^2)(1-Y^2)^3} \\ -\frac{3X^4+X^2Y^2-Y^2+X^2}{2(X^2+Y^2)(1+X^2)^3} & -\frac{XY}{(X^2+Y^2)(1+X^2)(1-Y^2)} \end{pmatrix}.$$

Because these two systems depend only on quadratic terms in (X, Y), the coefficient matrices have period $\frac{1}{2}T_{\text{leapfrog}}$. Each is a linear Hamiltonian system since the matrix $A(t)$ on the right-hand side can be written as $A = JH$ where $J = \left(\begin{smallmatrix} 0 & 1 \\ -1 & 0 \end{smallmatrix}\right)$ and H is symmetric.

In order to analyze these equations, we need to understand the behavior of solutions to the linear system with time-periodic coefficients, dependent on a parameter h,

$$\dot{X} = A(t; h)X, \quad A(t) = A(t + T; h), \tag{5.9}$$

which is known as a Floquet problem [22, 40, 65]. To understand the behavior of solutions of equations of the form (5.9), we must review some basic facts from Floquet

theory from Section 2.3.3. Define the fundamental solution operator $\Phi(t)$ as the matrix-valued solution to (5.9) with $\Phi(0) = I$. The *monodromy matrix* is defined as the solution operator evaluated at one period $M = \Phi(T)$. The eigenvalues, λ, of M are called the Floquet multipliers. If any multiplier λ satisfies $|\lambda| > 1$, then the solutions of the system of equations (5.9) include an exponentially growing solution and the system is considered unstable.

If $A(t)$ is a 2×2 Hamiltonian matrix, the Floquet multipliers comes in pairs $\lambda_1(h)$ and $\lambda_2(h)$ such that $\lambda_1\lambda_2 = 1$. If $\lambda_{1,2}$ have a nonzero imaginary part, then the two multipliers must lie on the unit circle and be conjugate. If $\lambda_{1,2}$ are real and $|\lambda_1| \neq 1$, then one multiplier lies inside the unit circle, and the other lies outside the unit circle. The system is then unstable. On the boundary between stability and instability, the two eigenvalues must lie on the unit circle and be real-valued, i.e., they must satisfy $\lambda_1 = \lambda_2 = \pm 1$.

The Floquet multipliers depend continuously on the parameter h. Therefore, bifurcations, i.e., changes in stability, can only occur with $\lambda_1 = \lambda_2 = \pm 1$ [65]. The existence of a multiplier $\lambda = 1$ (respectively $\lambda = -1$) corresponds to the existence of a periodic orbit with period T (respectively, an anti-periodic orbit of half-period T). The stability or instability is easily determined by examining $\mathrm{tr}(M) = \lambda_1 + \lambda_2$, with stability in the case $|\mathrm{tr}(M)| < 2$ and instability when $|\mathrm{tr}(M)| > 2$. At the bifurcation values, $\mathrm{tr}\, M = 2$ and $\mathrm{tr}\, M = -2$, the system (5.9) has a periodic orbit or an anti-periodic orbit, respectively.

We now return to the linearized perturbation equations of the leapfrogging orbit (5.8). The coordinates (ξ_+, η_-) describe perturbations within the family of periodic orbits. As such, the monodromy matrix for equation (5.8a) has eigenvalues $\lambda_{1,2} \equiv 1$ which can lead to at most linear-in-time divergence of trajectories; see [55]. The question of stability is therefore determined entirely by the second system (5.8b).

Let $Z = (\xi_-, \eta_+)$, then (5.8b) can be written as

$$\frac{dZ(t)}{dt} = A(X_h(t), Y_h(t))Z(t), \tag{5.10}$$

where

$$A(t) = A\left(t + \frac{1}{2}T_{\text{leapfrog}}(h)\right),$$

and the period of the leapfrogging motion, T_{leapfrog}, can be found from (5.7) and is given by

$$T_{\text{leapfrog}}(h) = \frac{8h^2}{1-h^2}\left(h^2 E\left(\frac{1}{h}\right) + \left(1-h^2\right) K\left(\frac{1}{h}\right)\right),$$

where E and K are complete elliptic integrals of the first and second kind, respectively.

5.4 Explicit Form of the Floquet problem

5.4.1 Reformulation in Terms of the Canonical Polar Angle

The coordinates X_h and Y_h can not be solved in closed form. This is not a problem when finding the Floquet multipliers numerically, but it will be analytically useful to have an explicit form of the Floquet problem. To this end, we change the independent variable in a manner inspired by the proof that bounded solutions to the gravitational two-body problem are ellipses. Consider the canonical polar coordinates [41],

$$X = \sqrt{2J}\cos\theta \quad \text{and} \quad Y = \sqrt{2J}\sin\theta. \tag{5.11}$$

This transformation preserves the Hamiltonian structure of the equations of motion, i.e.,

$$\frac{d\theta}{dt} = \frac{\partial H}{\partial J} \quad \text{and} \quad \frac{dJ}{dt} = -\frac{\partial H}{\partial \theta}.$$

We rewrite (5.10) as a Floquet problem with the polar angle θ as an independent variable. With respect to the variables θ and J, the Hamiltonian (5.4) can be rewritten

as

$$H(J,\theta) = \frac{2J}{2 - J^2 - 4J\cos 2\theta + J^2\cos 4\theta}.$$

At a given energy level $H = h$, we can solve for J,

$$J_{\pm} = \frac{1 + 2h\cos 2\theta \pm \sqrt{1 + 4h^2 + 4h\cos 2\theta}}{h(-1 + \cos 4\theta)}. \tag{5.12}$$

Of these two roots, only J_- is both positive and free from singularities. Thus from here on, we set $J = J_-(h,\theta)$. Since (5.11) is a canonical transformation, it preserves Hamilton's equations of motion. Therefore, θ evolves as

$$\begin{aligned}\frac{d\theta}{dt} = \frac{\partial H}{\partial J} = \ & \frac{1}{2}\Big(1 + 4h^2 + 4h\cos 2\theta \\ & + (1 + 2h\cos 2\theta)\sqrt{1 + 4h^2 + 4h\cos 2\theta}\Big).\end{aligned} \tag{5.13}$$

where we have used (5.12) to write (5.13) in terms of h and θ.

In these variables, the Floquet matrix in (5.10) is given by

$$A(J,\theta) = \begin{pmatrix} \frac{-\sin 2\theta}{(-1+J+J\cos 2\theta)(-1-J+J\cos 2\theta)} & \frac{(2+6J)\cos 2\theta - J(5+\cos 4\theta)}{2(-1-J+J\cos 2\theta)^3} \\ \frac{(2-6J)\cos 2\theta - J(5+\cos 4\theta)}{2(-1+J+J\cos 2\theta)^3} & \frac{\sin 2\theta}{(-1+J+J\cos 2\theta)(-1-J+J\cos 2\theta)} \end{pmatrix}. \tag{5.14}$$

Using (5.12), J can be eliminated from $A(J,\theta)$ in (5.14) and it can be written as a function $A_h(\theta)$ depending on the parameter h alone. Since

$$\frac{dZ(\theta)}{d\theta}\frac{d\theta}{dt} = A_h(\theta)Z(\theta), \tag{5.15}$$

equation (5.13) can be used to write this as

$$\frac{dZ(\theta)}{d\theta} = \tilde{A}_h(\theta)Z(\theta) \quad \text{where} \quad \tilde{A}_h(\theta) = \left(\frac{d\theta}{dt}\right)^{-1} A_h(\theta). \tag{5.16}$$

In what follows, we drop the tilde from this notation.

In particular, at the apparent bifurcation value $h = 1/8$, the coefficient matrix is given by

$$A_{h=\frac{1}{8}}(\theta) = \frac{1}{\sqrt{17+8\cos 2\theta}} \begin{pmatrix} -4\sin 2\theta & \frac{7+12\cos 2\theta - 4\cos 4\theta - 3\sqrt{17+8\cos 2\theta}}{-2+2\cos 2\theta} \\ \frac{3-4\cos 2\theta - 4\cos 4\theta - \sqrt{17+8\cos 2\theta}}{2+2\cos 2\theta} & 4\sin 2\theta \end{pmatrix}. \tag{5.17}$$

An additional benefit is that in this approach, the period is independent of h since $A_h(\theta) = A_h(\theta + \pi)$.

5.4.2 Numerical Solution of the Floquet Problem

Using this explicit construction, we give two numerical checks for the critical value of $h_c = \frac{1}{8}$. Let M_h be the monodromy matrix of the system (5.16), and define the function $f(h) = \operatorname{tr} M_h - 2$. We used MATLAB's built in rootfinder, `fzero` along with the ODE Solver `ode45` with a relative tolerance of 10^{-13}, an absolute tolerance of 10^{-15} to solve the equation $f(h_c) = 0$. Using an initial value of $h = 0.1$, the solver returned the numerical solution $h_c = 0.125$ to within machine error. Note that constructing $f(h)$ requires the numerical solution of the Floquet problem. See Figure 5.2(a).

Another test, which is more relevant for the approach used in Section 5.6, is to check that the solution to (5.17) has a periodic solution with an initial value of $Z(\theta) = (1, 0)^{\mathsf{T}}$. In this formulation only a single system of two ODEs must be integrated. Using arbitrary precision arithmetic and a 30th order Taylor method using the Julia package `TaylorIntegration.jl` [48], we find that the numerical solution satisfies $||Z(\pi) - Z(0)||_2 < 10^{-120}$. This is consistent with the hypothesis that Z has a periodic solution of period π and that h_c is truly rational up to the accuracy of the simulation. See Figure 5.2(b).

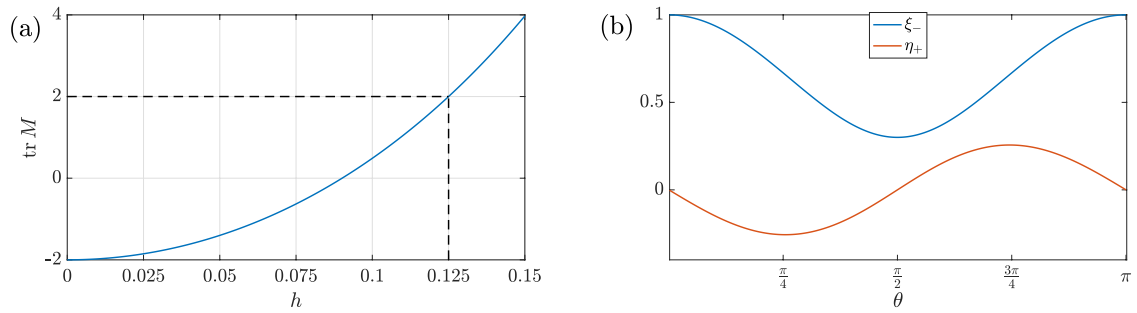

Figure 5.2 (a) The trace of the monodromy matrix as a function of the energy h. (b) The periodic orbit at $h = \frac{1}{8}$.

5.4.3 Expansion in h

The method of harmonic balance used in Section 5.6 requires that the Floquet matrix $A_h(\theta)$, with explicit form (5.16), be written as a Fourier series. To accomplish this, we expand A_h in a Maclaurin series in h and find at each order in h a finite Fourier expansion. Letting

$$A_h(\theta) = \sum_{k=0}^{\infty} h^k A_k(\theta),$$

the first few terms are given by

$$A_0(\theta) = \begin{pmatrix} -\sin 2\theta & -\cos 2\theta \\ -\cos 2\theta & \sin 2\theta \end{pmatrix},$$

$$A_1(\theta) = \begin{pmatrix} \sin 4\theta & 3 + \cos 4\theta \\ 3 + \cos 4\theta & -\sin 4\theta \end{pmatrix},$$

$$A_2(\theta) = \frac{1}{2} \begin{pmatrix} \sin 2\theta - 3\sin 6\theta & -12 - 9\cos 2\theta - 3\cos 6\theta \\ 12 + 9\cos 2\theta - 3\cos 6\theta & -\sin 2\theta + 3\sin 6\theta \end{pmatrix}.$$

To perform a perturbation expansion, it is preferable that the leading-order term has constant-valued coefficients. The system can be put in such a form by a θ-dependent change of variables known as a Lyapunov transformation, which we

construct. First note that the matrix

$$B(\theta) = \begin{pmatrix} \cos\theta & -\sin\theta \\ \sin\theta & \cos\theta \end{pmatrix} \tag{5.19}$$

is the fundamental solution matrix of the system

$$\frac{dB}{d\theta} = A_0 B.$$

Under the canonical change of variables $W(\theta) = B(\theta)Z(\theta)$, the system (5.10) becomes

$$\begin{aligned} \frac{dW}{d\theta} &= \frac{dB}{d\theta}Z + B\frac{dZ}{d\theta} \\ &= \frac{dB}{d\theta}B^{-1}W + BAZ \\ &= \left(\frac{dB}{d\theta}B^{-1} + BAB^{-1}\right)W. \end{aligned}$$

Letting

$$C(\theta) = \frac{dB}{d\theta}B^{-1} + BAB^{-1},$$

then

$$\frac{dW}{d\theta} = C_h(\theta)W, \tag{5.20}$$

where the first few terms in the series

$$C_h(\theta) = C_0 + \sum_{k=1}^{\infty} h^k C_k(\theta) \tag{5.21}$$

are

$$C_0(\theta) = \begin{pmatrix} 0 & -2 \\ 0 & 0 \end{pmatrix},$$

$$C_1(\theta) = \begin{pmatrix} -2\sin 2\theta & 4\cos 2\theta \\ 4\cos 2\theta & 2\sin 2\theta \end{pmatrix},$$

$$C_2(\theta) = \begin{pmatrix} \sin 4\theta & -8 - \cos 4\theta \\ 4 - 4\cos 4\theta & -\sin 4\theta \end{pmatrix},$$

$$C_3(\theta) = \begin{pmatrix} -5\sin 2\theta - \sin 6\theta & 26\cos 2\theta + 6\cos 6\theta \\ -6\cos 2\theta + 6\cos 6\theta & 5\ \sin 2\theta + \ \sin 6\theta \end{pmatrix},$$

including a leading-order term that is independent of θ, as desired.

5.5 Perturbative Expansion for Monodromy Matrix

Using the expansion presented in Section 5.4.3, we implement an algorithm introduced by Casas and collaborators [16] and introduced in Section 2.4. The method is the combination of three ideas—the Magnus expansion, the Lyapunov transform, and Lie transform perturbation theory—to construct an approximation to the monodromy matrix of a linear Hamiltonian system with periodic coefficients. A Mathematica implementation of this algorithm was made in preparation for this proposal and is also available.

There exist other algorithms [65] to construct solutions to the Floquet problem perturbatively and approaches using harmonic balance [52]; however, this method has two significant advantages. The Magnus expansion has the advantage that the approximate fundamental solution operator will always be in the same Lie algebra as the exact operator. As the systems under consideration here are Hamiltonian, this means the approximate fundamental solution matrix is symplectic. From the use of

the Lie transforms, the solution procedure is also recursive and very easy to code in a CAS.

This algorithm constructs a power series in h for P and K in the Floquet normal form $Z(t) = P(t)^{tK}$. All information on the stability of the system will be contained in K. The change in stability will occur either when the trace of the monodromy matrix, $e^{2\pi K}$, equals two or, equivalently, when the determinant of K vanishes.

Let K_n represent the nth order approximation. For example, the third order approximation is

$$K_3(h) = \begin{pmatrix} 0 & -2 - 12h - 63h^2 - 570h^3 \\ 12h^2 - 72h^3 & 0 \end{pmatrix} \tag{5.22}$$

with determinant

$$\begin{aligned} |K_3| &= -K_3(1,2)K_3(2,1) \\ &= \left(2 + 12h + 63h^2 + 570h^3\right)\left(12h^2 - 72h^3\right). \end{aligned}$$

Since

$$\frac{d}{dh}\left(2 + 12h + 63h^2 + 570h^3\right) = 12 + 126h + 1710h^2 = 1710\left(\frac{126}{3420} + h\right)^2 + \frac{1839}{190} > 0$$

the second factor is always increasing and must always be positive for $h > 0$, there the only nonzero root occurs at $h = \frac{12}{72} = \frac{1}{6}$. This is close to the critical energy $E_c = \frac{1}{8}$. Alternatively, analyzing the trace of the monodromy matrix,

$$\mathrm{tr}\left(e^{2\pi K_3(h)}\right) = 2\cosh\left(2\pi h\sqrt{-24 + 108h^2 - 2304h^3 + 41040h^4}\right) = 2$$

leads us to the same polynomial as when considering $|K_3|$, as expected.

Our calculations show that, as for K_3, K_n is always zero along the diagonal. Therefore, for all n calculated, $|K_n| = -K_n(1,2)K_n(2,1)$. However, $K_n(1,2)$ never

has roots for positive h and $K_n(2,1)$ has a positive root only for odd n. The first few relevant factors are:

$$
\begin{aligned}
K_3(1,2) &= 12h^2 - 72h^3, \\
K_5(1,2) &= 12h^2 - 72h^3 + 348h^4 - 3240h^5, \\
K_7(1,2) &= 12h^2 - 72h^3 + 348h^4 - 3240h^5 + 19017h^6 - 165942h^7, \\
&\vdots \\
K_{17}(1,2) &= 12h^2 - 72h^3 + 348h^4 - 3240h^5 + 19017h^6 - 165942h^7 \\
&\quad + 1073361h^8 - 9095238h^9 + \frac{991023639}{16}h^{10} - \frac{4137261381}{8}h^{11} \\
&\quad + \frac{58147963803}{16}h^{12} - \frac{240640073505}{8}h^{13} + \frac{13817540313693}{64}h^{14} \\
&\quad - \frac{56853585645399}{32}h^{15} + \frac{828635606507637}{64}h^{16} \\
&\quad - \frac{3395564189849295}{32}h^{17} + \frac{3203875950715252755}{4096}h^{18}.
\end{aligned}
$$

and the roots are given by Table 5.1.

Table 5.1 Roots of the Averaged Monodromy Matrix

n	$h_c^{(n)}$
3	0.1667
5	0.1391
7	0.1330
9	0.1305
11	0.1292
13	0.1283
15	0.1278
17	0.1274

As n increases, the roots do seem to converge (rather slowly) to $E_c = \frac{1}{8} = .125$. This convergence can also be visualized by looking at when the Floquet exponents (the eigenvalues of K) are zero. While this approach seems to work, it is rather slow.

5.6 Method of Harmonic Balance and the Hill's Determinant

We now present an alternate approach to Section 5.5. In this section, we apply the method of harmonic balance (MHB) to the π-periodic differential equation (5.20). As noted in Section 5.3, at parameter values where the system undergoes a bifurcation, there must exist either a periodic orbit or an anti-periodic orbit. The idea behind this method is that if such an orbit exists, then it has a convergent Fourier series, which can be found if an approximate solvability condition for its coefficients is satisfied. In this section, we provide a brief overview of the method. For a thorough classical overview, see [62]. This method is discussed in detail in Section 2.3.4.

To apply the method of harmonic balance, we write the periodic solution to system (5.20) as a Fourier series. The following two observations allow us to simplify the form of this series. First, we observe that the first component of numerical solution $Z(\theta)$ computed in Section 5.4.2 is an even function, and the second component is an odd function. Second, because it has a period of π, its Fourier series contains only even harmonics. Noting the definition of $W(\theta)$ using (5.19), this implies that $W(\theta)$ has only odd harmonics in its Fourier expansion. These two facts imply that $W(\theta) = (\xi_h, \eta_h)^\mathsf{T}$ has the following Fourier expansion:[1]

$$\xi_h(\theta) = \sum_{n=1}^{\infty} a_n(h) \cos(2n-1)\,\theta \quad \text{and} \quad \eta_h(\theta) = \sum_{n=1}^{\infty} b_n(h) \sin(2n-1)\,\theta. \tag{5.23}$$

[1]This expansion contained only one-fourth of the possible non-zeros terms and was based on mere observation from numerical simulations. It would, of course, be possible to proceed with a more general Fourier ansatz. We have done this and found that the computed Hill determinant factors into several terms. Of these terms, only the one corresponding to the above expansion ever vanishes, so that no generality has been lost.

We found using a trigonometric basis here to be more natural than the complex exponential basis used in (2.14). Putting this ansatz into the Floquet system (5.20) and collecting coefficients of the harmonics formally results in an infinite-dimensional matrix problem $M(h)\mathbf{a} = 0$ where $\mathbf{a} = [a_1, b_1, a_2, b_2, \ldots]^\mathsf{T}$.

To follow the approach of Hill, we need to truncate the Fourier ansatz (5.23) to $1 \leq n \leq N$. Simultaneously, we truncate the series (5.21) to $0 \leq k \leq N$,

$$C_h^{(N)}(\theta) = C_0 + \sum_{k=1}^{N} h^k C_k(\theta).$$

We therefore consider the sequence of truncated linear systems $M^{(N)}\mathbf{a}_N = \mathbf{0}$, where

$$\mathbf{a}_N = [a_1, b_1, a_2, b_2, \ldots, a_N, b_N]^\mathsf{T}.$$

This has nontrivial solutions if and only if $M^{(N)}(h)$ is singular, i.e., if $\left|M^{(N)}(h)\right| = 0$. We have automated this procedure in Mathematica [64] and can compute the result at arbitrary truncation order. The first two such truncated systems are

$$\left|M^{(1)}\right| = \begin{vmatrix} -1+h & 2+2h \\ -2h & 1-h \end{vmatrix} = -1 + 6h + 3h^2,$$

$$\begin{aligned} \left|M^{(2)}\right| = &\begin{vmatrix} -1+h & 2+2h+8h^2 & -h-\frac{h^2}{2} & -2h-2h^2 \\ -2h-4h^2 & 1-h & -2h+2h^2 & -h+\frac{h^2}{2} \\ h-\frac{h^2}{2} & -2h-2h^2 & -3 & 2+8h^2 \\ -2h+2h^2 & h+\frac{h^2}{2} & -4h^2 & 3 \end{vmatrix} \\ = \; & 9 - 54h - 109h^2 - 210h^3 - \frac{977}{2}h^4 \\ & + \frac{1049}{2}h^5 + \frac{75}{2}h^6 + 1074h^7 + \frac{11233}{16}h^8. \end{aligned}$$

The relevant root of $\left|M^{(1)}\right| = 0$ can be found in closed form, $h_c^{(1)} = 2/\sqrt{3} - 1 \approx 0.1547$, but the roots of the truncations at higher order must be found numerically. We have calculated the roots for several values of N and have tabulated them in Table 5.2.

As expected, we observe convergence to $h = \frac{1}{8}$. By a least-squares fit we find that the error, $\left| h_c^{(N)} - \frac{1}{8} \right|$, decays at a rate of about 4^{-N}. Ultimately, we conclude that this spectral approach converges more rapidly than the result from Section 5.5 which used averaging.

5.7 Proof of Bifurcation at $E_c = \frac{1}{8}$

The preceding results of this chapter strongly suggests that the bifurcation occurs at exactly $h = \frac{1}{8}$. By the arguments in Section 5.4, if a periodic solution to the explicit Floquet problem[2] at $h = \frac{1}{8}$ exists, the result will be proven. Finding a periodic solution to (5.17) with initial condition $Z(\theta) = (1, 0)^{\mathsf{T}}$ would complete our argument. A straightforward calculation shows that the following periodic solutions solve our initial-value problem:

$$\begin{aligned} \xi_-(\theta) &= \frac{1}{20}\left(1 + 4\cos 2\theta + 3\sqrt{17 + 8\cos 2\theta}\right) \\ \eta_+(\theta) &= -\frac{\tan\theta}{20}\left(1 + 4\cos 2\theta + \sqrt{17 + 8\cos 2\theta}\right). \end{aligned}$$

[2]Having reduced the problem to solving an elementary system of time-periodic ODEs, this formulation seemed to be a perfect to open source on the mathematicians' question-and-answer site `mathstackoverflow.net`. The hope was that someone had seen something that we had missed. Remarkably, Robert Israel (Professor Emeritus, University of British Columbia) observed that this problem could be solved in closed form with Maple [37] (we had exclusively used Mathematica [64] as our CAS).

Table 5.2 Roots of the Truncated Hill Determinants

N	$h_c^{(N)}$
1	0.154700538379256
2	0.125362196172840
3	0.125302181592097
4	0.125039391697053
5	0.125013678063844
6	0.125002532983010
7	0.125000749452121
8	0.125000157555837
9	0.125000043690148
10	0.125000009756739
11	0.125000002617060
12	0.125000000604347
13	0.125000000158988
14	0.125000000037475
15	0.125000000009738
16	0.125000000002326
17	0.125000000000599
18	0.125000000000145
19	0.125000000000037
20	0.125000000000009

CHAPTER 6

PHENOMENOLOGY OF THE MOTIONS OF THE FOUR-VORTEX PROBLEM

The goal of this chapter is to describe the fundamental motions of the vortex quartet and understand where they reside in phase-space and their relationship to the corresponding states of the three-vortex problem discussed in Section 4.2. We begin in Section 6.1 by discussing the regular motions of the vortex quartet–(mixed-period) leapfrogging, walkabout and braids. We examine these motions in both the Aref-Eckhardt and Dimer coordinates developed in Chapter 4, ultimately preferring the Dimer coordinates to examine the phase-space of the vortex quartet. In Section 6.2, we use the Poincaré surface of section and Lagrangian descriptors to examine the chaotic motions, such as the chaotic transitions from aperiodic leapfrogging, walkabouts, and braiding, see Figure 6.1(a) and (b). In particular, we explain why the chaotic braids seen in see Figure 6.1 (b) are both rare, overlooked, *and* fundamental to explaining the phase-space structure of the vortex quartet.

This overview of the phenomenology of the vortex quartet will prepare the reader for Chapter 7, which focuses on the breakdown of the structures that are encountered in this chapter. The breakdown of these structures is what allows or prevents transitions from the different regimes of phase-space, such as when a walkabout-to-disintegration or disintegration occurs, see Figure 6.1(c) and (d).

6.1 Regular Motion

In the section, we review various motions of the vortex quartet: leapfrogging, mixed-period leapfrogging, walkabouts, and braiding, paying particular attention to the simple form they take in the $(\mathbf{z}_1, \mathbf{z}_2) := (q_1, p_1, q_2, p_2)$-coordinates used in the 'Dimer' Hamiltonian formulation (4.13) compared to their form in the

$(\mathbf{Z}_1, \mathbf{Z}_2) := (Q_1, P_1, Q_2, P_2)$-coordinates used in the Aref-Eckhardt Hamiltonian (5.2), and especially the suitability of the former coordinate system for Poincaré sections. We present a series of figures showing the trajectories in physical space as well as in both of the reduced coordinate systems.

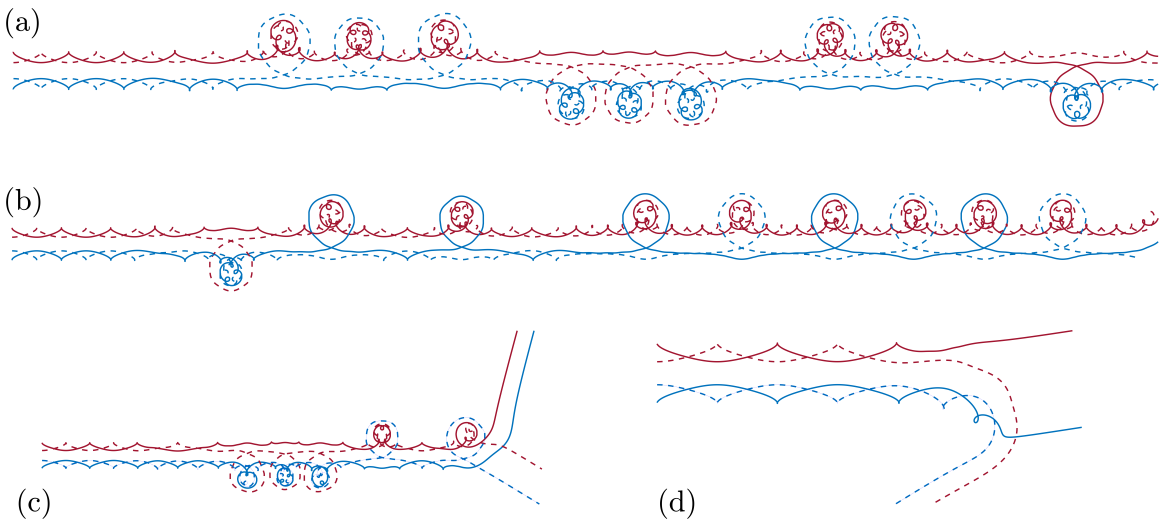

Figure 6.1 Motion in physical space. (a) A trajectory featuring several bouts of walkabout motion including one extended period of three consecutive walkabout 'dances'. (b) A trajectory featuring first walkabout orbits and later braiding orbits, as the two negative (blue) vortices take turns orbiting the tightly bound pair of positive (red) vortices.
(c) A leapfrogging motion that transitions to walkabout motion before disintegrating.
(d) A leapfrogging motion that disintegrates without a walkabout stage.

Leapfrogging

In the Aref-Eckhardt coordinates, the $\mathbf{Z}_1$ coordinate of the leapfrogging orbit is periodic while the $\mathbf{Z}_2$ coordinate is identically zero, while in the dimer coordinate system, both $\mathbf{z}_1$ and $\mathbf{z}_2$ undergo nontrivial periodic motion. The dynamics in a neighborhood of this orbit are, therefore, simpler in the Aref-Eckhardt coordinates used in previous studies. This separation of motion makes this coordinate system useful for studying the linear stability of the leapfrogging orbit, see Figure 6.2.

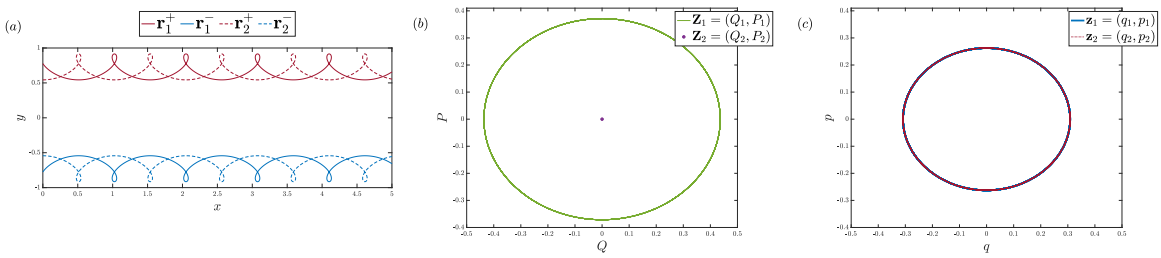

Figure 6.2 A typical leapfrogging motion in (a) Lab coordinates (physical space) (b) Phase space in Aref coordinates (c) Phase space in dimer coordinates (the red and blue trajectories coincide).

Mixed-Period Leapfrogging

Figures 6.3 and 6.4 show orbits observed by Whitchurch et al. called, respectively, two-to-one and three-to-one mixed-period leapfrogging orbits. In Figure 6.3, the two positive-signed vortices move through two periodic motions per every periodic motion of the negative signed vortices giving a 2:1 ratio, while Figure 6.4 shows a 3:1 ratio. The dimer coordinates here do a better job of separating the two time-scales of the motion and providing orbits with monotonic phases useful for numerically computing Poincaré sections. Both the leapfrogging and mixed-period leapfrogging motions correspond to orbits in Region I of Figure 4.2.

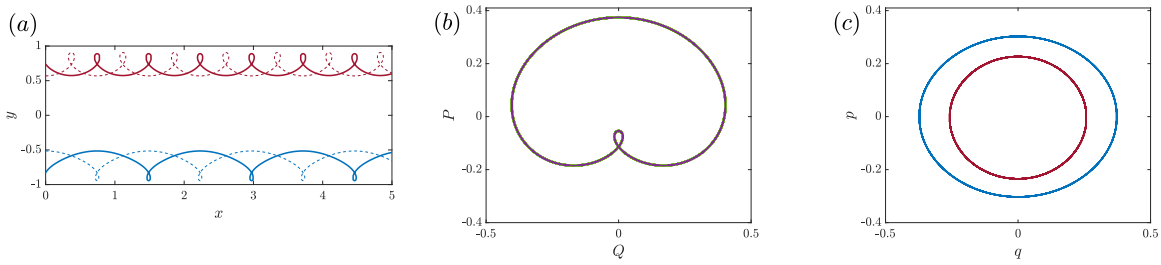

Figure 6.3 A mixed leapfrogging motion with a ratio of two-to-one in (a) Lab coordinates (physical space) (b) Phase-space using Aref coordinates
(c) Phase-space using dimer coordinates.

Walkabout

Walkabouts are analogous to the $-1{:}-1{:}2$ three-vortex motion seen in Region II of Figure 4.2. The vortex with circulation two has been replaced by a pair of vortices

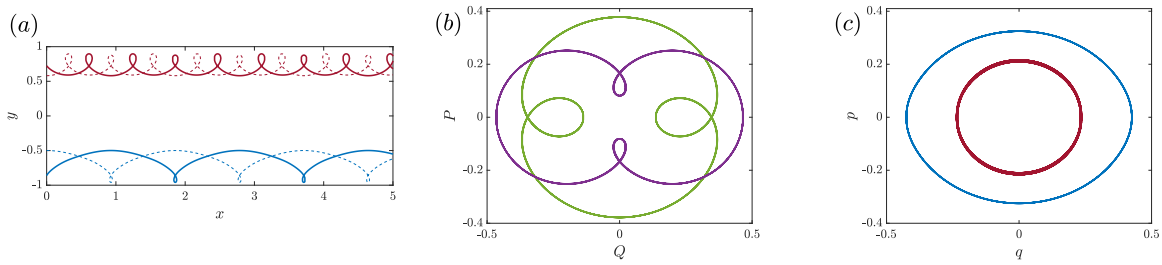

Figure 6.4 A mixed leapfrogging motion with a ratio of three-to-one in (a) Lab coordinates (physical space) (b) Phase-space using Aref coordinates
(c) Phase-space using dimer coordinates.

of circulation one orbiting rapidly about their common center of vorticity while the two negative vortices move approximately to the motion seen in Figure 6.5(a). The motion in Aref-Eckhardt coordinates seen in Figure 6.5(b) fails to separate the fast and slow motions, whereas in the dimer coordinates seen in Figure 6.5(c), the fast time scale of the motion of the positive vortices is separated from the slower motion of the two negative vortices. A typical dimer will rotate at a rate of one to three orders of magnitude than the walkabout motion frequency.

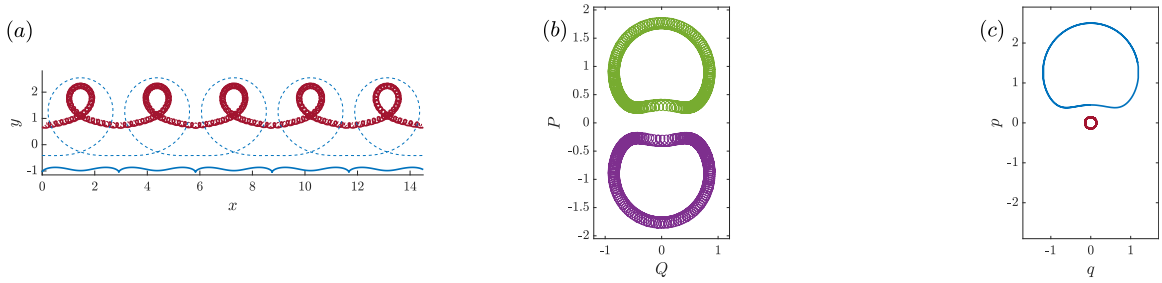

Figure 6.5 Walkabout motion in (a) Lab coordinates (b) Phase-space using Aref coordinates (c) Phase-space using dimer coordinates.

Braiding

Braiding orbits are analogous to the $-1\text{:}-1:2$ three-vortex motion seen in Region III of Figure 4.2. As in the walkabouts, the vortex with circulation two is replaced by a pair of vortices orbiting about their common center of vorticity while the two negative vortices move along similar trajectories to those shown in Figure 6.6(a).

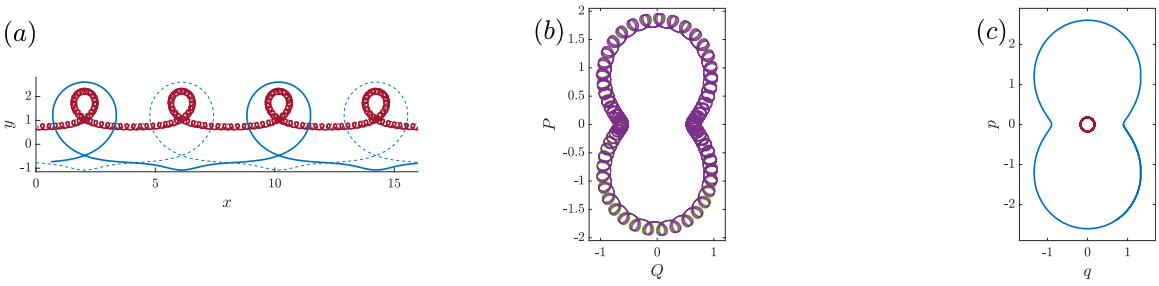

Figure 6.6 Braiding motion in (a) Lab coordinates (b) Phase-space using Aref coordinates (c) Phase-space using dimer coordinates.

Remark 6.1.1. *For typical orbits, the dimer motions rotate at a frequency one to three orders of magnitude larger than the walkabout and braiding motions. If this ratio is a rational number, the*

6.2 Chaotic Motion and the Poincaré Surface of Section

In addition to the regular bounded motions discussed in the previous section, there exist chaotic orbits that, depending on the energy, may spend time in one or more of the three regions of phase space. These may, at times, resemble any of the families of orbits previously discussed. Figure 6.7 shows the orbits from Figure 6.1 in the dimer coordinates. Figure 6.7(a) shows bouts of leapfrog-like and walkabout-like chaotic motion while Figure 6.7(b) shows bouts of braid-like motion as well. At higher energies, we observe two types of escape: in the first, the vortices go through a period of walkabout motions, as shown in Figure 6.7(c) before eventually escaping. In the second, the vortices immediately disintegrate without going into walkabout motion, see Figure 6.7(d).

The Poincaré surface of section A standard tool for visualizing dynamics in more than two dimensions is to reduce the dimensions using the Poincaré Surface of Section (PSS). The PSS provides qualitative information about essential structures of a dynamical system such as periodic and quasi-periodic orbits, KAM tori and their breakup, and the presence of stochastic regions. For a detailed description,

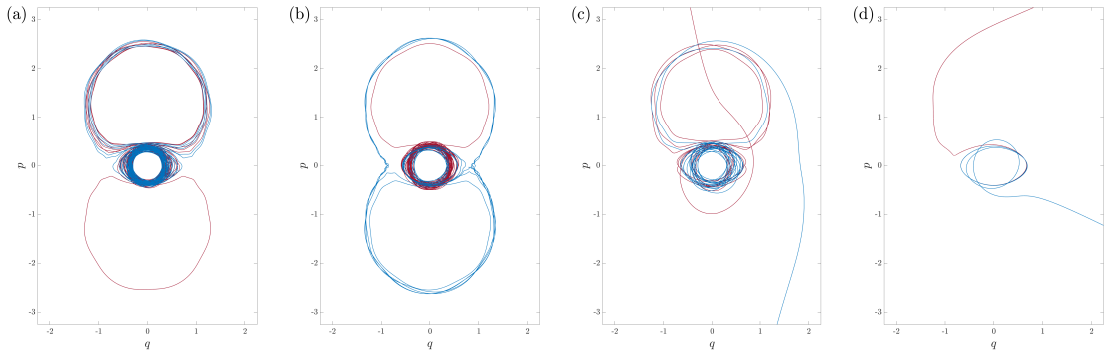

Figure 6.7 Corresponding motions to Figure 6.1. (a) Walkabout. (b) Walkabout with braiding. (c) Walkabout to disintegration. (d) Disintegration.

see Section 2.3.1. It does not provide information about escape nor a complete picture of the underlying invariant manifolds that provide the skeleton of phase space. Therefore, we complement the visualizations using the PSS with the direct numerical computation of invariant manifolds for specific fixed points, using the method of adaptive linear interpolation (ALI+) described by Goodman and Wróbel [26]. We also use plots of Lagrangian descriptors to visualize the global structure of the invariant manifolds.

For a two-degree-of-freedom Hamiltonian, each orbit lies on a three-dimensional energy surface, $\mathcal{E}_h = \{\mathbf{z} : H(\mathbf{z}) = h\}$. The PSS is created by looking at the flow on a cross-section of this surface. This cross-section is formed by taking the hyperplane Σ_h, defined by enforcing that $q_1 = 0$ and that $q_1(t)$ is increasing to define an orientation. For each point on the $\mathbf{z}_2 = (q_2, p_2) \in \Sigma_h$ section, the value of the remaining coordinate on the energy surface, p_1, is found by solving $H(0, p_1, q_2, p_2) = h$. The corresponding Poincaré map is defined by following the flow on $\mathcal{E}_h$ of a point $\mathbf{z}_2$ on the PSS until it returns to Σ_h. However, this map is undefined at points for which the forward trajectory does not return to the surface. In this case, we say that the Hamiltonian is *open*, and the trajectory has *escaped*.

In order to find a unique p_1 for a given energy h, the same root of $H(0, p_1, q_2, p_2) = h$ must be chosen for each initial condition. This is achieved by transforming the

relationship $H(0, p_1, q_2, p_2) = h$ into a fourth-degree polynomial in p_1^2 and using a polynomial root solver to find all solutions and consistently choosing the smallest positive root. This gives a unique initial condition of the form $(0, p_1(q_2, p_2, h), q_2, p_2)$.

Figure 6.8 shows the PSS for progressively increasing values of h: $h = 0.01$, $h = 0.125$, $h = 0.18$, and $h = 0.20$. For small values of h, the dynamics look much like that of the three vortex system described in Section 4.2. As h is increased, the topology of the PSS changes, and additional dynamical features become visible, as expected from the KAM theory outlined in Section 2.5. The PSS can be divided into three regions, exactly analogous to the three regions of the three-vortex problem; see Figure 4.2. In the phase-plane of the three-vortex problem, the fixed points in Region II are surrounded by periodic orbits, while the fixed points on the PSS are surrounded by KAM tori corresponding to quasi-periodic walkabout motions enclosing the fixed points. Analogous to Region III of the three-vortex problem, the PSS features KAM tori corresponding to braiding motions, which enclose all five fixed points. In between the KAM tori are resonant island chains; these correspond to solutions for which the ratio of the frequency of the dimer and the frequency of the braiding or walkabout motions is a rational number. The remainder of this section is organized around a sequence of carefully selected images from our extensive numerical study of this problem that best demonstrates these changes in the phase-space dynamics and provides a catalog of the key structures in phase-space.

6.2.1 The PSS for $h = 0.01$

For $h = 0.01$, the PSS shown in Figure 6.8(a) is remarkably similar to the phase plane of the three-vortex problem shown in Figure 4.2. This is because (4.13) demands that if h is small and $q_1 = 0$ then p_1 must small as well so that q_2 and p_2 approximately satisfy the three-vortex equations of motion. Periodic orbits of the continuous-time system correspond to fixed points, or periodic orbits of discrete period N, of the

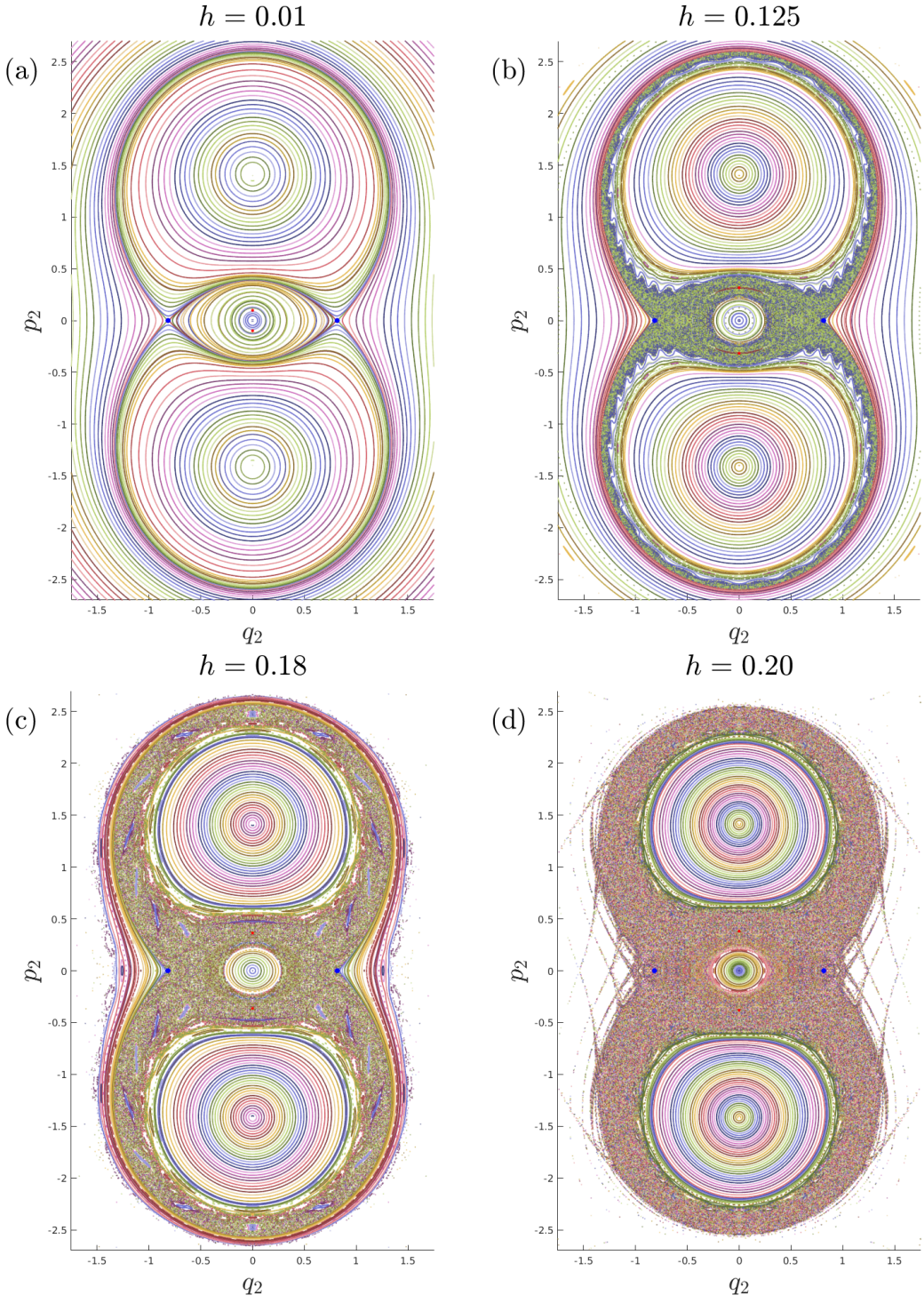

Figure 6.8 PSS for increasing values of h. Note the similarities to the phase-plane of the three-vortex system, see Figure 4.2.

Poincaré map of first return defined by the surface of section. Thus the leapfrogging orbits correspond to fixed points of the Poincaré map. These are located on the p_2-axis and marked with red dots. The leapfrogging orbits correspond to two distinct fixed points because Hamiltonian (4.13) is invariant under the re-labeling of like-signed vortices. As $h \to 0$, these two fixed points converge to the origin, corresponding to the limiting case of a pair of vortices of magnitude 2 moving along parallel lines. The fixed points representing the continuation of the rigidly translating triangles (RTT) of the three-vortex system are marked with blue dots, and we denote the left and right fixed points as RTT_L and RTT_R, respectively.

6.2.2 The PSS for $h = 0.08$

Next, we consider the interior region at $h = 0.08$. A closeup of Region I is shown in Figure 6.9. At this value of h, the interior separatrix has split, leading to heteroclinic tangles near the fixed points RTT_L and RTT_R. This splitting can be inferred from the existence of stochastic regions near the fixed points confined to Regions I and II. This splitting can be seen explicitly by computing the invariant manifolds of these points. The stable (blue) and unstable (red) manifolds of the fixed points have been computed to complement this figure, see Section 6.3 for details.

As can be seen Figure 6.9, the fixed point representing the leapfrogging orbit **(V)** sits on the p_2-axis along with other higher-period leapfrogging orbits including the period-two fixed point which is a two-to-one mixed period leapfrogging orbit, labelled **(VI)**, and the period-three fixed point which is a three-to-one mixed period leapfrogging orbit, labelled **(VII)**, as shown previously in Figure 6.3 and 6.4. The KAM tori surrounding these periodic points indicate that they are stable at this energy level. The tori in the central region around the origin, labelled **(VII)**, depict walkabout orbits in which the negative-signed pairs are closely bound into a dimer. In this region, the assumption that $\mathbf{r}_+$ remains small fails to hold, so that the coupling

term H_2 in the Hamiltonian (4.13) cannot be assumed small and the dynamics are not close to those of the -1:-1:2 system of three vortices.

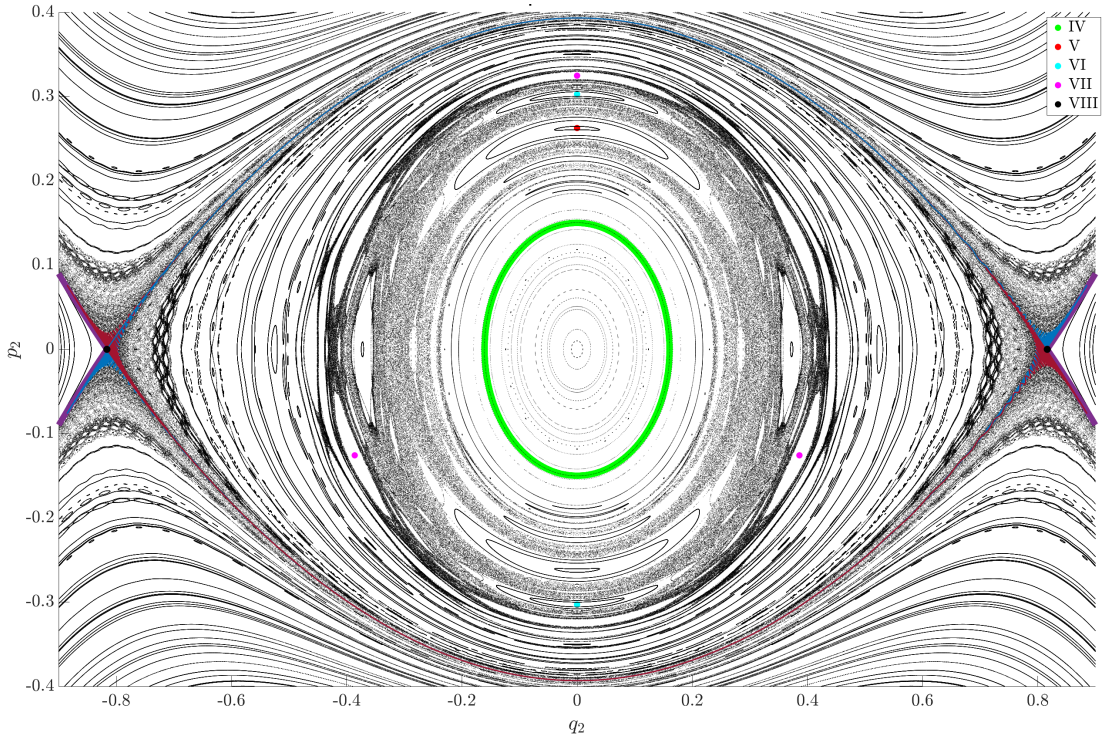

Figure 6.9 The PSS of the central region for $h = 0.08$ where **(IV)** is a walkabout with two negative vortices together, **(V)** is the leapfrogging orbit, **(VI)** is a period 2 fixed point. **(VII)** is period three fixed point, **(VIII)** are RTT_L and RTT_R. Stable and unstable manifolds are shown in blue and red, respectively, while heteroclinic orbits are shown in purple.

6.2.3 The PSS for $h = 0.125$

For $h = 0.125$, Figure 6.8(b) shows a large stochastic region between Region I and Region II. Figure 6.10(a) shows the invariant manifolds of the RTT orbits superimposed on the Poincaré section. Here we can observe this stochastic region corresponds to the continued splitting of the interior separatrix. However, we also observe that the exterior separatrix dividing Regions II and III, marked in purple, remains intact. Many tori which are present at $h = 0.08$ in Figure 6.9 surrounding the mixed-period leapfrogging orbits have broken up at $h = 0.125$, but the KAM tori

surrounding the leapfrogging orbit remain. The presence of these tori prevents points in a neighborhood of leapfrogging orbit from moving into the larger stochastic region. Figure 6.10(c) shows the LD plot of the same section. This gives a global view of the manifolds and can be calculated without detailed knowledge of the fixed points.

6.2.4 The PSS for $h = 0.18$

At $h = 0.18$, shown Figure 6.8(c), unlike at the previously discussed lower energies, there are visible island chains in Region III corresponding to resonant braiding orbits. Additionally, there are no KAM tori surrounding the leapfrogging orbit. Zooming into the fixed point RTT_R, we observe that the exterior separatrix has split, as shown in Figure 6.11. Because the exterior separatrix has split, points in the stochastic sea can enter into braiding orbits in Region III, allowing for the perturbed leapfrogging trajectories to enter into braiding motions, as seen in Figures 6.1(b) and 6.7(b). However, because of the existence of KAM tori in Region III, no orbits in the interior region can escape to infinity.

6.2.5 The PSS for $h = 0.20$

The KAM tori in Region III, corresponding to quasi-periodic braiding orbits, break up between the values $h = 0.18$ and $h = 0.20$ as seen by comparing Figures 6.8(c) and (d). At $h = 0.20$, no tori remain in Region III, and there is no barrier to escape for trajectories from Regions I and II. We investigate the breakup of these tori in more detail in Chapter 7 where we discuss the mechanisms for escape.

Figure 6.10(b), shows the invariant manifolds of the RTT points, clearly demonstrating their splitting. However, directly computing long portions of invariant manifolds is numerically very difficult, and this method does not allow us to visualize the full extent of the invariant manifolds. The plot of the Lagrangian descriptors in Figure 6.10(b) demonstrates the location and of these manifolds much more clearly.

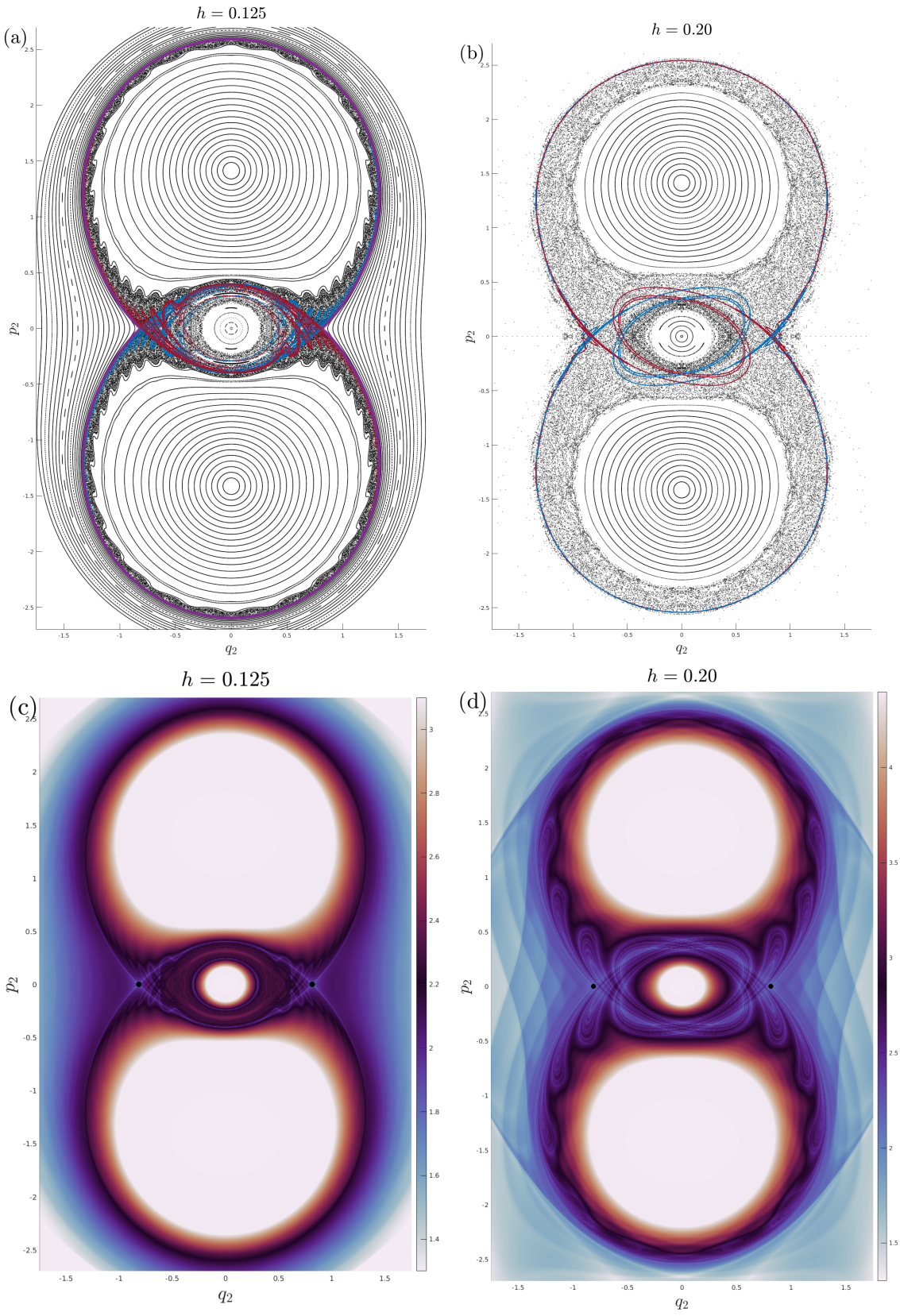

Figure 6.10 PSS and LD for $h = 0.125$ and $h = 0.20$. The stable and unstable manifolds of both RTT_L and RTT_R are colored in blue and red, respectively.

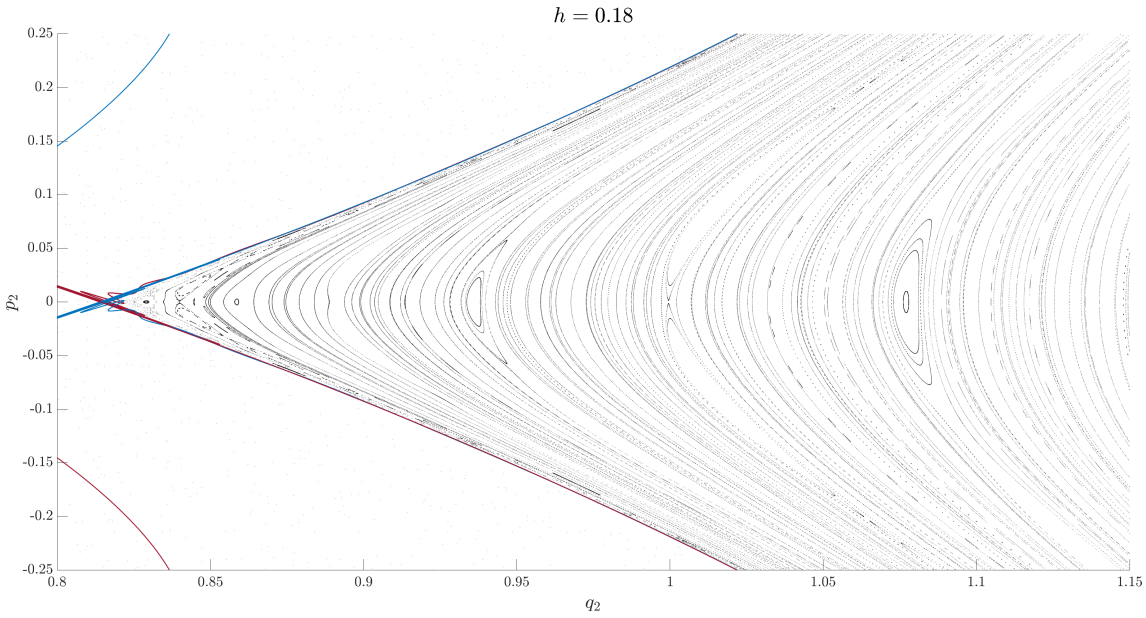

Figure 6.11 Closeup showing the small separatrix splitting of the exterior separatrix at RTT_R for $h = 0.18$.

We can now see the manifolds winding along the edge of Region II inside the stochastic sea. We can also see the invariant manifolds that extend throughout the escape regions outside the KAM tori in Regions III. As we do not even know what these are invariant manifolds *of*, they could not be computed using a direct approach.

We conclude by noting that there is only a narrow regime of energies in which the splitting of the exterior separatrices and KAM tori in Region III simultaneously exist. Because both of these features are necessary for perturbed leapfrogging orbits to be able to transition to braiding, this explains why braids are rare and mostly overlooked in previous studies.

6.3 A Remark on Numerics Used in This Chapter

The calculations in Section 6.2 and Chapter 7 rely heavily on numerical integration of the Hamiltonian system. All numerical integration was done using the Julia package `DifferentialEquations.jl` [49]. Using forward mode automatic differentiation (AD), via the `ForwardDiff.jl` [50] package, only the Hamiltonian needs to be

specified. The canonical equations of motion (2.2) are found by computing the appropriate partial derivatives using AD. This approach, amazingly, leads to less round-off error than the numerical evaluation of the complicated explicit expressions for the equations of motion. For all numerics, as a consistency check, the change of energy over the trajectory was computed and confirmed to be on the same order of magnitude as expected by the prescribed tolerances.

The Lagrangian descriptors were evaluated in parallel on 128 threads with 36 million initial conditions using an equally spaced grid of $6,000 \times 6,000$ points. The ODEs were solved using the Tsit5 algorithm (a 5th order Runge-Kutta method [57] due to Tsitouras) with relative and absolute tolerances of 10^{-6} and 10^{-9}. For creating the initial primary segment of the invariant manifolds, double precision arithmetic was used to find the Jacobian of the numerically defined Poincaré map. The invariant manifolds were computed using a custom Julia implementation of the ALI+ algorithm described by Goodman and Wróbel [26] with a curvature threshold of $\alpha = 10^{-4}$. The primary segment was numerically integrated using the Vern9 (a 9th order Runge-Kutta algorithm [58] due to Verner) with tolerances of 10^{-14} and 10^{-17} using double-precision arithmetic.

CHAPTER 7

NONLINEAR TRANSITIONS

In Chapter 6, we discussed the fundamental motions of the vortex quartet and described their location in phase space. In the current chapter, we focus on the role the phase space structure plays in the transitions of the quartet's dynamics. Ultimately, we would like to use this to understand the nature of escape. Acheson [2] identified two distinct types of escape, walkabout-to-disintegration, and immediate disintegration. In both cases, the vortices must escape as two opposite-signed pairs that escape to infinity along transverse rays. We observe a third type of escape—'diffusive-escape'—in which the walkabout orbits disintegrate only over a very long time scale due to overlapping resonance zones in Region III. By utilizing the tools from the geometric theory of dynamical system, we can understand the nature of these transitions to escape. The system undergoes six key transitions as h increases. Sequentially, they are:

I. The breakdown of the KAM tori surrounding the leapfrogging orbit.

II. The crossing of the interior separatrices connecting RTT_L and RTT_R with the invariant manifolds of the leapfrogging orbit.

III. The splitting of the exterior separatrix between Regions II and III.

IV. The breakdown of the KAM tori between the island chains in Region III. This allows *diffusive escape*.

V. The disappearance of the island chains in Region III. This allows *walkabout-to-disintegration*.

VI. The intersection of the invariant manifolds of the leapfrogging orbit with the escape regions. This allows *immediate disintegration*.

7.1 Escape Times

To get a bird's eye view of the quantitative behavior of escape as h is varied, consider a perturbed initial condition of the periodic leapfrogging orbit. On a level set of the Hamiltonian $H = h$, the leapfrogging orbit on the PSS using the cross-section $q_1 = 0$ is given by the initial condition

$$\mathbf{z}_h^{\mathrm{lf}}(0) = \left(0, p_1\left(0, \sqrt{\frac{h}{2h+1}}\right), 0, \sqrt{\frac{h}{2h+1}}\right).$$

where $p_1(q_2, p_2)$ is determined by the energy surface condition, $H(0, p_1, q_2, p_2) = h$. We consider a family of perturbed leapfrogging orbits with initial conditions given, for example, by the formula

$$\mathbf{z}_h^{\mathrm{pert}}(0) = \left(0, p_1\left(10^{-6}, \sqrt{\frac{h}{2h+1}}\right), 10^{-6}, \sqrt{\frac{h}{2h+1}}\right),$$

and plotting their escape times in Figure 7.1. This plot provides hints as to which values of phase space to examine, but in itself does not provide a complete picture as it only demonstrates the behavior of a one-parameter family of perturbations as h varies. We set a maximum numerical integration time of $T_{\max} = 10^6$. In this figure we annotate two values noted by Tophøj and Aref, $h \approx 0.216$ and $h \approx 0.26$. The first represents the values where they began to observe perturbed leapfrogging orbits that first transitioned into walkabout motion before escaping and the latter where they saw a disintegration. These escape values were found by running simulations for a variety of initial conditions and observing the behavior. Figure 7.1 provides a refinement of that picture. It appears that escapes begin at a smaller value energy level than the value given by Aref, around $h = 0.194$, marked in the plot, although they may not have been considering such long integration times. In Figure 7.1, observe that escape time is not a smooth function of the energy level. We observe spikes where the escape time appears to diverge. This behavior has a natural explanation that is discussed in Section 7.7.

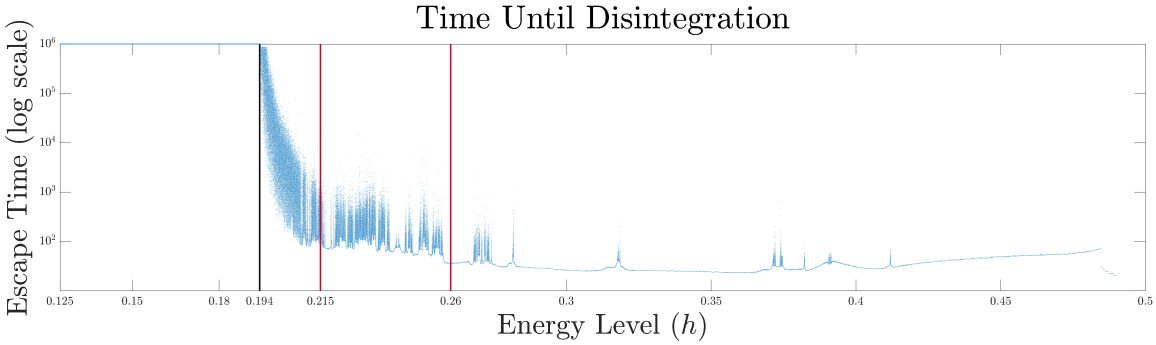

Figure 7.1 Time to escape for typical trajectory in a neighborhood of the leapfrogging orbit.

7.2 Transition I: Connection of Leapfrogging orbit to Region 1

In Chapter 5, we demonstrated that the leapfrogging orbit is stable for $h < h_c = \frac{1}{8}$. As discussed in Section 2.6.5, it is the disappearance of the last KAM tori surrounding the two new stable fixed points created by the pitchfork bifurcation that allows for the leapfrogging motion to transition from an aperiodic leapfrogging into walkabout motions. Figure 7.2, shows invariant manifolds of RTT_L and RTT_R at $h = 0.129 > h_c$, and also the invariant manifolds of the unstable leapfrogging orbit.

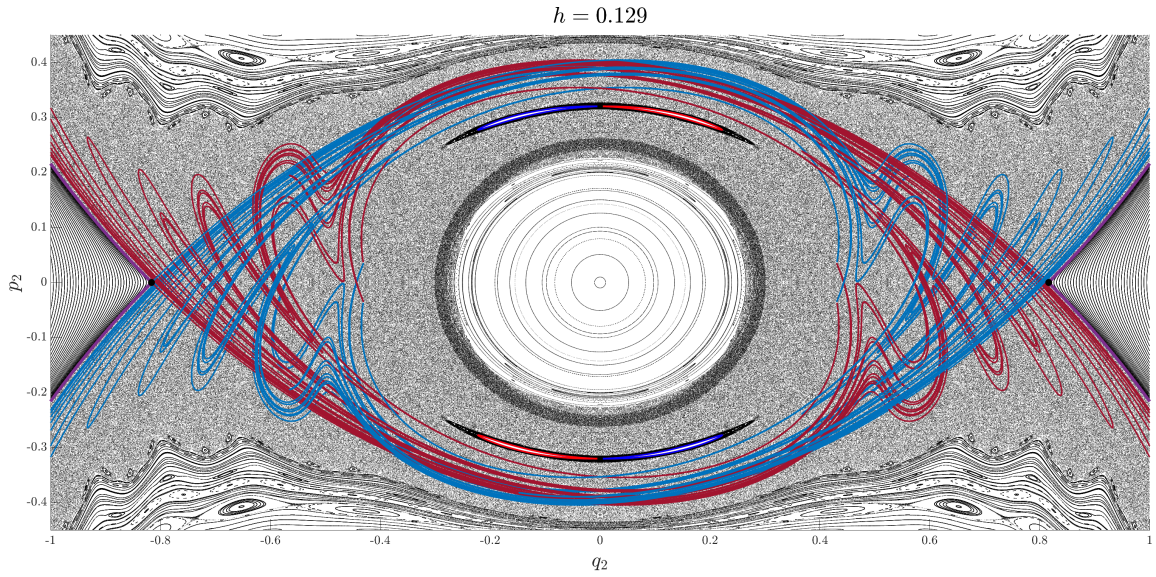

Figure 7.2 The PSS for $h = 0.129$. The stable and unstable manifolds are drawn in blue and red, respectively. Heteroclinic orbits are drawn in purple.

Zooming in closer in Figure 7.3, we can clearly see KAM tori enclosing the invariant manifolds of the unstable leapfrogging orbit. In Figure 7.4 we provide a

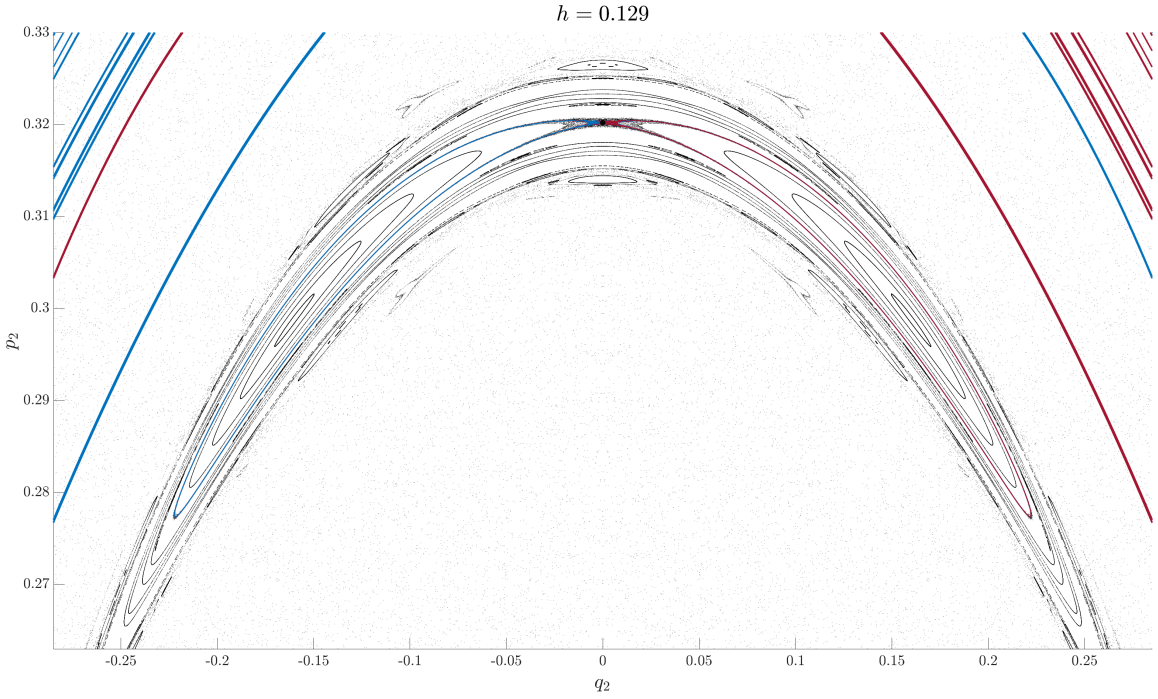

Figure 7.3 Zoomed in image of Figure 7.2 near the leapfrogging orbit. Observe the KAM tori surrounding the invariant manifolds of the fixed point.

closer look at the homoclinic tangle. This tangle is the 'trellis' or 'web' that was infamously imagined, but not drawn, by Poincaré. Figure 7.5 shows the central region at slightly larger energy $h = 0.135$. At first appearance, this looks the same as for $h = 0.129$; however, on closer inspection, we see that no tori surrounding the leapfrogging fixed point remain, as can be seen in the closeup shown in Figure 7.6.

7.3 Transition II: Connection of Leapfrogging orbit to Region 2

At $h = 0.145$, the unstable manifold of the leapfrogging orbit intersects the unstable manifold of RTT_R. Figure 7.7, shows just these two invariant manifolds, along with the intact exterior separatrix, leaving out some of the others in order to reduce clutter and demonstrate the intersection cleanly. For larger values of h, we no longer are concerned about the invariant manifolds of the leapfrogging orbit, as we already

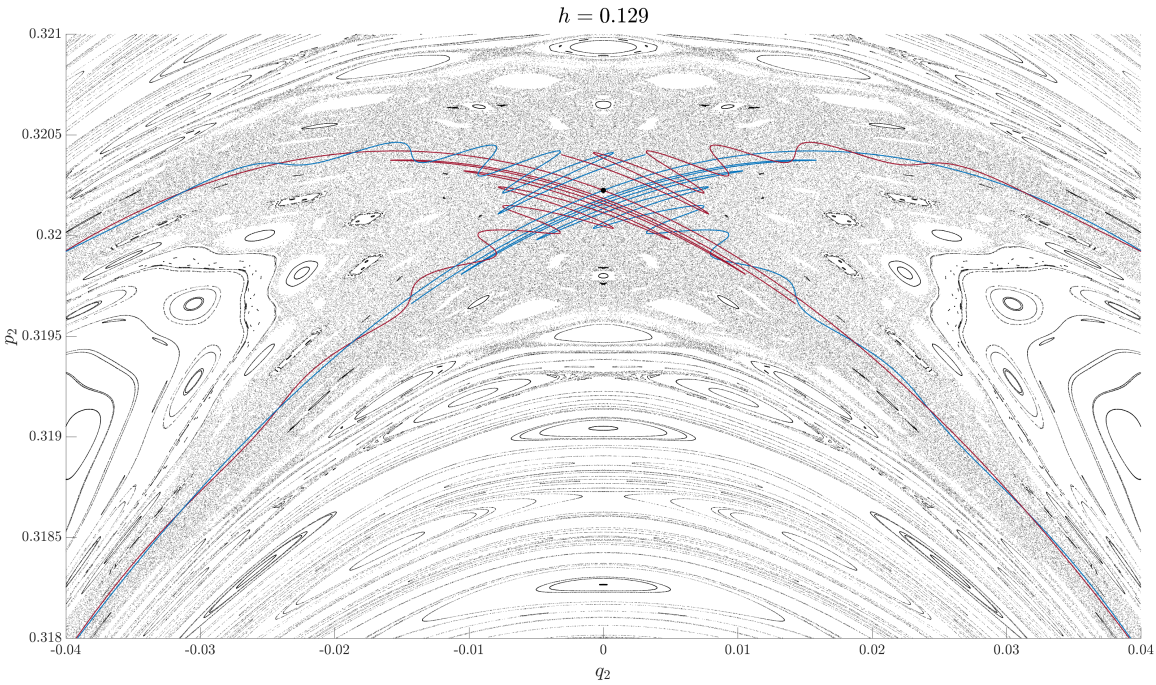

Figure 7.4 Zoomed in picture of Figure 7.3 to show the homoclinic tangle at the fixed point.

know that it will intersect the invariant manifolds of RTT_L and RTT_R. Thus for the subsequent transitions, we show only the invariant manifolds of RTT_L and RTT_R.

7.4 Transition III: Splitting of the Exterior Separatrix

As explained is in Section 6.2, at $h = 0.18$ the exterior separatrix has split. In particular, the plot at $h = 0.18$ in Figure 6.11 shows that KAM tori constrain the tangles on the interior of the island chains. It is now possible for points inside the stochastic sea to reach the island chains. This breakup leads to perturbed leapfrogging orbit to temporarily transition into quasi-periodic braiding motions.

7.5 Transition IV: Diffusive Escape

As discussed in Section 6.2, the exterior separatrix begins to split at around $h = 0.18$. At this energy level, we begin to observe braids in the chaotic trajectories of motions starting in a neighborhood of the leapfrogging orbit, such as in Figure 1.4(b) as they

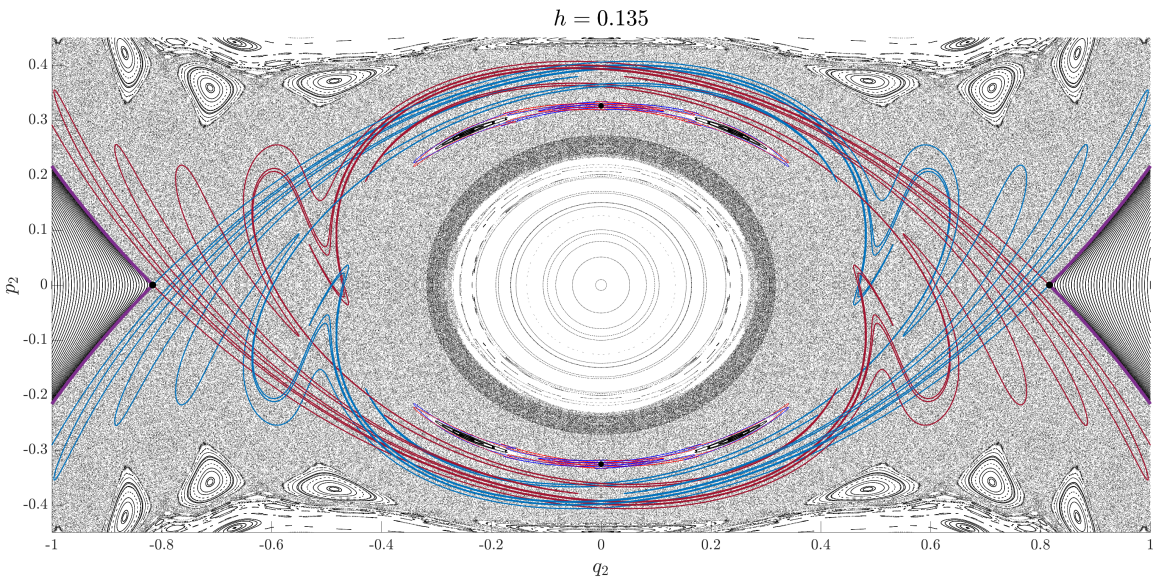

Figure 7.5 The PSS for $h = 0.135$. The stable and unstable manifolds are drawn in blue and red, respectively. Heteroclinic orbits are drawn in purple.

escape from the chaotic sea into island chains in Region III. However, as long as there are KAM tori enclosing Region III, the trajectories must remain bounded.

In Section 6.2, we observe that the KAM tori in Region III break up between $h = 0.18$ and $h = 0.20$. We now provide a refinement of that observation. Figure 7.8 shows a closeup of the PSS in a neighborhood of RTT_R for three values of h. We note that as $h \to 0.194^+$, the last tori breaks down. This observation is in line with the escape time plot in Figure 7.1. The breakdown of these island chains is due to the overlap of the separatrices surrounding the resonant fixed points in the island chain. Figure 7.9 shows a set of discrete-Time LD computations in a neighborhood of RTT_R with increasing values of h. These image demonstrate the gradual increase in the resonance overlap as h increases from $h = 0.188$ to $h = 0.195$. In the first image, the invariant manifolds are very simple and do not overlap, while in the last, we see quite complicated overlapping tangles. The trajectory of a point inside the island chain can now move through the resonances, ostensibly at random. This seemingly random motion causes a diffusive drift from resonance to resonance. However, because

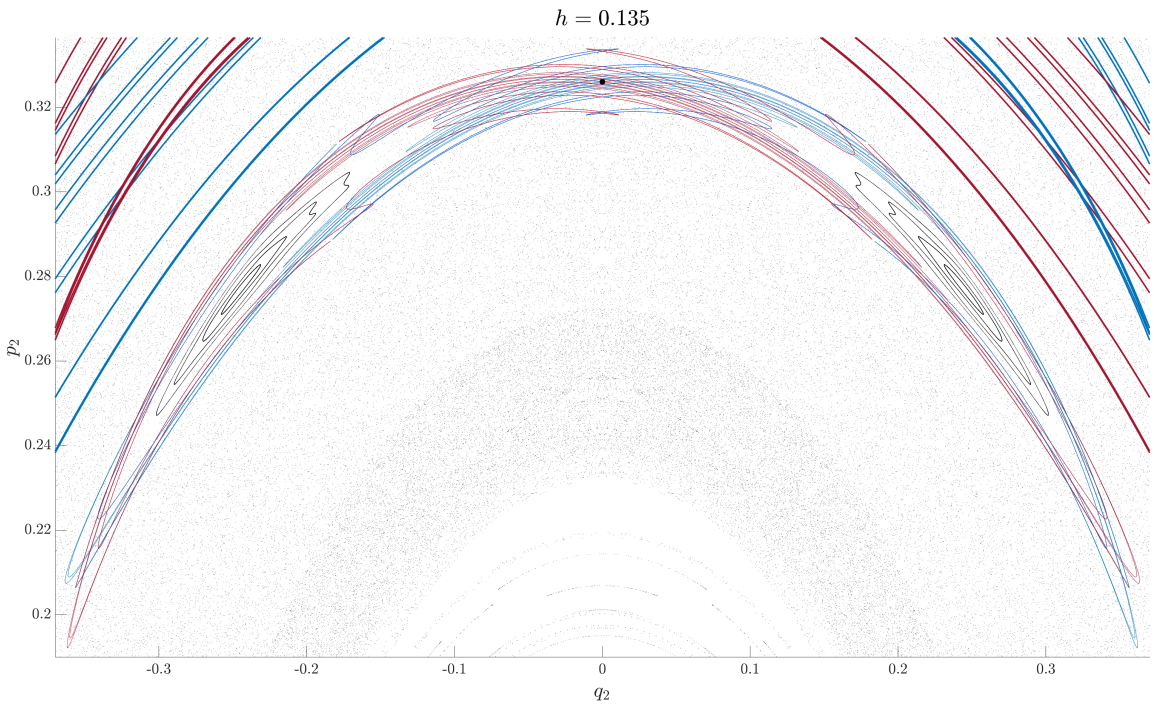

Figure 7.6 Zoomed in image of Figure 7.5 near the leapfrogging orbit. Observe that there are *no* KAM tori surrounding the fixed point.

of the island chains' 'stickiness,' this process is slow, but it becomes faster as the overlaps of resonances grow. This is consistent with the escape-time plot in Figure 7.1. The resonance overlap can also be seen using classical invariant manifold and PSS techniques. In Figure 7.10, we have plotted the PSS at the value of $h = 0.191$, which is below the critical value at which the final KAM tori break up. Inside the island chain, unstable periodic points of order k ranging from $k = 9$ to 27. The stable and unstable manifolds of these hyperbolic fixed points of the kth-iterates of the Poincare map are drawn as blue and red curves, respectively. Heteroclinic tangles surround each island chain, but there exist KAM tori in between the island chains so that the tangles are isolated from each other. An analogous plot at a slightly higher level $h = 0.1945$ is shown in Figure 7.11, in which the KAM tori separating the island chains have all split. The resonances now overlap, and the heteroclinic tangles surrounding adjacent island chains of kth-order periodic points intersect, creating a path from Regions I

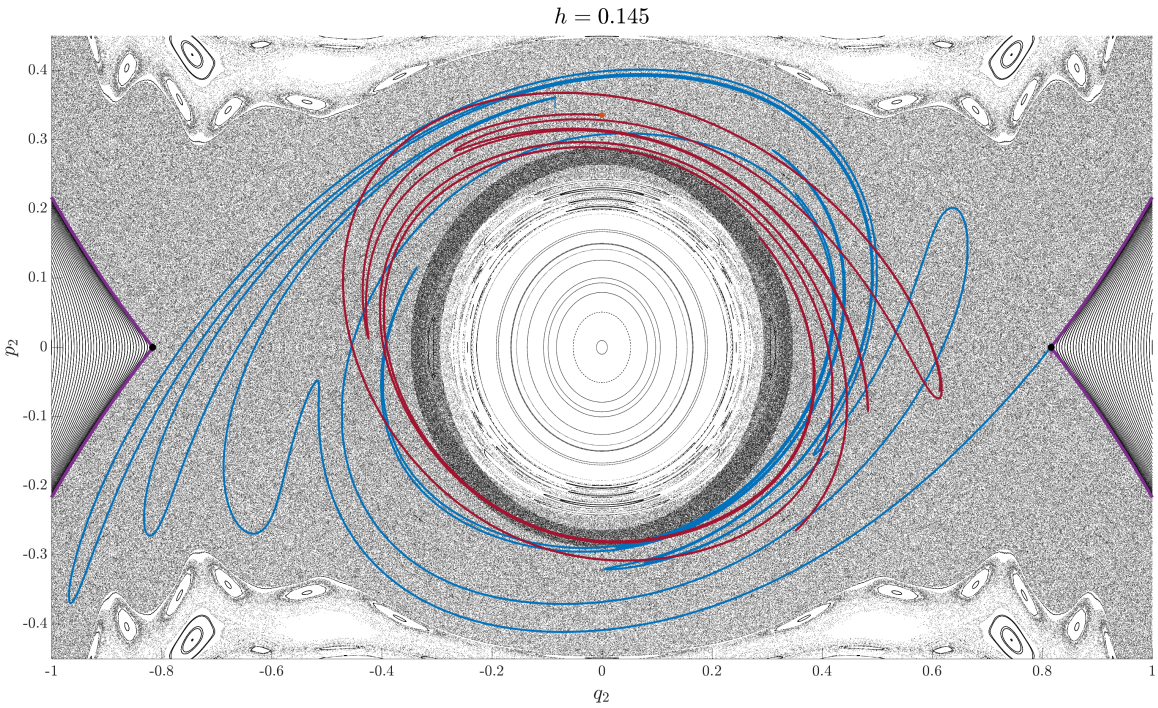

Figure 7.7 The PSS for $h = 0.145$. The stable and unstable manifolds are drawn in blue and red, respectively. Heteroclinic orbits are drawn in purple. Observe that the stable manifold of RTT_R crosses the unstable manifold of the leapfrogging orbit.

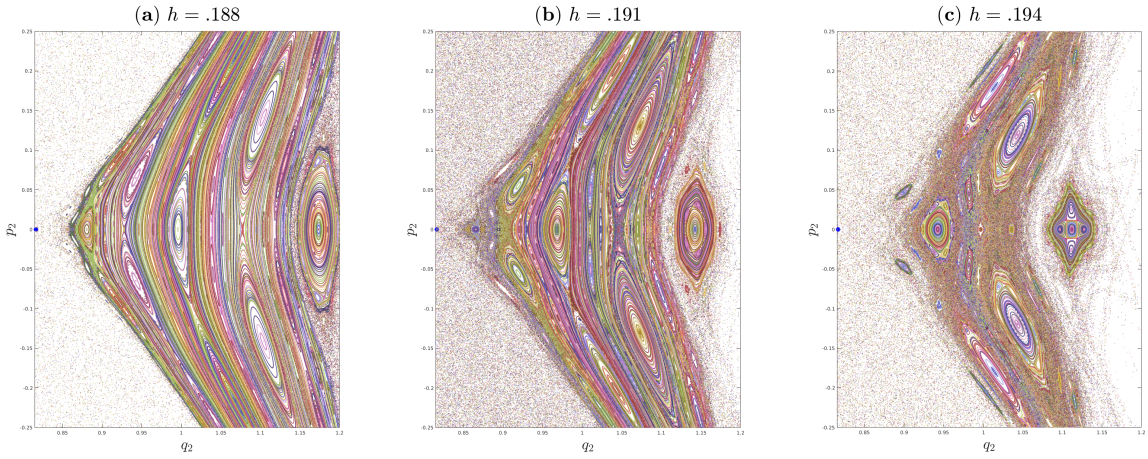

Figure 7.8 Breakdown of the tori in Region III near RTT_R as h approaches 0.194.

and II to the escape region outside the island chain. We note here that Lagrangian descriptors are a powerful exploratory tool—very little prior knowledge of the phase space is needed to build a skeleton depicting all the invariant manifolds on the section. The construction of Figures 7.10 and 7.11 required the tedious and challenging process

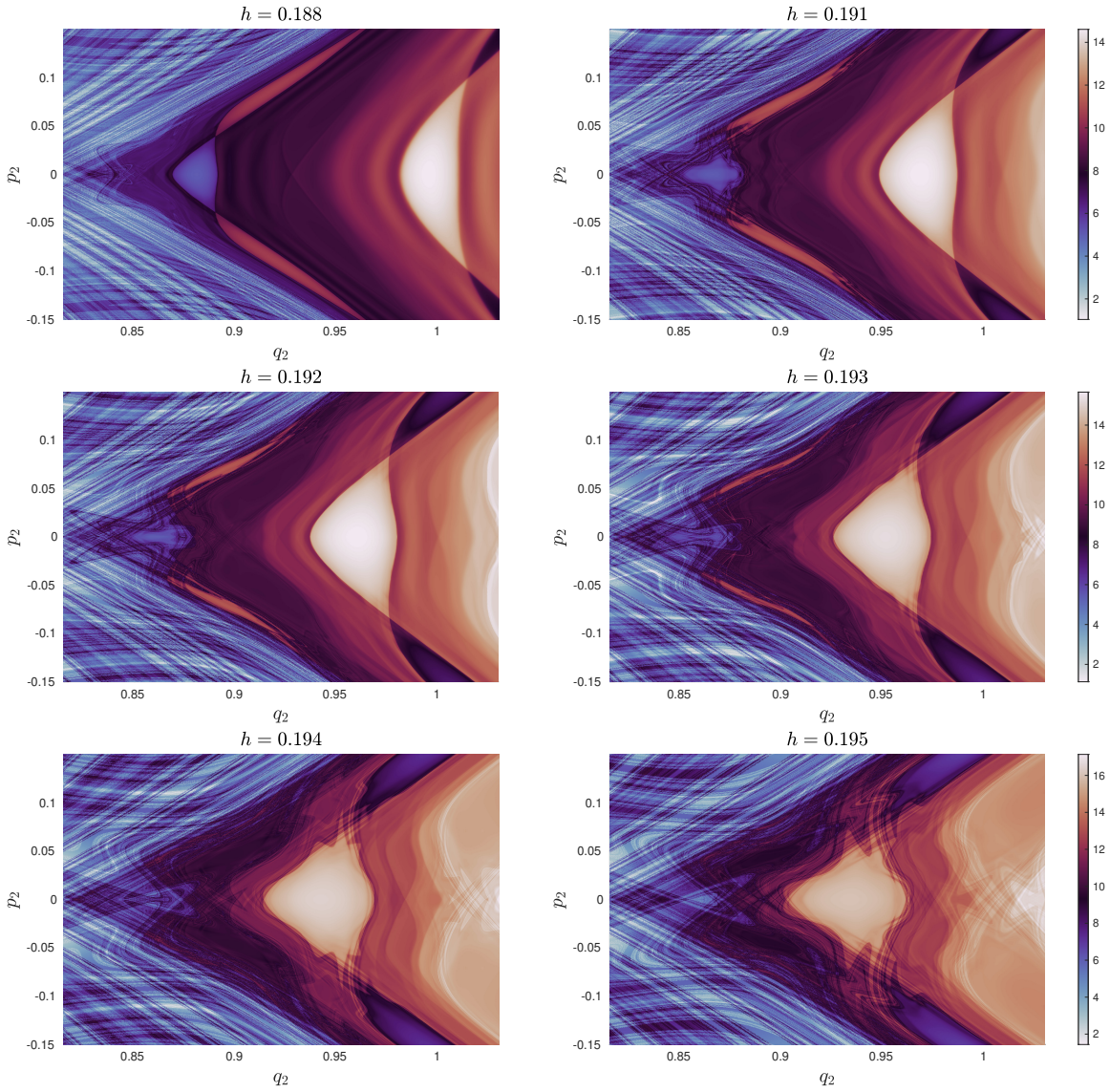

Figure 7.9 The growing resonance overlap of the island chain near RTT_R using discrete-time Lagrangian descriptors. Compare to Figure 7.8.

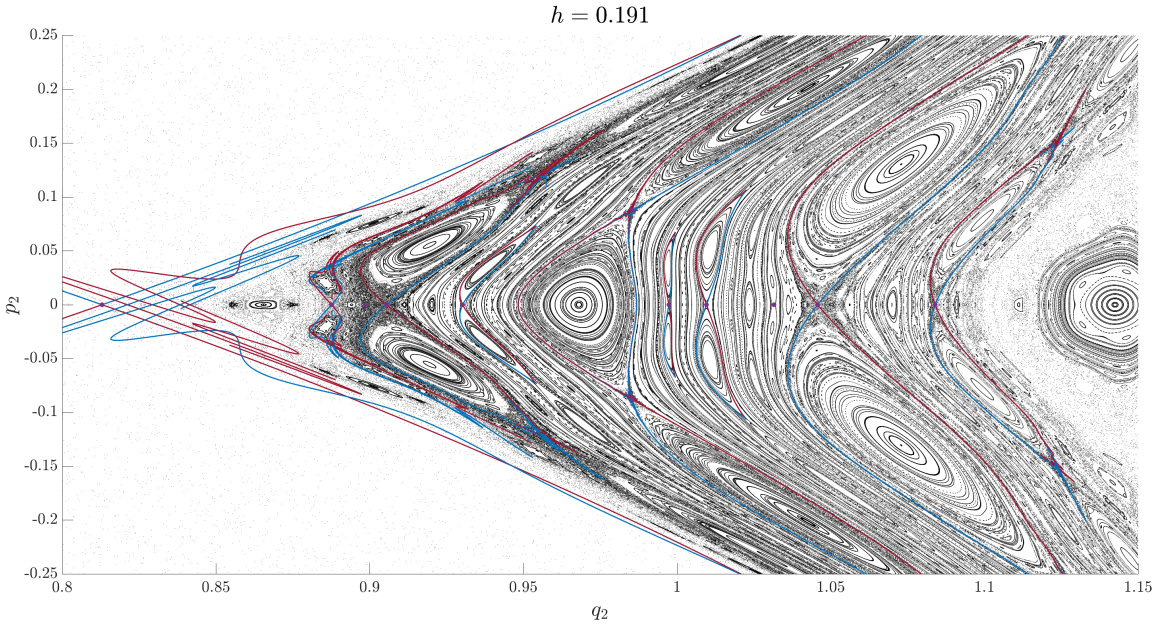

Figure 7.10 For $h < 0.194$, the stable and unstable manifolds of the nested island chain saddles are between within the KAM Tori and do not cross.

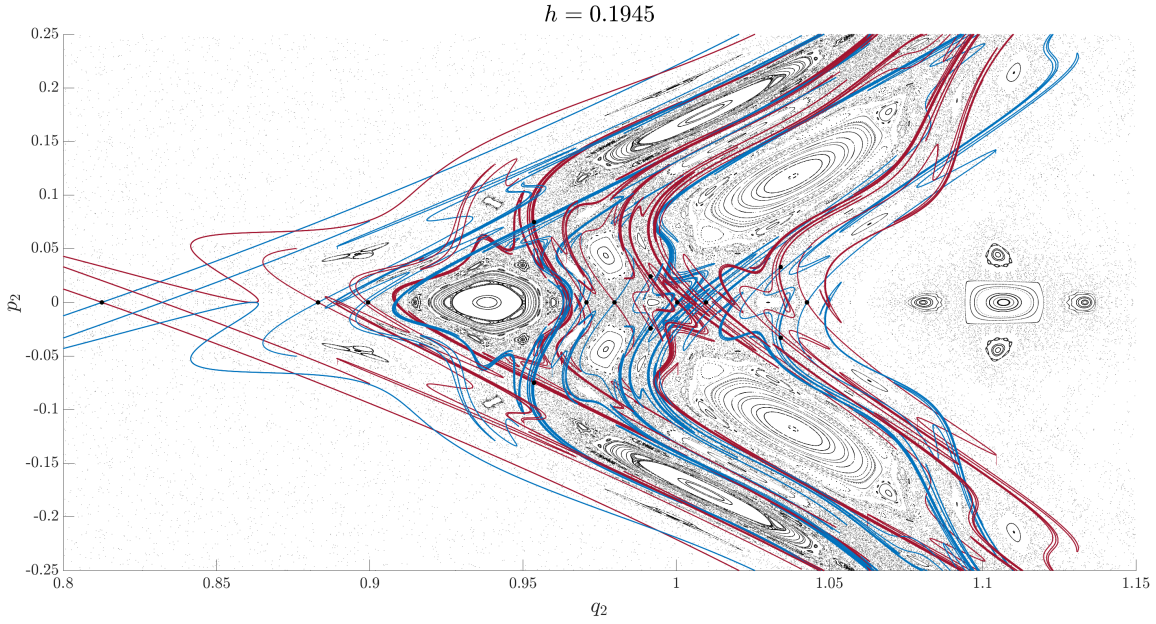

Figure 7.11 For $h > 0.194$, the stable and unstable manifolds of, leading to a mode of escape for trajectories in Regions I and II.

of finding each periodic point *and* its order before we could numerically construct its stable and unstable manifold. Even then, only a handful of points were found. When using Lagrangian descriptors in Figure 7.9 no information is needed about the fixed points' location and order, nor is it necessary to compute the manifolds emanating each fixed point.

7.6 Transition V: Walkabout-to-Disintegration

Neither PSS nor LD plots provide a viewer with immediate information about escaping trajectories. To get a quantitative understanding of the escape regions, we introduce the discrete-time forward escape plot for a set of initial conditions on the PSS. In these images, each initial condition $\mathbf{z}$ on the section is color-coded according to the number of times the trajectory returns to the PSS in forward time before escape.

In this section and the following sections, we present a series of paired images for each of the three values h indicated in Figure 7.1. The first member of each pair uses backward and forward-time Lagrangian descriptors to show the skeleton of invariant manifolds on the surface of section while the second shows the forward-time Lagrangian descriptors to show only the skeleton of the stable manifolds. The third presents the forward time escape structure for initial conditions on the section. In this image, we also present the stable manifolds of the leapfrogging orbit and the unstable manifolds of RTT_L and RTT_R to understand the relationship between the perturbed leapfrogging orbits and the escape regions. In Figure 7.12, we observe the apparent location of invariant manifolds corresponding to the 'tentacles' separating different lobes of the hit map. In Figure 7.13, we show only the stabl manifold structure. However,these do not provide an answer what phase space structures these invariant manifolds emanate from. At $h = 0.194$, as seen in Figure 7.14, all initial conditions

with escape times less than four hits lay outside the invariant manifolds of RTT_L and RTT_R and can only be reached by the diffusion through the broken island chains.

At $h = 0.216$, the picture has changed, see Figure 7.15 and Figure 7.16. At this energy level, the region of island chains is no longer present, and we see in Figure 7.17 that the unstable manifolds of both RTT_L and RTT_R (shown in red) intersect the stable manifolds of the leapfrogging orbit (shown) *and* enter into the immediate escape regions (shown in green). This is the parameter value Acheson and Aref observe walkabout-to-disintegration behavior in laboratory-frame simulations. To complete the picture of how the invariant manifolds change with h, we have included Figure 7.18, showing the PSS and forward-time LD for the immediate values of $h = 0.21$ and $h = .225$.

7.7 Transition VI: Immediate Disintegration

At $h = 0.26$, there is now an immediate escape has grown to encompass a neighborhood of the leapfrogging orbit, see Figures 7.19, 7.20, and 7.21. A generic point in a neighborhood of the leapfrogging fixed points escapes without entering into the region of walkabout motions.

There exist points that do enter into walkabouts or braids, corresponding to the spikes in the escape times seen in Figure 7.1. When the vortices disintegrate, they travel in pairs along transverse rays as they escape to infinity. When these transverse rays become tangent with each other, the vortices again becoming bound, and possibly exchange partners.

This can be understood by zooming in near the leapfrogging orbit in Figure 7.17, see Figure 7.22. Looking at initial conditions near the perturbed leapfrogging trajectory, we observe a generic point is in an immediate escape region. However, this neighborhood also contains a complex structure of higher escape times,

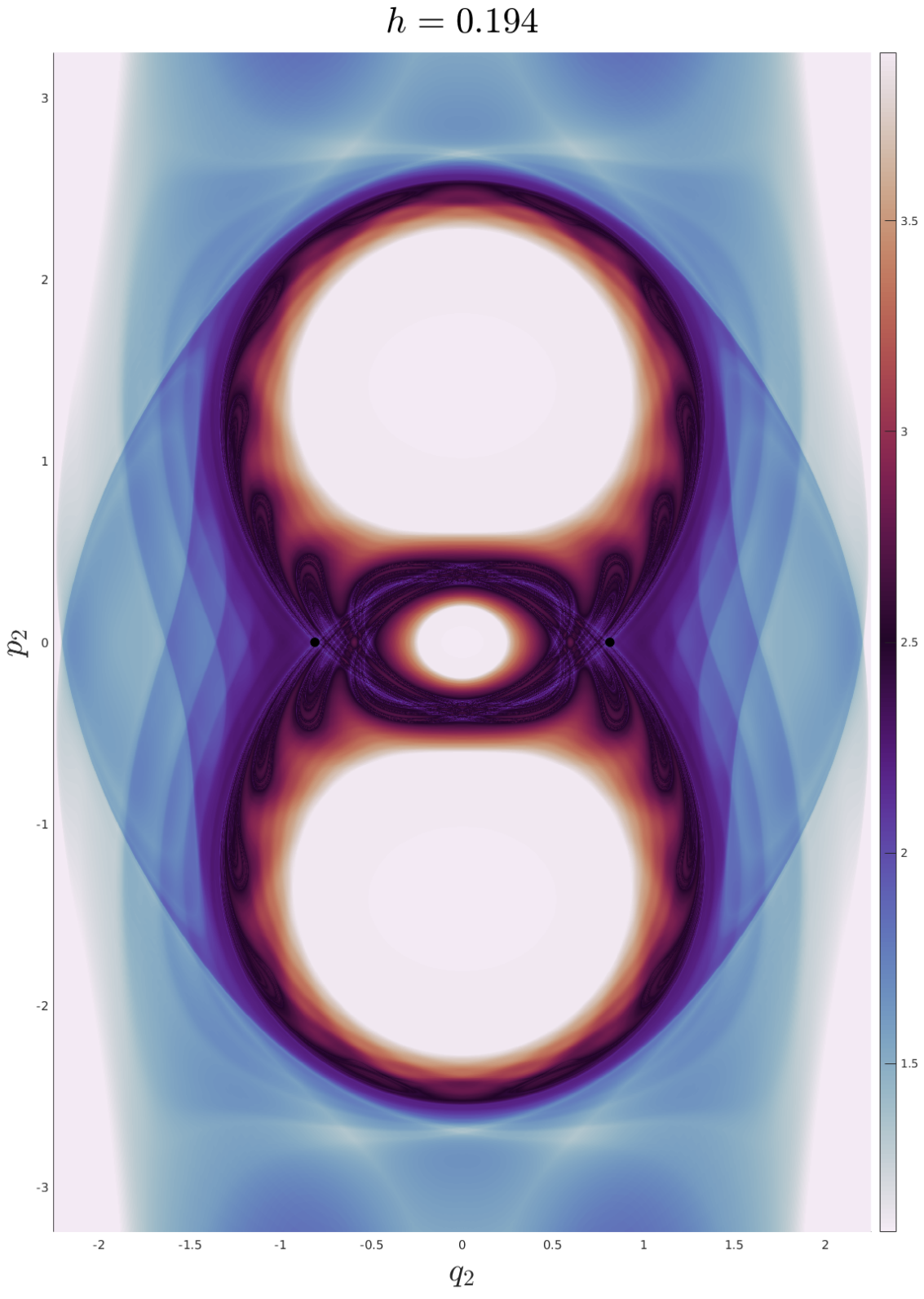

Figure 7.12 LD for $h = 0.194$ showing the skeleton of invariant manifolds.

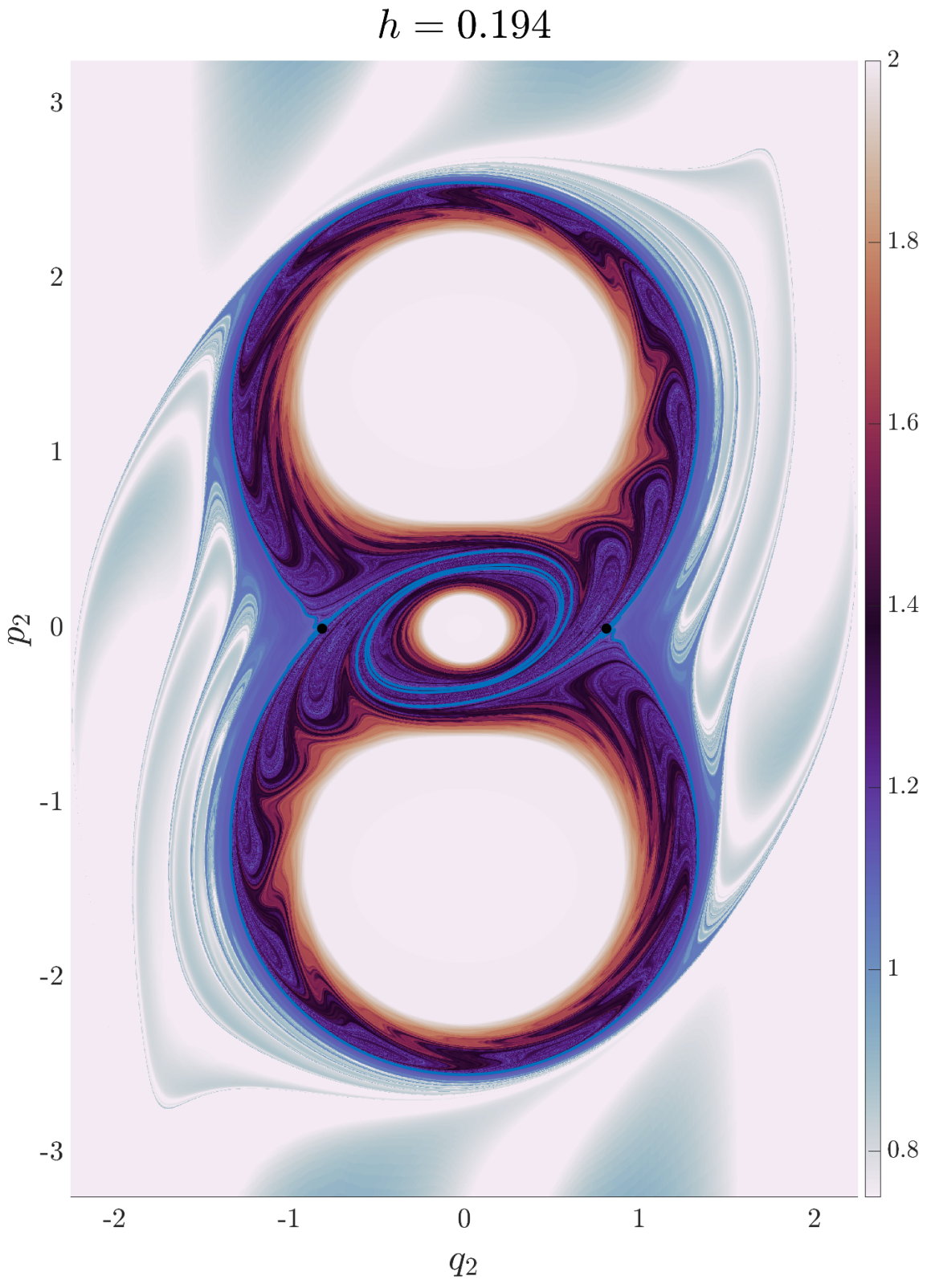

Figure 7.13 Forward-time LD for $h = 0.194$ with the stable manifolds of RTT_L and RTT_R in blue.

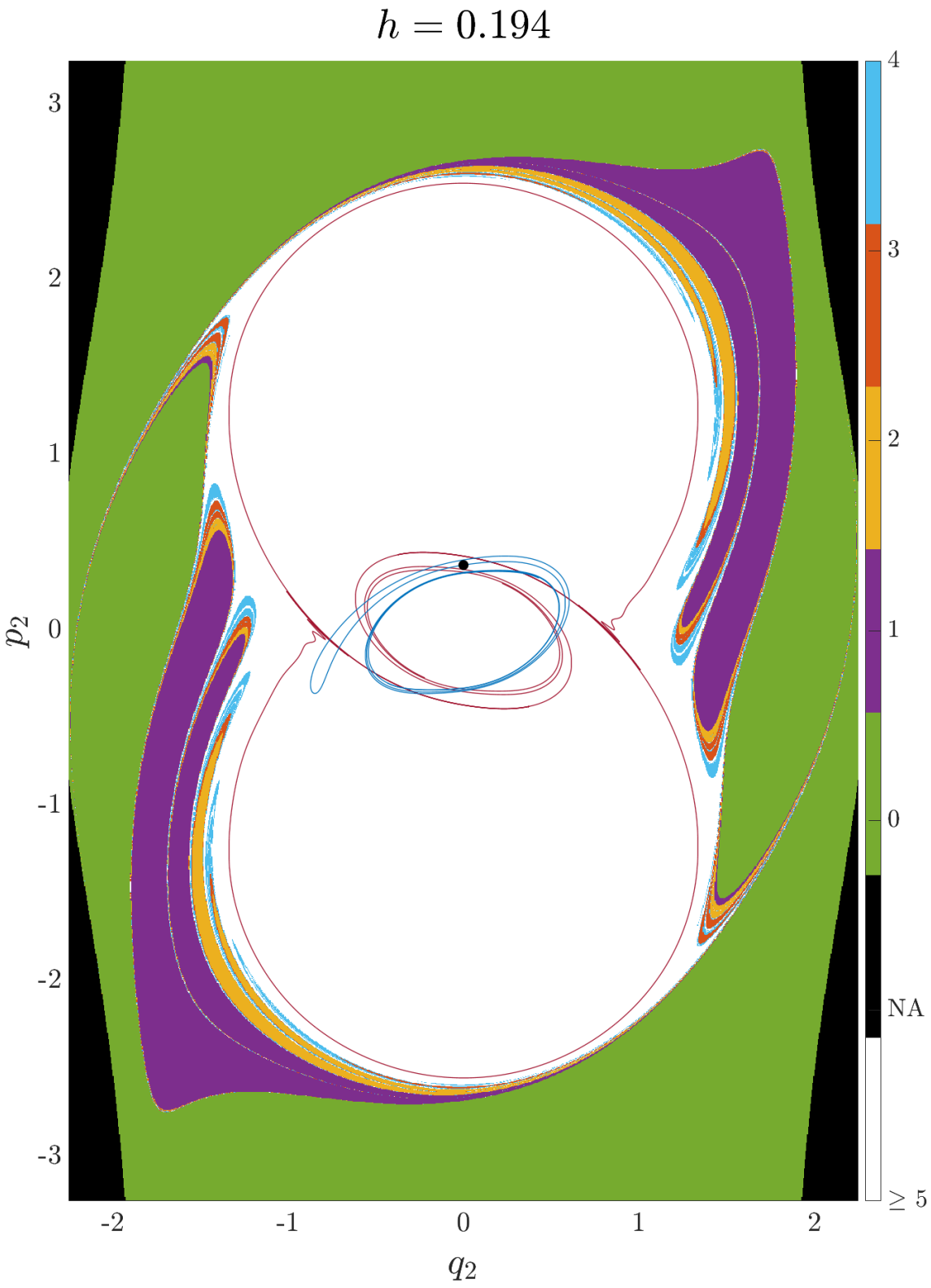

Figure 7.14 The forward time discrete escape plot with the stable manifolds (blue) of the leapfrogging orbit and the unstable manifolds of RTT_L and RTT_R (red) for $h = 0.194$.

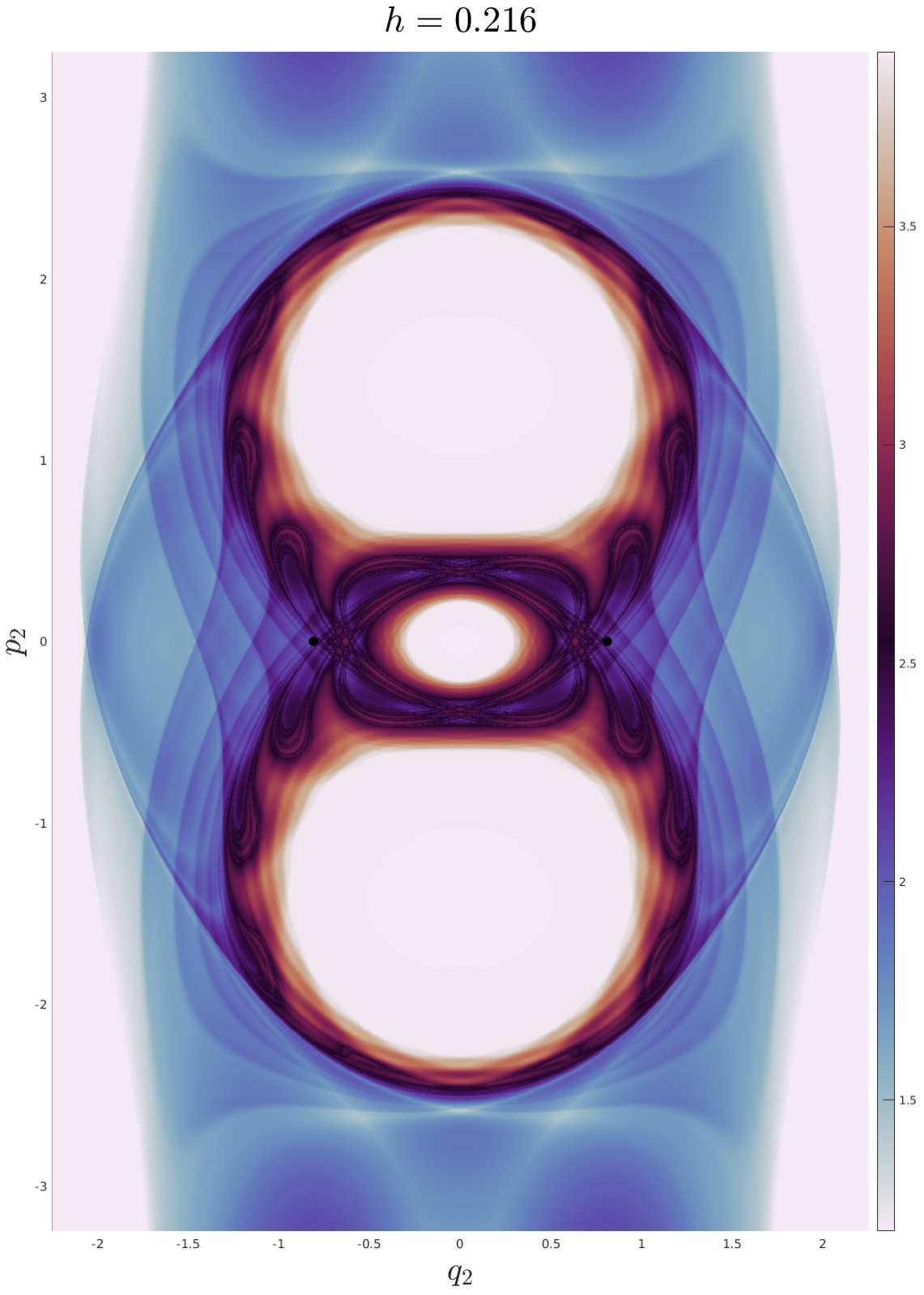

Figure 7.15 LD for $h = 0.216$ showing the skeleton of invariant manifolds.

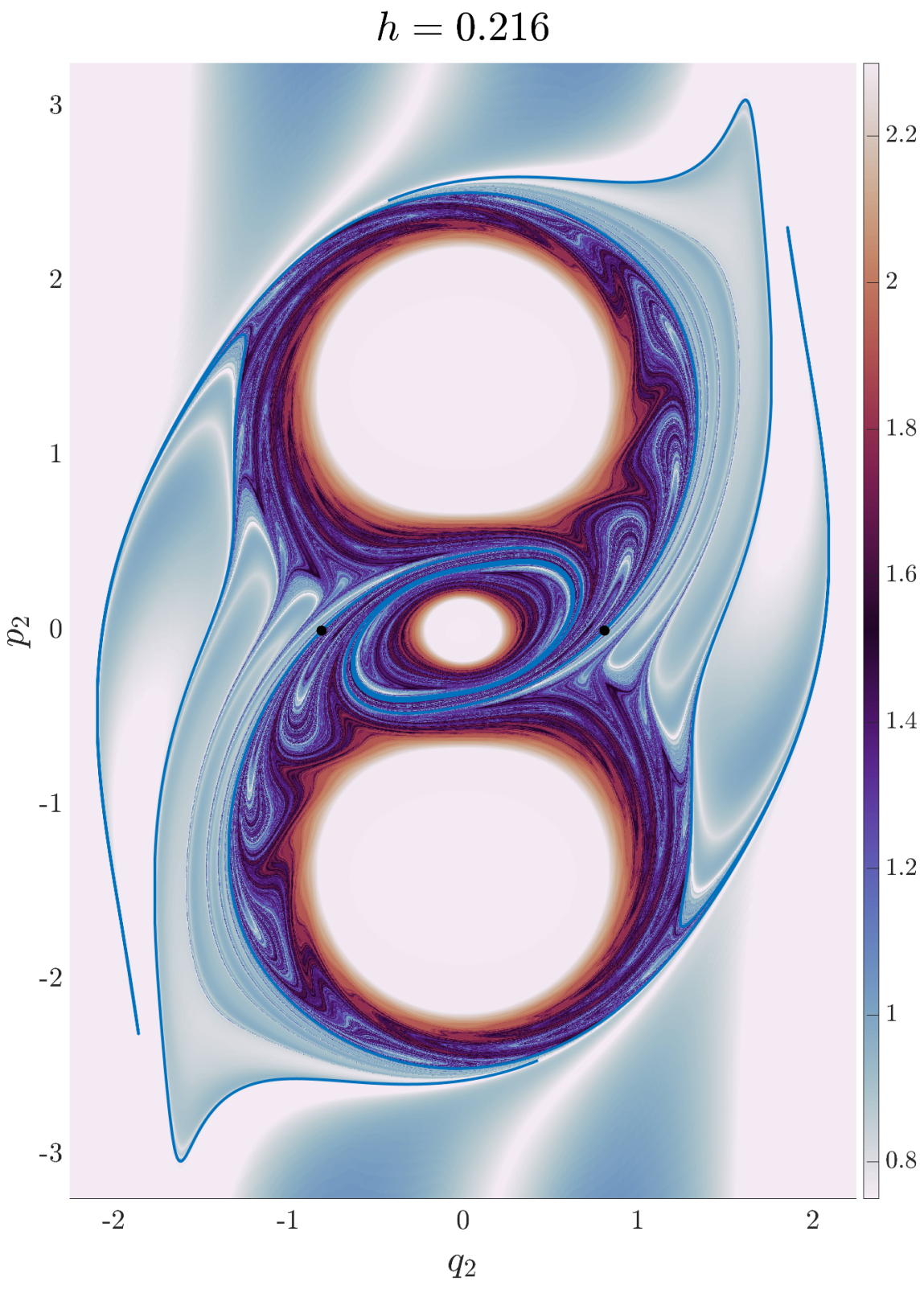

Figure 7.16 Forward-time LD for $h = 0.216$ with the stable manifolds of RTT_L and RTT_R in blue.

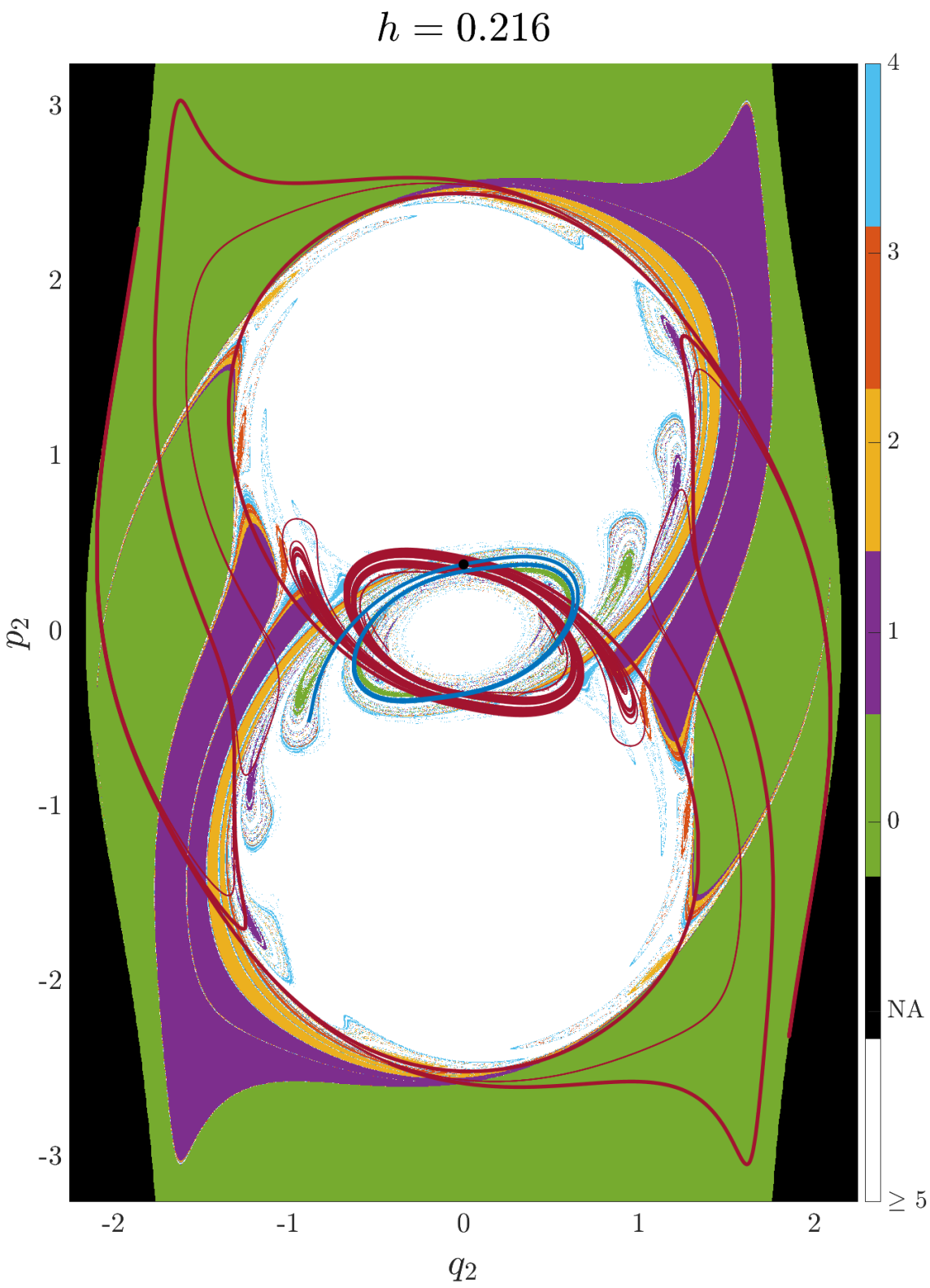

Figure 7.17 The forward time discrete escape plot with the stable manifolds (blue) of the leapfrogging orbit and the unstable manifolds of RTT_L and RTT_R (red) for $h = 0.216$.

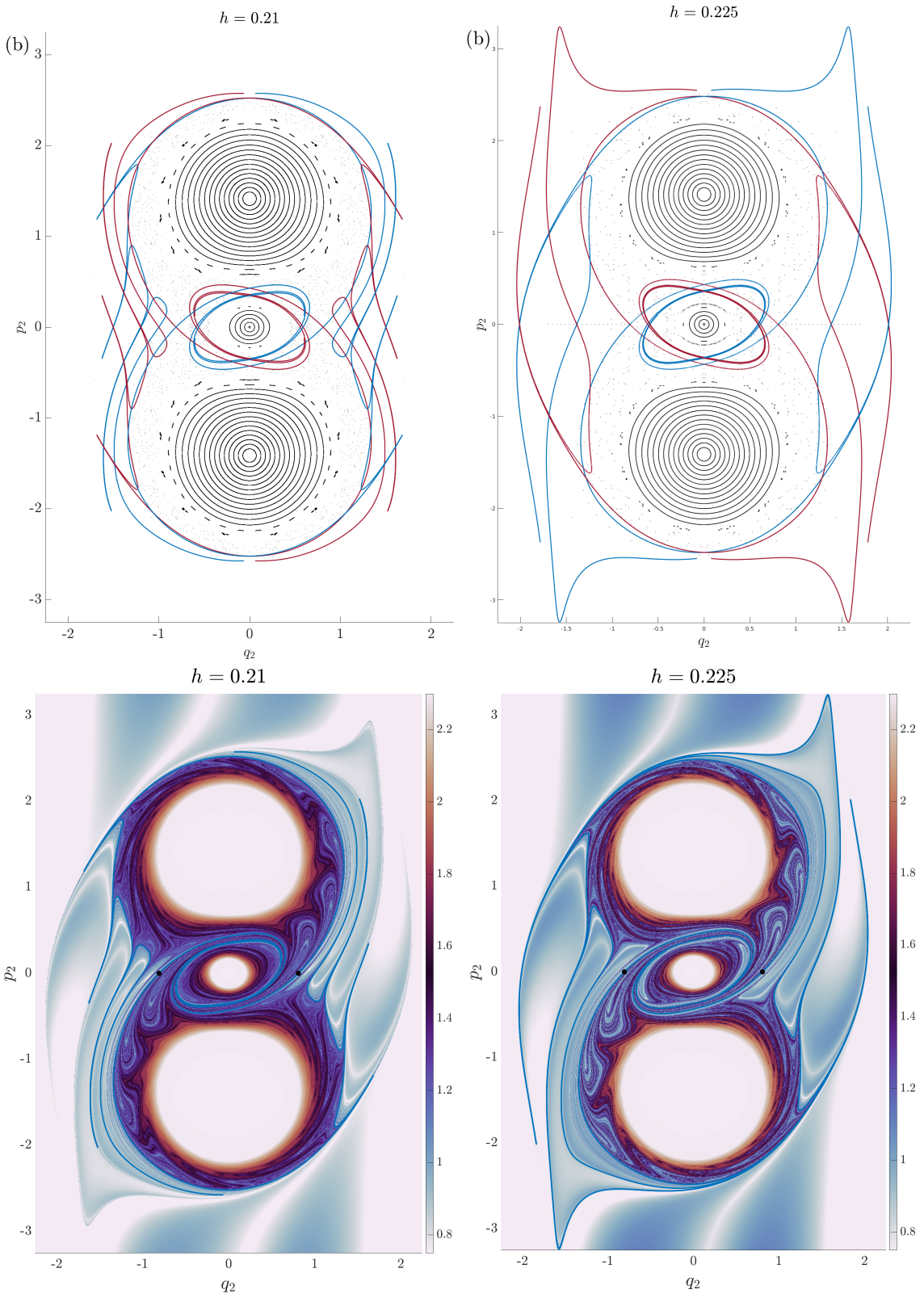

Figure 7.18 PSS and LD for $h = 0.21$ and $h = 0.225$. The stable and unstable manifolds of both RTT_L and RTT_R are colored in blue and red, respectively.

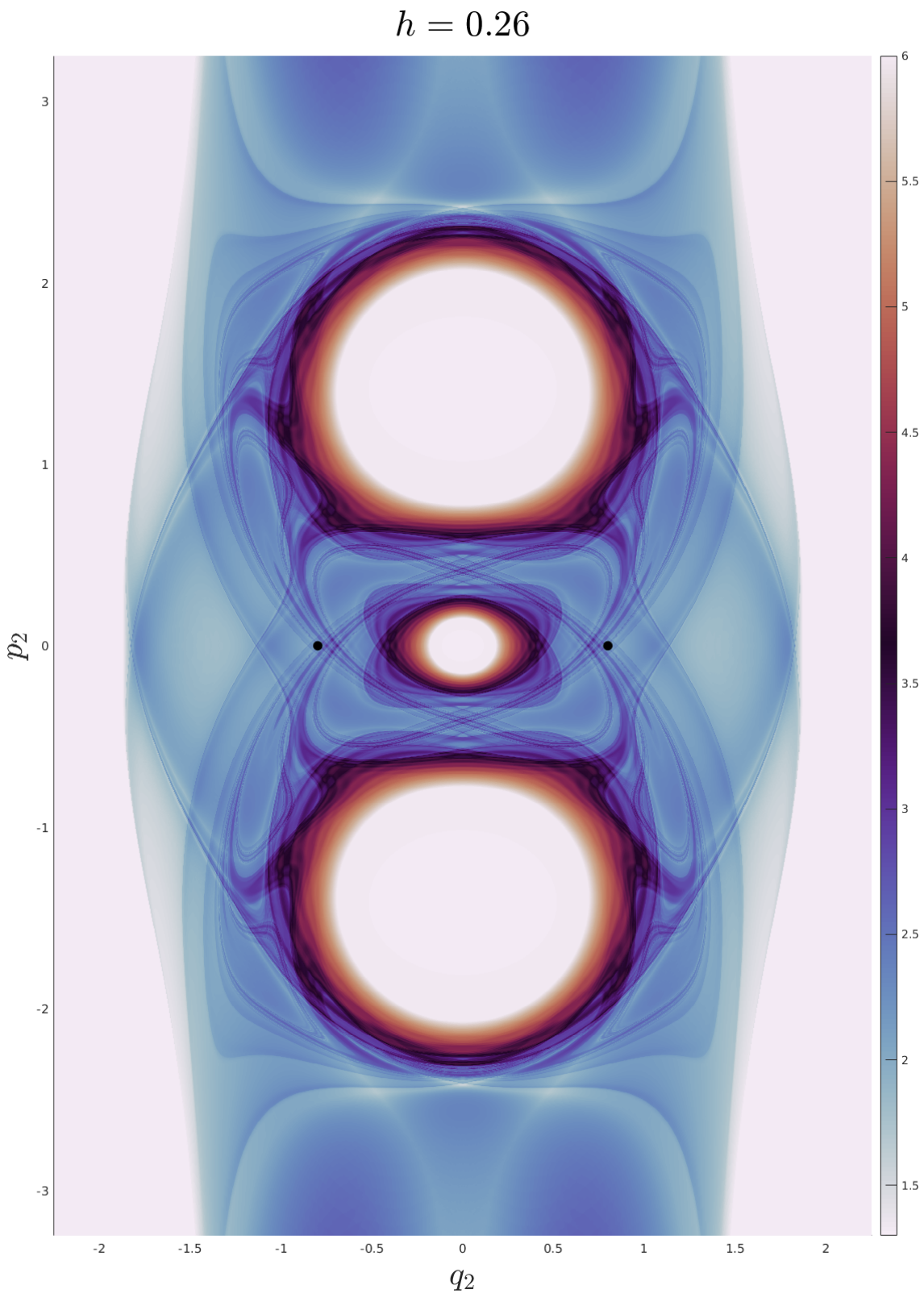

Figure 7.19 LD for $h = 0.26$ showing the skeleton of invariant manifolds.

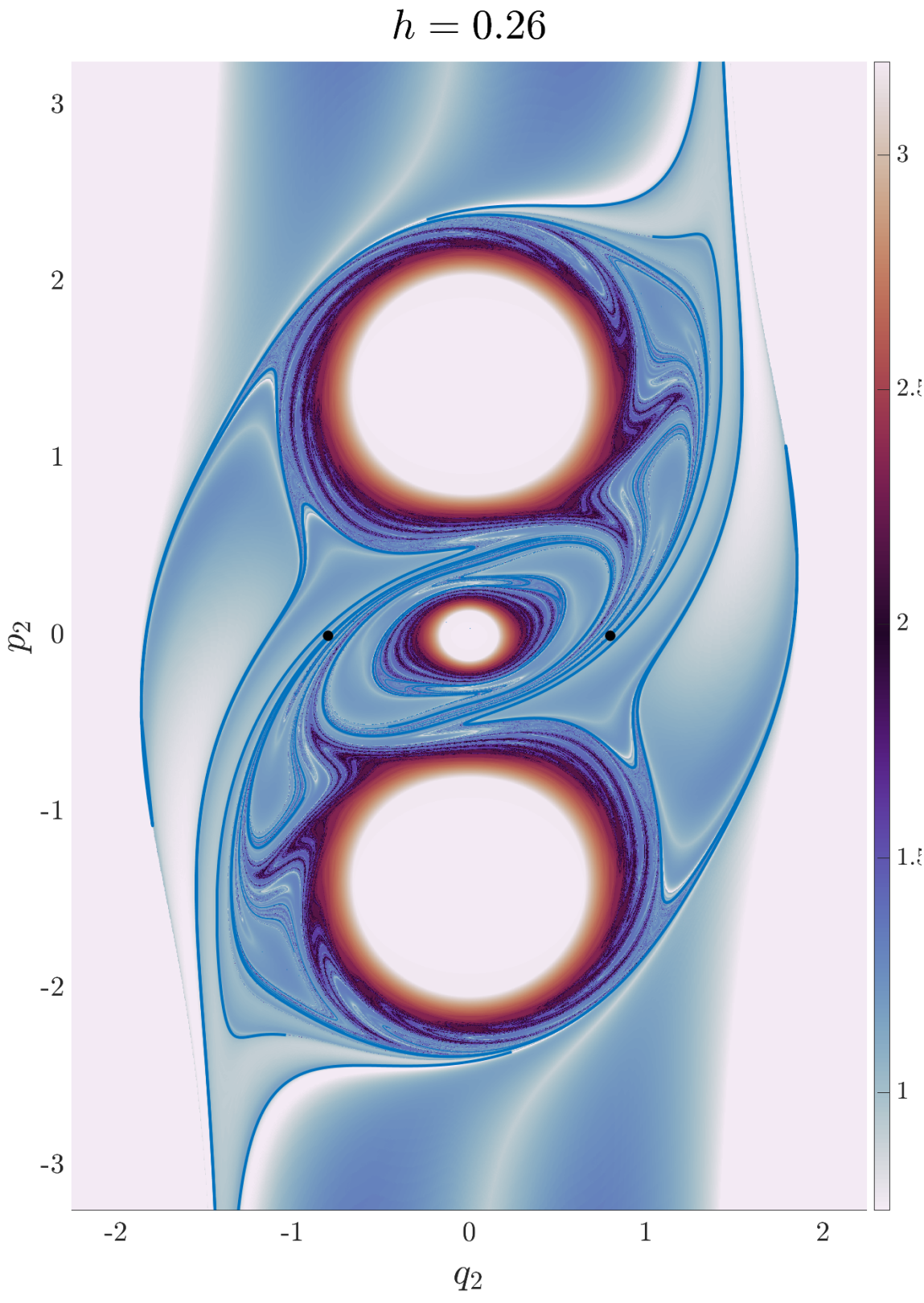

Figure 7.20 Forward-time LD for $h = 0.26$ with the stable manifolds of RTT_L and RTT_R in blue.

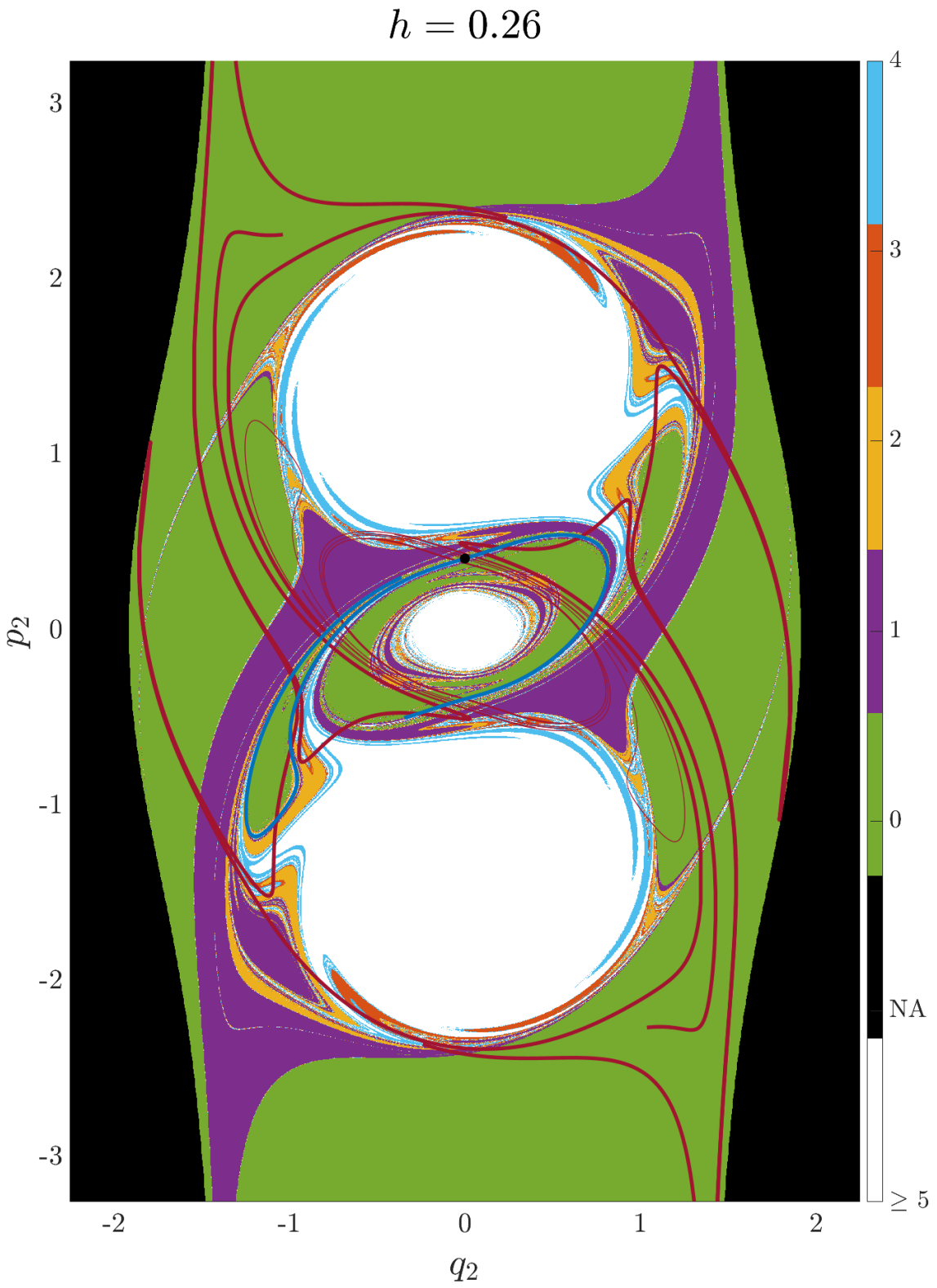

Figure 7.21 The forward time discrete escape plot with the stable manifolds (blue) of the leapfrogging orbit and the unstable manifolds of RTT_L and RTT_R (red) for $h = 0.26$.

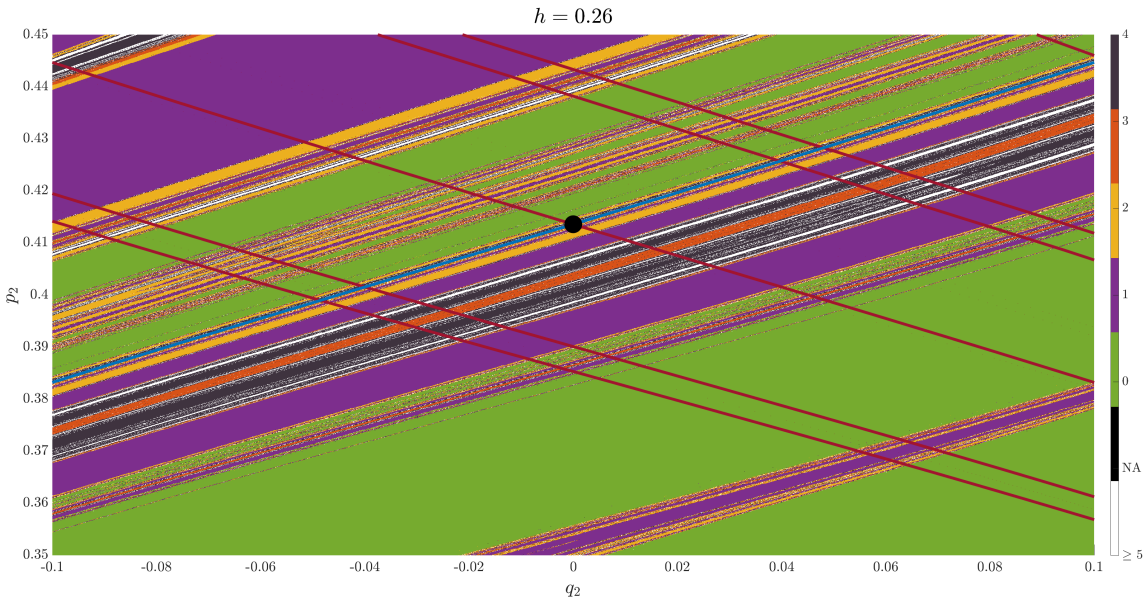

Figure 7.22 The forward time-discrete escape plot with the stable manifolds (blue) of the leapfrogging orbit and the unstable manifolds of RTT_L and RTT_R (red) for $h = 0.26$.

CHAPTER 8

CONCLUDING REMARKS

8.1 Conclusion

We recall the two goals laid out in Chapter 1:

1. **Goal I:** To demonstrate, without numerics, the exact algebraic value of the of the Hamiltonian of pitchfork bifurcation.

2. **Goal II:** Understand how, as the parameter h is increased, the dynamics transitions between the various regimes and escape becomes first possible and then almost inevitable, as well as identifying the structures in phase-space that are responsible for the transition between these regimes.

8.1.1 Goal I

The present paper represents our attempt to explain the fortuitous bifurcation value. Toward that end, we have derived an explicit reformulation of the stability problem, equation (5.16). We achieve this explicit form by a transformation used in solving the Kepler problem [30]. This formulation allows us to pose the stability problem with periodic coefficients that are given exactly, whereas previous studies considered linearizing about a numerical solution. This simplified problem allows us to show numerically that there is a periodic solution within an error on the scale of 10^{-120}

We then expand the system in a Fourier-Taylor series, using the energy h as a small parameter. We employ a classical technique from the study of lunar motion due to G. W. Hill, which uses the method of harmonic balance, to derive a sequence of algebraic criteria for the stability of the leapfrogging orbits. The roots of these polynomials form a sequence of approximations that appears to converge exponentially to h_c.

We had hoped that this analysis would provide insight into a mechanism illuminating the extraordinary algebraic critical value, perhaps in the form of an

exact formula for the periodic orbit. However, with this framework we do *prove* the existence a the bifurcation at this critical value.

8.1.2 Goal II

In the laboratory coordinates, it was possible to catalog many of the motions–some, such as braiding, which is easy to miss. In phase-space, the distinctions between these motions are clear- further, the structures that divide them become evident. With the right coordinate system, the structures of phase space that dictate the qualitative behavior of our system manifest themselves. In Chapter 6, we provide a comprehensive phenomenology of the vortex quartet, and in Chapter 7 we utilize this knowledge to understand the transitions of the perturbed leapfrogging orbit as we vary the energy level.

8.2 Future Work

For example, several generalizations of the leapfrogging solution exist and may be amenable to the techniques discussed here. First, leapfrogging solutions exist for quartets consisting of two pairs with vorticities $\Gamma_1^- = -\Gamma_1^+$ and $\Gamma_2^- = -\Gamma_2^+$. This system reduces to the case studied here when $\Gamma_1^+ = \Gamma_2^+$. In the more general case, the critical energy level should now depend on the ratio of the vorticities, $\lambda = \frac{\Gamma_1}{\Gamma_2}$. Acheson reports that he has investigated this situation numerically through direct simulations [2]. He makes a few observations about the behavior and suggests that it would be worthwhile to conduct a systematic analysis. We believe the semi-analytic method is especially well-suited for such an analysis as it will allow us to build the stability curves in (h, λ) space.

Another generalization is that leapfrogging solutions exist for a system of $2N$ vortices with $N > 2$, half with vorticity $+1$ and half with vorticity -1. As the leapfrogging of four vortices models the leapfrogging of two vortex rings, so the

leapfrogging of $2N$ vortices models the leapfrogging of N vortex rings, a problem that has been studied experimentally in superfluid helium. Wacks et al. has studied the latter system. [60]. While they found the motion to be stable in their numerical simulations, reduction to an ODE system would allow the exploration of a larger volume of parameter space and the application of more theoretical tools. A third generalization is to consider a system of vortices confined to a sphere; in this case, the leapfrogging solution is symmetric about a great circle. P. Newton [45] has simulated these solutions, but their stability has not been analyzed.

APPENDIX A

PARAMETER REFERENCE SHEET

The recent and classical literature: Aref and Tophøj [55], Gröbli [27] and Whitchurch et al. [61] all use different parameters to express the initial conditions, the parameterization of the periodic orbits and the range of values for which these orbits exist. We have gathered the results here.

Aref and Tophøj [55] use the Hamiltonian

$$H(X,Y) = -\frac{1}{2}\log\left(\frac{1}{1-Y^2} - \frac{1}{1+X^2}\right)$$

with equations of motion in terms of the conserved quantity $h = e^{2H}$

$$\begin{aligned}
\frac{dX}{dt} &= -\frac{Y(1+X^2)}{(X^2+Y^2)(1-Y^2)} = -h\frac{Y}{(1-Y^2)^2} \\
\frac{dY}{dt} &= \frac{X(1-Y^2)}{(X^2+Y^2)(1+X^2)} = h\frac{X}{(1+X^2)^2}
\end{aligned}$$

and initial conditions given in terms of the ratio of the breadths of the pairs, α,

$$\begin{aligned}
X(0) &= 0 \\
Y(0) &= \frac{1-\alpha}{1+\alpha} = \frac{1}{\sqrt{h+1}}.
\end{aligned}$$

The conserved quantity h can be written in a few different ways

$$\begin{aligned}
h &= \frac{4\alpha}{(1-\alpha)^2} \\
&= \frac{(1+X^2)(1-Y^2)}{X^2+Y^2} \\
&= e^{2H}
\end{aligned}$$

and the relationship between α and h can be inverted

$$\alpha = \frac{2+h\pm 2\sqrt{h+1}}{h}.$$

Table A.1 Comparison of Important Parameters

Author	Permissible Values	Critical Value
Love	$3 - 2\sqrt{2} < \alpha < 1$	$\alpha_c = \frac{3-\sqrt{5}}{2}$
Gröbli	$1 < \lambda < \infty$	$\lambda_c = 4$
Whitchurch	$0 < H < \infty$	$H_c = \log 2$
Behring	$0 < \tilde{H} < \frac{1}{2}$	$\tilde{H}_c = \frac{1}{8}$

Gröbli [27] uses λ which is equivalent to $\frac{1}{2h}$. Whitchurch et al. [61] use the energy H itself as their parameter. In this text, we use the energy level sets of a rescaled Hamiltonian, $\tilde{H} = \frac{1}{2}e^{-2H} = \frac{1}{2h}$.

The list of permissible values for periodic motion and the critical value for instability are summarized below in Table A.1.

APPENDIX B

CLOSED FORM RESULTS FOR THE LEAPFROGGING SOLUTION

In this Appendix we will consider some classical results of closed-form solutions to the Leapfrogging problem. Consider the Hamiltonian system

$$H(X,Y) = \frac{1}{2}\left(\frac{1}{1-Y^2} - \frac{1}{1+X^2}\right) \tag{B.1}$$

with equations of motion

$$\frac{dX}{dt} = \frac{\partial H}{\partial Y} = \frac{Y}{(1-Y^2)^2} \tag{B.2a}$$

$$\frac{dY}{dt} = -\frac{\partial H}{\partial X} = -\frac{X}{(1+X^2)^2} \tag{B.2b}$$

and initial conditions

$$X(0) = 0 \tag{B.3a}$$

$$Y(0) = \sqrt{\frac{1}{1+h}}. \tag{B.3b}$$

Here, $h = \frac{1}{2H(0,Y_0)}$ is the parameter that will be related to the energy level. We will later see periodic orbits exist for $h > 1$. We can then use this conserved quantity, h, to solve for (say) Y in terms of X,

$$Y^2 = \frac{1}{h+1}\frac{1-(h-1)X^2}{1+\frac{X^2}{h+1}}$$

and plug this into (B.2a) to render the equation of motion for $\dot{X}$ entirely in terms of X,

$$\frac{dX}{dt} = \frac{1}{h^2\sqrt{h+1}}\left(1 - \frac{h}{h+1}\frac{1}{1+\frac{x^2}{h+1}}\right)^{-2}\sqrt{\frac{1-(h-1)x^2}{1+\frac{x^2}{h+1}}}. \tag{B.4}$$

B.1 Implicit Solution

We can now solve for dt using (B.4) and integrating yields

$$\begin{aligned}
t(X) &= h^2\sqrt{h+1}\int_0^X \left(1-\frac{h}{h+1}\frac{1}{1+\frac{x^2}{h+1}}\right)^2 \sqrt{\frac{1+\frac{x^2}{h+1}}{1-(h-1)x^2}}dx \\
&= h^2\sqrt{\frac{h+1}{h-1}}\int_0^{X\sqrt{h-1}} \left(1-\frac{h}{h+1}\frac{1}{1-k^2u^2}\right)^2 \sqrt{\frac{1-k^2u^2}{1-u^2}}du \\
&= h^2\sqrt{\frac{h+1}{h-1}}\Bigg[\int_0^{X\sqrt{h-1}} \frac{1}{\sqrt{1-k^2u^2}\sqrt{1-u^2}}du \\
&\quad -\frac{2^2h}{h+1}\int_0^{X\sqrt{h-1}} \frac{\sqrt{1-k^2u^2}}{\sqrt{1-u^2}}du \\
&\quad +\frac{h^3}{(h+1)^2}\int_0^{X\sqrt{h-1}} \frac{1}{(1-k^2u^2)\sqrt{1-k^2u^2}\sqrt{1-u^2}}du\Bigg] \\
&= h^2\sqrt{\frac{h+1}{h-1}}\left(F(\theta,k)-\frac{2h}{h+1}E(\theta,k)+\frac{h^2}{(h+1)^2}\Pi(\theta,k^2,k)\right) \\
&= \frac{2h^2}{\sqrt{h^2-1}}\Big(F(\arcsin(X\sqrt{h-1},k)-E(\arcsin(X\sqrt{h-1},k)\Big) \\
&\quad -\frac{h+1}{\sqrt{h-1}h\sqrt{h+X^2+1}}.
\end{aligned}$$

where we have used the substitutions $u = \sqrt{h-1}X$, $\sin\theta = x\sqrt{h-1}$ and $k^2 = 1/(1-h^2)$. Observe that since $h > 1$, this choice gives an imaginary k. We have used the identity (DLMF 19.6.3),

$$\Pi(\theta,k^2,k) = \frac{1}{1-k^2}\left(E(\theta,k)-\frac{k^2}{\sqrt{1-k^2\sin^2\theta}}\right),$$

to remove the incomplete elliptic integral of the third kind.

B.2 Period

Observing that $t|_{x=\frac{1}{\sqrt{h-1}}}$ is a quarter period allows us to compute the period in terms of complete elliptic functions. A few equivalent expressions are

$$T_{\text{leapfrog}} = \frac{8h^3}{h+1}\sqrt{\frac{h+1}{h-1}}\left(K\left(\frac{i}{\sqrt{h^2-1}}\right) - E\left(\frac{i}{\sqrt{h^2-1}}\right)\right) \tag{B.5a}$$

$$T_{\text{leapfrog}} = \frac{8h^3}{h+1}\sqrt{\frac{h+1}{h-1}}\left(\frac{\sqrt{h^2-1}}{h}K\left(\frac{1}{h}\right) - \frac{h}{\sqrt{h^2-1}}E\left(\frac{1}{h}\right)\right) \tag{B.5b}$$

$$T_{\text{leapfrog}} = 8h^2\left(K\left(\frac{1}{h}\right) - \frac{h^2}{h^2-1}E\left(\frac{1}{h}\right)\right). \tag{B.5c}$$

For these expressions, we have used DLMF 19.7.2,

$$\begin{aligned} K(ik/k') &= k'K(k), \\ E(ik/k') &= \frac{1}{k'}E(k), \end{aligned}$$

with $k = h$ and $k' = \frac{\sqrt{h^2-1}}{h}$ so $k^2 + k'^2 = 1$ to obtain expressions with a real modulus.

B.3 Action

In a similar way, we can compute the action using DLMF 19.2.4, 19.2.5 and 19.2.6

$$\begin{aligned} J &= \oint Y dX \\ &= 4\int_0^{\frac{1}{\sqrt{h-1}}} \sqrt{\frac{1+(1-h)X^2}{X^2+h+1}}dX \\ &= \frac{4}{\sqrt{h^2-1}}\int_0^1 \sqrt{\frac{1-u^2}{1-k^2u^2}}du \\ &= \frac{4}{\sqrt{h^2-1}}\int_0^{\frac{\pi}{2}} \frac{1-\sin^2\theta}{\sqrt{1-k^2\sin^2\theta}}d\theta \\ &= \frac{4}{\sqrt{h^2-1}}\left(K(k) - D(k)\right) \\ &= \frac{4}{\sqrt{h^2-1}}\left(K(k) - \frac{1}{k^2}\left(K(k) - E(k)\right)\right) \\ &= \frac{4}{\sqrt{h^2-1}}\left(h^2K(k) + (1-h^2)E(k)\right). \end{aligned}$$

We have used DLMF 19.2.7,

$$\begin{aligned} D(k) &\equiv \int_0^{\frac{\pi}{2}} \frac{\sin^2\theta}{\sqrt{1-k^2\sin^2\theta}} d\theta \\ &= \frac{1}{k^2}\left(K(k) - E(k)\right). \end{aligned}$$

Using 19.4 of DLMF we can also write this as

$$J(h) = 4h\left(K\left(\frac{1}{h}\right) - E\left(\frac{1}{h}\right)\right). \tag{B.6a}$$

$$J(h) = iE\left(i\sinh^{-1}\left(\frac{1}{h^2-1}\right), i\sqrt{h^2-1}\right). \tag{B.6b}$$

This relationship also gives us another way to calculate the period. Since $\frac{\partial H(J)}{\partial J} = \nu$, we can also calculate $\frac{\partial J(h)}{\partial h} = T_{lf}$ to get the same period as found earlier.

APPENDIX C

PERTURBATIVE EXPANSIONS OF THE LEAPFROGGING ORBIT

C.1 Poincare-Lindstedt Expansion of the Leapfrogging Orbit

In this Appendix we consider asympotitic expansion of the leapfrogging orbit. We will first approximate the periodic orbits in the invariant subspace using the Poincaré–Lindstedt technique. We will also arrive at the same results using Hamiltonian normal forms; this will serve as a confirmation of those results. We can expand the equations of motion as

$$\frac{dX}{dt} = \frac{Y}{(1-Y^2)^2} = \sum_{n=1}^{\infty} nY^{2n-1} \tag{C.1a}$$

$$\frac{dY}{dt} = -\frac{X}{(1+X^2)^2} = \sum_{n=1}^{\infty} n(-1)^n X^{2n-1} \tag{C.1b}$$

Solutions on the energy level $H = E$ with $X(0) = 0$ have

$$Y(0) = \sqrt{\frac{2E}{2E+1}}. \tag{C.2}$$

In order to find a Poincaré–Linstedt expansion of the periodic solutions to this system we let $X = \sqrt{\epsilon}x$ and $Y = \sqrt{\epsilon}y$ where ϵ will be the small parameter E. Plugging this into (C.1) and dividing by $\sqrt{\epsilon}$ we find

$$\frac{dx}{dt} = \sum_{n=1}^{\infty} n\epsilon^{n-1} y^{2n-1} \tag{C.3a}$$

$$\frac{dy}{dt} = \sum_{n=1}^{\infty} n(-1)^n \epsilon^{n-1} x^{2n-1} \tag{C.3b}$$

and initial conditions $x(0) = 0$ and

$$y(0) = \sqrt{\frac{2}{2\epsilon+1}} = \sqrt{2}\sum_{k=1}^{\infty} 2^k \binom{k-\frac{1}{2}}{k} (-1)^k \epsilon^k = \sqrt{2} - \sqrt{2}\epsilon + \frac{3\sqrt{2}}{2}\epsilon^2 + O(\epsilon^3) \tag{C.4}$$

We could have changed the initial conditions as to make $y(0)$ independent of ϵ; however, that would necessitate changing the parameter, and for the moment keeping $\epsilon = E$ as the small parameter makes it easy to compare the results of this section with the previous numerics and with the results that will follow using Lie transform methods. It also keeps the bifurcation value as $E_c = \epsilon_c = \frac{1}{8}$. Having higher order ϵ terms in $y(0)$ does not require any additional difficulty when implementing the algorithm in Mathematica.

Introducing the strained coordinate $\theta = \omega(\epsilon)t$ the perturbed solution will now have period of 2π with respect to θ. Since the period with $\epsilon = 0$ is 2π, $\omega(0) = 1$ where ω is given by the asymptotic power series

$$\omega(\epsilon) \sim 1 + \sum_{n=1}^{\infty} \epsilon^n \omega^n. \tag{C.5}$$

We also introduce the expansions

$$x \sim X_0 + \epsilon X_1 + \epsilon^2 X_2 + \dots \tag{C.6a}$$

$$y \sim Y_0 + \epsilon Y_1 + \epsilon^2 Y_2 + \dots . \tag{C.6b}$$

and collect all powers of ϵ by inserting (C.6) and (C.5) into (C.3). Keeping all terms relevant to order ϵ^2

$$(1 + \omega_1\epsilon + \omega_2\epsilon^2)\frac{d}{d\theta}\begin{bmatrix} X_0 + \epsilon X_1 + \epsilon^2 X_2 \\ Y_0 + \epsilon Y_1 + \epsilon^2 Y_2 \end{bmatrix} = \begin{bmatrix} 0 & 1 \\ -1 & 0 \end{bmatrix}\begin{bmatrix} X_0 + \epsilon X_1 + \epsilon^2 X_2 \\ Y_0 + \epsilon Y_1 + \epsilon^2 Y_2 \end{bmatrix} + \epsilon \begin{bmatrix} 2Y_0^3 \\ 2X_0^3 \end{bmatrix} + \epsilon^2 \begin{bmatrix} 6Y_0^2 Y_1 + 3Y_0^5 \\ 6X_0^2 X_1 - 3X_0^5 \end{bmatrix}.$$

Collecting terms of order ϵ^0, we have

$$\frac{d}{d\theta}\begin{bmatrix} X_0 \\ Y_0 \end{bmatrix} = \begin{bmatrix} 0 & 1 \\ -1 & 0 \end{bmatrix}\begin{bmatrix} X_0 \\ Y_0 \end{bmatrix} \tag{C.7}$$

with $X_0(0) = 0$ and $Y_0(0) = \sqrt{2}$. This gives

$$X_0(\theta) = \sqrt{2}\sin\theta \tag{C.8a}$$

$$Y_0(\theta) = \sqrt{2}\cos\theta. \tag{C.8b}$$

as expected. We will define

$$\mathcal{L} = \frac{d}{d\theta} - \begin{bmatrix} 0 & 1 \\ -1 & 0 \end{bmatrix}, \tag{C.9}$$

with the inner product given by

$$\langle u, v\rangle = \int_0^{2\pi} u^T v d\theta.$$

Then the adjoint nullspace is

$$\ker \mathcal{L}^\dagger = \text{span}\{(\cos\theta, -\sin\theta), (\sin\theta, \cos\theta)\}.$$

To order ϵ,

$$\begin{aligned}\frac{d}{d\theta}\begin{bmatrix} X_1 \\ Y_1 \end{bmatrix} &= \begin{bmatrix} 0 & 1 \\ -1 & 0 \end{bmatrix}\begin{bmatrix} X_1 \\ Y_1 \end{bmatrix} + \begin{bmatrix} 2Y_0^3 \\ 2X_0^3 \end{bmatrix} - \omega_1 \begin{bmatrix} X_0' \\ Y_0' \end{bmatrix} \\ &= \begin{bmatrix} 0 & 1 \\ -1 & 0 \end{bmatrix}\begin{bmatrix} X_1 \\ Y_1 \end{bmatrix} - \begin{bmatrix} 3\sqrt{2}\cos\theta + \sqrt{2}\cos(3\theta) \\ 3\sqrt{2}\sin\theta - \sqrt{2}\sin(3\theta) \end{bmatrix} + \omega_1 \begin{bmatrix} \sqrt{2}\cos\theta \\ -\sqrt{2}\cos\theta \end{bmatrix}\end{aligned}$$

with $X_1(0) = 0$ and $Y_1(0) = -\sqrt{2}$. We now require the inhomogeneous terms to be perpendicular to the adjoint nullspace, we find $\omega_1 = 0$ and

$$X_1(\theta) = \frac{1}{2}\left(3\sqrt{2}\sin\theta + \sqrt{2}\sin 3\theta\right) \tag{C.10a}$$

$$Y_1(\theta) = \frac{1}{2}\left(\sqrt{2}\cos 3\theta - 3\sqrt{2}\cos\theta\right). \tag{C.10b}$$

This process has been coded in Mathematica and worked out to tenth order, finding that

$$\omega = 1 - \frac{9\epsilon^2}{2} + \frac{3\epsilon^4}{2} + \frac{17\epsilon^6}{16} + \frac{99\epsilon^8}{64} + \frac{381\epsilon^{10}}{128} + O\left(\epsilon^{12}\right).$$

This expansion is in agreement with the Taylor series of the complete elliptic integrals in the expansion

$$\omega = \frac{T}{2\pi} = \sqrt{\frac{h^2-1}{h^3}} \frac{\pi}{4h\left(E\left(k^2\right) - K\left(k^2\right)\right)}.$$

In principle, this can be worked out to arbitrary order. However, solving a system of linear ODEs at each step, while straightforward can become taxing at higher orders. The Lie transform is entirely algebraic (except for averaging over trigonometric functions) and is considerably faster.

We can analyze the error of the approximations at $E = \frac{1}{4}$ and $E = \frac{1}{8}$ to confirm that the results converge to the numerical solution found with MATLAB `ode45` at the expected rate. We will use $\Delta_E(n)$ as the discrete l_2 norm at each mesh point to compare the total separation of the approximation with the numerical solution. We should expect expect $\Delta_{\frac{1}{4}}/\Delta_{\frac{1}{8}} \approx \frac{1/4^n}{1/8^n} = 2^n$, which we do indeed observe.

C.2 Normal Form for the Leapfrogging Orbits

The Hamiltonian in the invariant plane can be expanded as a geometric series as

$$H = \frac{1}{2}\Big(\frac{1}{1-Y^2} - \frac{1}{1+X^2}\Big) = \frac{1}{2}\Big(Y^2 + X^2\Big) + \sum_{n=2}^{\infty} \frac{1}{2}\Big(Y^{2n} + (-1)^{n+1} X^{2n}\Big). \quad \text{(C.11)}$$

As can be observed from the phase plane, for small X and Y this is roughly a harmonic oscillator with circular orbits. By finding the normal form we can expand on this observation. There are two straightforward ways to bring this Hamiltonian into a normal form. We can put X and Y into complex coordinates

$$X = \frac{z + \bar{z}}{2}, \quad Y = \frac{z - \bar{z}}{2i}$$

and find generating functions W_i that make the transformed Hamiltonian real or put X and Y into symplectic polar coordinates

$$X = \sqrt{2J}\cos\theta, \quad Y = \sqrt{2J}\sin\theta$$

and find generating functions W_i that make the transformed Hamiltonian independent of θ. Both methods will produce the same result. We will use the latter.

1. **Setup** We can write (C.11) using symplectic polar coordinates as

$$H = \sum_{n=0}^{\infty} \epsilon^n \frac{H_n^0(\theta, J)}{n!} \tag{C.12}$$

where,

$$\begin{aligned}
H_0^0 &= \frac{1}{2}\left(X^2 + Y^2\right) = J, \\
H_1^0 &= \frac{1}{2}\left(-X^4 + Y^4\right) = -2\cos 2\theta J^2, \\
H_2^0 &= \frac{2!}{2}\left(X^6 + Y^6\right) = \left(5 + 3\cos 4\theta\right) J^3, \\
H_3^0 &= \frac{3!}{2}\left(-X^8 + Y^8\right) = -6(7\cos 2\theta + \cos 6\theta) J^4.
\end{aligned}$$

The transformation into the new coordinates is canonical and the Poisson bracket in the polar variables is

$$\{F, G\} = \frac{\partial F}{\partial \theta}\frac{\partial G}{\partial J} - \frac{\partial F}{\partial J}\frac{\partial G}{\partial \theta}.$$

Using the scaling $H \to \epsilon H$ and $J \to \epsilon J$, we formally add the factor ϵ to keep track of terms. We will later set $\epsilon = 1$.

In this case the unperturbed problem is $H = H_0 = J$, which is just the harmonic oscillator with unit frequency.

2. **First Order** The first row of the Lie triangle, (2.21) gives

$$\begin{aligned} H_0^1 &= H_1^0 + \{H_0^0, W_1\} \\ &= -2\cos 2\theta J^2 - \frac{\partial W_1}{\partial \theta}. \end{aligned}$$

Choosing W_1 to get rid of all angular dependence of H_0^1,

$$\begin{aligned} \frac{\partial W_1}{\partial \theta} &= -2\cos 2\theta J^2 \\ W_1 &= \sin 2\theta J^2. \end{aligned}$$

In the Mathematica code, this step is implemented by averaging both sides to remove the θ dependence. Now, $H_0^1 = 0$ and

$$H_*(\epsilon, J, \theta) = J + O(\epsilon^2).$$

3. **Second Order** The next row of the Lie triangle and (2.21) can be used to find H_0^2,

$$\begin{aligned} H_0^2 &= H_1^1 + \{H_0^1, W_1\} \\ &= H_2^0 + \{H_1^0, W_1\} + \{H_0^0, W_2\} + \{H_0^1, W_1\} \\ &= \left(5 + 3\cos 4\theta\right) J^3 - 8J^3 - \frac{\partial W_2}{\partial \theta}. \end{aligned}$$

Removing the angular dependence demands,

$$W_2 = \frac{3}{4} J^3 \sin 4\theta.$$

and

$$H^*(\epsilon, J, \theta) = J - \frac{3}{2} J^3 + O(J^4).$$

So far, this agrees with the series expansion for $H(J)$.

4. **Higher Order Terms**

We can run this algorithm to as high of order as we would like. Taking $\epsilon = 1$, we will summarize some of these results. The Hamiltonian is given by

$$H(J) = J - \frac{3}{2}J^3 + 3J^5 - \frac{103}{16}J^7 + O\left(J^9\right).$$

with equations of motion

$$\begin{aligned}
\dot{J} &= -\frac{\partial H}{\partial \theta} = 0, \\
\dot{\theta} &= \frac{\partial H}{\partial \theta} = 1 - \frac{9J^2}{2} + 15J^4 + \frac{721J^6}{16} + O(J^6).
\end{aligned}$$

The first few W_i are

$$\begin{aligned}
W_1 &= J^2 \sin 2\theta, \\
W_2 &= \frac{3}{4}J^3 \sin 4\theta, \\
W_3 &= J^4 \left(3\sin 2\theta + \sin 6\theta\right), \\
W_4 &= J^5 \left(\frac{33}{2}\sin 4\theta + \frac{15}{8}J^5 \sin 8\theta)\right), \\
W_5 &= 63J^6 \left(2\sin 2\theta + 165\sin 6\theta + 9\sin 10\theta\right), \\
W_6 &= \frac{1}{8}J^7 \left(13605\sin 4\theta + 3435\sin 8\theta + 105\sin 2\theta\right).
\end{aligned}$$

In Appendix B.3, it is shown that the action is given by

$$\begin{aligned}
J &= \frac{1}{2\pi}\oint Y dX \\
&= \frac{1}{\pi H}\Big(E(2H) - K(2H)\Big).
\end{aligned}$$

This can not be inverted to find H in terms of J analytically. However, by using the Taylor series for complete elliptic functions, it can be shown that the

asymptotic series for the action, J, begins as

$$J(H) = H + \frac{3H^3}{2} + \frac{15H^5}{4} + \frac{175H^7}{16} + \frac{2205H^9}{64} + \frac{14553H^{11}}{128} + \frac{99099H^{13}}{256} + O\left(H^{15}\right) \tag{C.13}$$

which can be inverted to find

$$H(J) = J - \frac{3}{2}J^3 + 3J^5 - \frac{103}{16}J^7 + \frac{915}{64}J^9 - \frac{4149}{128}J^{11} + \frac{19075}{256}J^{13} + O\left(J^{15}\right). \tag{C.14}$$

This is consistent with our normal form result.

C.3 Change of Coordinates using Lie Transforms

The generating functions allow a change of coordinates from the unperturbed problem to the perturbed problem. That is, W_i induces a coordinate transformation for the new θ^* and J^* in terms of the old θ and J using the Lie triangle. The first few terms are

$$J^* = J - 2J^2\cos 2\theta + \frac{J^3}{2}(8 - 3\cos 4\theta) - \frac{J^4}{4}(\cos 2\theta + 7\cos 6\theta)) + O(J^5)$$

and

$$\begin{aligned}\theta^* =& \theta + 2J\sin 2\theta + \frac{17}{8}J^2\sin 4\theta \\ &+ \frac{J^3}{12}(37\sin 6\theta - 39\sin 2\theta) + \frac{J^4}{48}(244\sin 8\theta - 353\sin 4\theta) + O(J^5).\end{aligned}$$

The solution to the unperturbed problem $H_0 = J$ is

$$\begin{aligned}X_0(J,\theta) &= \sqrt{2J}\sin\theta, \\ Y_0(J,\theta) &= \sqrt{2J}\cos\theta\end{aligned}$$

where $\theta = t$. In the transformed variables, (J^*, θ^*), X and Y are given by

$$X(J,\theta) = \sqrt{2J^*}\sin\theta^* \tag{C.15a}$$

$$Y(J,\theta) = \sqrt{2J^*}\cos\theta^* \tag{C.15b}$$

where

$$\theta = \omega t = \left(1 - \frac{9J^2}{2} + 15J^4 + \frac{721J^6}{16} + \dots\right) t.$$

Expanding (C.15) and using (C.13) to remove J^*, we arrive at equations in the original coordinates. To first order,

$$X(\theta) = \sqrt{2H}\left(\sin\theta + \frac{H}{2}\left(3\sin\theta + \sin 3\theta\right) + O(H^2)\right) \tag{C.16a}$$

$$Y(\theta) = \sqrt{2H}\left(\cos\theta + \frac{H}{2}\left(\cos 3\theta - 3\cos\theta\right) + O(H^2)\right). \tag{C.16b}$$

We can analyze the error of the approximations at $E = \frac{1}{4}$ and $E = \frac{1}{8}$ to confirm that the results converge to the numerical solution found with MATLAB `ode45` at the expected rate. $\Delta_E(n)$ is taken to be the discrete l_2 norm at each mesh point to compare the total separation of the approximation with the numerical solution. The error ratio should should go up by a factor of two as we add a new term to our expansion as seen in Table C.1.

Table C.1 Convergence of Asymptotic Expansions

Order	$\Delta_{\frac{1}{4}}$	$\Delta_{\frac{1}{8}}$	$\Delta_{\frac{1}{4}}/\Delta_{\frac{1}{8}}$	$\log_2\left(\Delta_{\frac{1}{4}}/\Delta_{\frac{1}{8}}\right)$
1	9.259005409	1.315307630	7.04	2.81
2	0.470145680	0.028243406	16.65	4.06
3	0.291026866	0.007774063	37.44	5.22
4	0.085970168	0.001369417	62.78	5.97
5	0.038049990	0.000285269	133.38	7.06
6	0.018444049	0.000072420	254.68	7.99
7	0.008278637	0.000015669	528.34	9.04
8	0.004109456	0.000003999	1027.58	10.01
9	0.001882635	0.000000892	2111.46	11.04
10	0.000937033	0.000000227	4126.16	12.01

BIBLIOGRAPHY

[1] Ralph Abraham and Jerrold E. Marsden. *Foundations of mechanics*. AMS Chelsea Publishing, 2011.

[2] D. J. Acheson. Instability of vortex leapfrogging. *Eur. J. Phys.*, 21:269–273, 2000.

[3] M. Agaoglou, B. Aguilar-Sanjuan, V. J. García-Garrido, R. García-Meseguer, F. González-Montoya, M. Katsanikas, V. Krajňák, S. Naik, and S. Wiggins. Chemical reactions: A journey into phase space, December 2019. https://champsproject.github.io accessed on July 1, 2020.

[4] M. Agaoglou, B. Aguilar-Sanjuan, V. J. García Garrido, F. González-Montoya, M. Katsanikas, V. Krajňák, S. Naik, and S. Wiggins. Lagrangian descriptors: Discovery and quantification of phase space structure and transport. accessed on July 1, 2020. https://champsproject.github.io/lagrangian_descriptors/ accessed on July 1, 2020.

[5] M. H. Anderson, J. R. Ensher, M. R. Matthews, C. E. Wieman, and E. A. Cornell. Observation of Bose-Einstein condensation in a dilute atomic vapor. *Science*, 269:198–201, 1995.

[6] H. Aref. Three-vortex motion with zero total circulation: Addendum. *Z. Angew. Math Phys.*, 40:495–500, 1989.

[7] H. Aref. Point vortex dynamics: A classical mathematics playground. *J. Math. Phys.*, 48:065401, 2007.

[8] H. Aref, N. Rott, and H. Thomann. Gröbli's solution of the three-vortex problem. *Annu. Rev. Fluid Mech.*, 24:1–21, 1992.

[9] V. I Arnold. *Dynamical systems III*. Springer-Verlag, 1988.

[10] B. M. Behring and R. H. Goodman. Stability of leapfrogging vortex pairs: A semi-analytic approach. *Phys. Rev. Fluids*, 4:124703, Dec 2019.

[11] S. Blanes, F. Casas, J. A. Oteo, and J. Ros. *The Magnus expansion and some of its applications*. Elsevier, 2009.

[12] D. Boccaletti and G. Pucacco. *Theory of Orbits Volume 2: Perturbative and geometrical methods*. Springer, 2011.

[13] S. Bolotin and D. Treschev. Hill's formula. *Russ. Math. Surv.*, 65:191–257, 2010.

[14] A. V. Borisov, A. A. Kilin, and I. S. Mamaev. Reduction and chaotic behavior of point vortices on a plane and a sphere. *Discrete Contin. Dyn. Syst.*, 54(suppl.):100–109, 2005.

[15] J. R. Cary. Lie transform perturbation theory for Hamiltonian systems. *Phys. Rep.*, 1981.

[16] F. Casas. A lie-deprit perturbation algorithm for linear differential equations with periodic coefficients. *Discrete Contin. Dyn. Syst. Ser. A*, 2014.

[17] F. Casas, J. A. Oteo, and J. Ros. Unitary transformations depending on a small parameter. *Proc. Math. Phys. Eng. Sci.*, 2012.

[18] Carmen Charles. Chicone. *Ordinary differential equations with applications*. Springer, 2006.

[19] D. L. Cowern. Crazy pool vortex. [YouTube video]. https://youtu.be/pnbJEg9r1o8 accessed on April 19, 2020. Accessed November 22nd, 2020.

[20] F. J. Dyson. The radiation theories of Tomonaga, Schwinger, and Feynman. *Phys. Rev.*, 1948.

[21] B. Eckhardt and H. Aref. Integrable and chaotic motions of four vortices II. Collision dynamics of vortex pairs. *Philos. Trans. R. Soc. London, Ser. A*, 1988.

[22] G. Floquet. Sur les équations différentielles linéaires à coefficients périodiques. In *Annales scientifiques de l'École normale supérieure*, volume 12, pages 47–88, 1883.

[23] V. J. García-Garrido. An extension of discrete lagrangian descriptors for unbounded maps. *Int J. Bifurcat. Chaos*, 30(05):2030012, 2020.

[24] A. B. Givental, B. A. Khesin, J. E. Marsden, A. N. Varchenko, V. A. Vassiliev, Oleg Y. Viro, and V. M. Zakalyukin, editors. *Small denominators and problems of stability of motion in classical and celestial mechanics*, pages 306–412. Springer Berlin Heidelberg, Berlin, Heidelberg, 2009.

[25] Herbert Goldstein, Charles Poole, and John Safko. *Classical mechanics*. Addison Wesley, 2002.

[26] R. H. Goodman and J. K. Wróbel. High-order bisection method for computing invariant manifolds of two-dimensional maps. *Int. J. Bifurcat. Chaos*, 21:2017–2042, 2011.

[27] W. Gröbli. *Spezielle probleme über die Bewegung geradliniger paralleler Wirbelfäden*. PhD thesis, Georg-August-Universität Göttingen, 1877.

[28] B. C. Hall. *Lie Groups, Lie Algebras, and Representations: An Elementary Introduction*. Springer, 2015.

[29] G. W. Hill. On the part of the motion of the lunar perigee which is a function of the mean motions of the sun and moon. *Acta Math.*, 8:1–36, 1886.

[30] Jorge V. José and Eugene J. Saletan. *Classical dynamics: a contemporary approach*. Cambridge University Press, 1998.

[31] A. A. Kamel. Expansion formulae in canonical transformations depending on a small parameter. *Celest. Mech. Dyn. Astron.*, 1969.

[32] G.R. Kirchhoff. *Vorlesungen über mathematische Physik: Mechanik*, volume 1 of *Vorlesungen über mathematische Physik*. Teubner, Leipzig, 1876.

[33] C. Lopesino, F. Balibrea-Iniesta, V. J. García-Garrido, S. Wiggins, and A. M. Mancho. A theoretical framework for lagrangian descriptors. *Int. J. Bifurca. Chaos*, 27(01):1730001, 2017.

[34] A. E. H. Love. On the motion of paired vortices with a common axis. *Proc. London Math. Soc.*, 1:185–194, 1893.

[35] J. A. Jiménez Madrid and A. M. Mancho. Distinguished trajectories in time dependent vector fields. *Chaos*, 19(1):013111, 2009.

[36] A. M. Mancho, S. Wiggins, J. Curbelo, and C. Mendoza. Lagrangian descriptors: A method for revealing phase space structures of general time dependent dynamical systems. *Communications in Nonlinear Science and Numerical Simulation*, 18(12):3530 – 3557, 2013.

[37] Maplesoft, a division of Waterloo Maple Inc. Maple, 2020. Waterloo, Ontario.

[38] L. Markus and H. Yamabe. Global stability criteria for differential systems. *Osaka J. Math.*, 12:305–317, 1960.

[39] M R Matthews, B P Anderson, P. C. Haljan, D. S. Hall, C. E. Wieman, and E. A. Cornell. Vortices in a Bose-Einstein Condensate. *Phys. Rev. Lett.*, 83:2498–2501, 1999.

[40] James D. Meiss. *Differential dynamical systems*. SIAM, Society for Industrial and Applied Mathematics, 2017.

[41] Kenneth Ray Meyer and Glen R. Hall. *Introduction to Hamiltonian dynamical systems and the N-body problem*. Springer-Verlag, 1992.

[42] J. Moser. On invariant curves of area-preserving mappings of an annulus. *Nachr. Akad. Wiss. Göttingen, II*, pages 1–20, 1962.

[43] R. Navarro, R Carretero-González, P. J. Torres, P. G. Kevrekidis, D. J. Frantzeskakis, M. W. Ray, E. Altuntaş, and D. S. Hall. Dynamics of a few corotating vortices in Bose-Einstein condensates. *Phys. Rev. Lett.*, 110:225301, 2013.

[44] P. K. Newton. *The N-Vortex Problem: Analytical Techniques*. Springer, 2001.

[45] P. K. Newton and H. Shokraneh. Interacting dipole pairs on a rotating sphere. *Proc. R. Soc. London, Ser. A*, 464:1525–1541, 2008.

[46] L. Perko. *Differential Equations and Dynamical Systems*. Springer-Verlag, Berlin, Heidelberg, 1991.

[47] H. Poincaré. *Les Méthodes Nouvelles de la Mécanique Céleste. Tome III*. Gauthier-Villars, 1899.

[48] J. A. Pérez-Hernández and L. Benet. PerezHz/TaylorIntegration.jl: TaylorIntegration v0.4.1, 2019.

[49] C. Rackauckas and Q. Nie. Differentialequations. jl–a performant and feature-rich ecosystem for solving differential equations in julia. *J. Open Res. Softw.*, 5(1), 2017.

[50] J. Revels, M. Lubin, and T. Papamarkou. Forward-mode automatic differentiation in Julia. *arXiv:1607.07892 [cs.MS]*, 2016.

[51] N. Rott. Three-vortex motion with zero total circulation. *Z Angew Math Phys*, 40:473–494, 1989.

[52] D. A. Sadovski and J. B. Delos. Bifurcation of the periodic orbits of Hamiltonian systems: An analysis using normal form theory. *Phys. Rev. E*, 1996.

[53] S. A. Smith. *Point Vortices: Finding Periodic Orbits and their Topological Classification*. PhD thesis, Tufts University, 2012.

[54] L. Tophøj and H. Aref. Chaotic scattering of two identical point vortex pairs revisited. *Phys. Fluids*, 20:093605, 2008.

[55] L. Tophøj and H. Aref. Instability of vortex pair leapfrogging. *Phys. Fluids*, 25:014107, 2013.

[56] D. Treschev and O. Zubelevich. *Introduction to the Perturbation Theory of Hamiltonian Systems*. Springer-Verlag Berlin Heidelberg, 2009.

[57] C. Tsitouras. Runge–kutta pairs of order 5 (4) satisfying only the first column simplifying assumption. *Comput. Math. with Appl.*, 62(2):770–775, 2011.

[58] J. H. Verner. Numerically optimal runge–kutta pairs with interpolants. *Numerical Algorithms*, 53(2-3):383–396, 2010.

[59] H. von Helmholtz. Über integrale der hydrodynamischen gleichungen, welcheden wirbelbewegungen entsprechen. *J. Reine Angew. Math*, 55:25–55, 1858.

[60] D. H. Wacks, A. W. Baggaley, and C. F. Barenghi. Coherent laminar and turbulent motion of toroidal vortex bundles. *Phys. Fluids*, 26:027102, 2014.

[61] B. Whitchurch, P. G. Kevrekidis, and V. Koukouloyannis. Hamiltonian bifurcation perspective on two interacting vortex pairs: From symmetric to asymmetric leapfrogging, period doubling, and chaos. *Phys. Rev. Fluids*, 3:014401, 2018.

[62] E. T. Whittaker and G. N. Watson. *A Course of Modern Analysis*. Cambridge University Press, 1902.

[63] S. Wiggins. *Introduction to Applied Nonlinear Dynamical Systems and Chaos*. Texts in Applied Mathematics. Springer New York, 2003.

[64] Wolfram Research, Inc. Mathematica, Version 12.0, 2019. Champaign, IL.

[65] V. Yakubovich and V. Starzhinskii. *Linear Differential Equations with Periodic Coefficients Vol. 1*. John Wiley and Sons, 1975.